Quantum Metrology Tools for Enhancing Time-Resolved Spectroscopy

Dionysis Adamou

Submitted in fulfilment of the requirements for the Degree of Doctor of Philosophy

School of Engineering

College of Science and Engineering

University of Glasgow

November 2025

Supervisory Team:

Matteo Clerici

Primary Supervisor

Jonathan Weaver

Secondary Supervisor

Ashley Lyons

Co-Supervisor

Abstract

In conventional balanced-detection measurements, sensitivity can generally be improved by increasing the optical power. However, in many systems this approach reaches an upper bound beyond which increasing the probe power can damage the sample or degrade the measurement. In THz time-domain spectroscopy, this bound is set by nonlinear noise and measurement back-action. When this ceiling is reached by classical techniques, a potential avenue to improve the signal-to-noise ratio is by using quantum metrological resources. This work reports the development of a bright, ultrafast twin-beam source, exhibiting more than 6 dB of noise suppression up to microwatt optical power levels, together with an ultra-low-noise balanced photoreceiver with sub-shot-noise performance. Integrating these technologies into a THz-TDS system developed in collaboration with colleagues we demonstrate, for the first time to our knowledge, a measurable enhancement in sensitivity by harnessing quantum correlations when compared with a classical source under identical conditions. Although the implemented THz-TDS setup deviates from conventional polarimetric schemes, which typically achieve higher sensitivity, these results show that quantum methods can provide a sensitivity enhancement in field-resolved THz spectroscopy. Beyond this demonstration, the developed twin-beam source has clear potential for wider use as its brightness, stability and correlation strength make it an attractive candidate for ultrafast, differential transient absorption measurements.

Contents

List of Tables

List of Figures

List of Abbreviations

AOM: Acousto-Optic Modulator
BBO: Beta-Barium Borate
CMRR: Common-Mode Rejection Ratio
CW: Continuous Wave
DFG: Difference-Frequency Generation
EO: Electro-Optic
EOS: Electro-Optic Sampling
FRS: Field-Resolved Spectroscopy
GaP: Gallium Phosphide
GVM: Group-Velocity Mismatch
InGaAs: Indium Gallium Arsenide
ND: Neutral-Density Filter
NIR: Near Infrared
NRF: Noise-Reduction Factor
OAP: Off-Axis Parabolic
OPA: Optical Parametric Amplification
OR: Optical Rectification
PBS: Polarising Beam Splitter
PCB: Printed-Circuit Board
PD: Photodiode
p-pol: Horizontal Polarisation
QE: Quantum Efficiency
QPM: Quasi-Phase Matching
RMS: Root-Mean-Square
s-pol: Vertical Polarisation
SFG: Sum-Frequency Generation
SHG: Second-Harmonic Generation
SNR: Signal-to-Noise Ratio
SPDC: Spontaneous Parametric Down-Conversion
TDS: Time-Domain Spectroscopy
TEC: Thermoelectric Cooling
THz: Terahertz
TIA: Transimpedance Amplifier
TTL: Transistor–Transistor Logic

Acknowledgements

I am deeply grateful to my supervisor, Matteo Clerici for his exceptional guidance and constant encouragement throughout this journey. His scientific insight, humour, and generosity with his time have made the entire experience both intellectually stimulating and enjoyable. I also thank Daniele Faccio for welcoming me into his group for the latter stages of my PhD, as well as Ashley Lyons, who served as my supervisor during this period.

I would also like to thank Lucia Caspani, Jonathan Weaver and Marco Peccianti for the insightful discussions we had, which greatly contributed to my technical development and the progress of this project. My special thanks go to Lenny Hirsch, with whom I shared many long and often frustrating days in the lab, always pushing each other all the way to the finish line. I am also grateful to him for introducing me to 3D modelling tools.

Finally, I want to express my deepest appreciation for my parents, Chris and Helen. Their support and belief in me throughout my studies made this possible. I owe them everything.

Conferences and Publications

Peer-Reviewed Publications

Adamou, D., Hirsch, L., Shields, T., Yoon, S., Dada, A. C., Weaver, J. M. R., Faccio, D., Peccianti, M., Caspani, L., & Clerici, M. (2025). Quantum-enhanced time-domain spectroscopy. *Science Advances*, *11*(4), eadt2187.

Hirsch, L., **Adamou, D.**, Faccio, D., Peccianti, M., & Clerici, M. (2024). Design of an optimized terahertz time-domain spectroscopy system pumped by a 30 W Yb: KGW source at a 100 kHz repetition rate with 245 fs pulse duration. *Applied Sciences*, *14*(15), 6688.

Löscher, R., Moreno, V., **Adamou, D.**, Kesim, D. K., Schroeder, M. C., Clerici, M., Wolf, J.-P., & Saraceno, C. J. (2023). High-power sub-picosecond filamentation at 1.03 μm with high repetition rates between 10 and 100 kHz. *APL Photonics*, *8*(11).

Wang, T.-J., Ebrahim, M. H., Afxenti, I., **Adamou, D.**, Dada, A. C., Li, R., Leng, Y., Diels, J.-C., Faccio, D., Couairon, A., Milián, C., & Clerici, M. (2023). Cumulative Effects in 100 kHz Repetition-Rate Laser-Induced Plasma Filaments in Air. *Advanced Photonics Research*, *4*(3), 2200338. https://doi.org/10.1002/adpr.202200338

Conference Contributions

Adamou, D., Hirsch, L., Shields, T., Yoon, S., Dada, A. C., Weaver, J. M. R., Faccio, D., Caspani, L., Peccianti, M., & Clerici, M. (2025). Quantum enhanced time-domain spectroscopy. *Optica Nonlinear Optics Topical Meeting*, Honolulu, Hawaii, USA, 4–7 August.

Adamou, D., Hirsch, L., Shields, T., Yoon, S., Dada, A. C., Weaver, J. M. R., Faccio, D., Caspani, L., Peccianti, M., & Clerici, M. (2025). Quantum-enhanced time-domain sampling of THz fields. *CLEO/Europe–EQEC 2025*, Munich, Germany, 23–27 June (oral).

Adamou, D., Hirsch, L., Shields, T., Yoon, S., Dada, A. C., Weaver, J. M. R., Faccio, D., Caspani, L., Peccianti, M., & Clerici, M. (2025). Quantum-enhanced time-domain sampling of THz fields. *Optica Quantum 2.0 Conference and Exhibition*, San Francisco, California, USA, 1–5 June (oral).

Adamou, D., Hirsch, L., Shields, T., Yoon, S., Dada, A. C., Weaver, J. M. R., Faccio, D., Caspani, L., Peccianti, M., & Clerici, M. (2024). Development of nonclassical light sources for time-resolved THz detection. *14th International Conference on Metamaterials, Photonic Crystals and Plasmonics (META 2024)*, Toyama, Japan, 16–19 July (oral).

Adamou, D., Hirsch, L., Shields, T., Yoon, S., Dada, A. C., Weaver, J. M. R., Faccio, D., Caspani, L., Peccianti, M., & Clerici, M. (2024). Probing terahertz pulses with nonclassical radiation. *10th International Conference on Antennas and Electromagnetic Systems (AES 2024)*, Rome, Italy, 25–28 June (oral).

Adamou, D., Hirsch, L., Shields, T., Yoon, S., Dada, A. C., Weaver, J. M. R., Faccio, D., Caspani, L., Peccianti, M., & Clerici, M. (2024). Towards quantum-enhanced THz sensing. *13th Advanced Lasers and Photon Sources (ALPS 2024)*, Yokohama, Japan, 22–26 April (oral).

Löscher, R., Moreno, V., **Adamou, D.**, Kesim, D. K., Schroeder, M. C., Clerici, M., Wolf, J.-P., & Saraceno, C. (2024). Quasi-stationary hydrodynamics in high-repetition-rate filamentation. *Optica High-Brightness Sources and Light-Driven Interaction Congress 2024*, Vienna, Austria, 12–14 March (oral).

Adamou, D., Hirsch, L., Weaver, J. M. R., Faccio, D., Caspani, L., Peccianti, M., & Clerici, M. (2023). Large (>3 dB) noise reduction factors from sub–shot-noise quantum correlations in <200 fs pulses. *SPIE Photonex 2023*, Glasgow, UK, 24–26 October (oral).

Adamou, D., Ebrahim, M. H., Afxenti, I., Wang, T.-J., Milián, C., Dada, A. C., Li, R., Leng, Y., Diels, J.-C., Faccio, D., Couairon, A., & Clerici, M. (2023). Laser-induced plasma filaments in air at high repetition rates: the role of cumulative effects. *Quantum, Atomic, and Molecular Physics (QuAMP 2023)*, Institute of Physics, Glasgow, UK, 11–13 September (poster).

Adamou, D., Hirsch, L., Weaver, J. M. R., Faccio, D., Caspani, L., Peccianti, M., & Clerici, M. (2023). Large (>3 dB) noise reduction factors from sub–shot-noise quantum correlations in <200 fs pulses. *Quantum, Atomic, and Molecular Physics (QuAMP 2023)*, Institute of Physics, Glasgow, UK, 11–13 September (poster).

Wang, T.-J., Ebrahim, M. H., Afxenti, I., **Adamou, D.**, Milián, C., Dada, A. C., Li, R., Leng, Y., Diels, J.-C., Faccio, D., Couairon, A., & Clerici, M. (2022). Cumulative effects in high-repetition-rate filaments. *Conference on Filamentation (COFIL 2022)*, Chania, Crete, 11–15 July (oral).

Declaration

I declare that this thesis is the result of my own work and has not been submitted for any other degree or any other institution. Where work conducted in collaboration, this has been clearly acknowledged.

1 Introduction

Optical spectroscopy serves as a robust analytical technique, crucial for fundamental research and various applications. It allows the identification of chemical compounds [1], the assessment of environmental quality [2], and the exploration of molecular interactions within intricate biological systems [3].

To understand how this technique came to be, we must trace its origins back to the 17th century, when Isaac Newton conducted his systematic study of light, producing his first published paper [4]. Here, he demonstrated that white light is comprised of various colours, challenging the common belief that prisms added colour to light rather than separating it. This essential research established the basis for what would eventually be recognised as spectroscopy.

A significant advancement followed in 1802, when William Hyde Wollaston noted several dark lines in the solar spectrum [5], marking the first recorded spectral features. While Wollaston incorrectly interpreted these as natural separations between colours, his findings were the first signs of what we now recognise as absorption lines. In 1814, Joseph von Fraunhofer expanded upon Wollaston's observations by refining his interpretation and employing better optics, notably his diffraction grating, to systematically map hundreds of dark lines across the solar spectrum [6]. These lines, now known as Fraunhofer lines, represent the first recorded absorption spectrum.

Decades later, Gustav Kirchhoff and Robert Bunsen made a crucial breakthrough by demonstrating that specific chemical elements absorb light at characteristic wavelengths, thus establishing a direct link between spectral patterns and atomic structure. This insight marked the birth of spectrochemical analysis, transforming spectroscopy into a powerful tool for chemical identification and astrophysical research.

Although William Herschel discovered infrared radiation in 1800, progress in the field was initially slow due to the lack of suitable detection instruments. This began to change by the mid-19th century with the development of tools like the Nobili–Melloni

thermopile, which enabled more sensitive heat detection. In 1859, John Tyndall used the thermopile to systematically explore the properties of infrared radiation and gas absorption, laying important groundwork for infrared studies. The conventional extension of spectroscopy into the infrared is generally marked by the work of Abney and Festing in 1881, who built on Tyndall's findings and recorded the first infrared absorption spectra of organic liquids [7]. These steps established infrared spectroscopy as a distinct branch of analytical science. In the coming years, researchers discovered that molecular vibrations could be interrogated by infrared radiation. Therefore, chemical bonds and structures could be identified directly across all states of matter, a transformative leap in analytical science.

Around the same time, Heinrich Hertz's discovery of radio waves [8], despite occurring at much longer wavelengths, sparked a broader scientific interest in probing the electromagnetic spectrum beyond the visible and near-infrared. This curiosity was taken further by Heinrich Rubens, who, alongside E.F. Nichols, was among the first to recognise the existence of a spectral region between optical and electronic sources, a region now referred to as the terahertz (THz) gap [9].The THz region bridges the microwave and infrared regions of the electromagnetic spectrum spanning roughly between 0.1 to 10 THz. Various complex biomolecules exhibit low-frequency vibrational and rotational modes within this range, directly related to molecular function and dynamics. Combined with the non-ionising nature of THz radiation, these properties make THz spectroscopy a powerful non-destructive analytical tool with broad potential applications spanning genetics, biomedical research, and drug discovery and development. Moreover, the strong penetrative ability of this region makes it extremely useful for military and security applications [10], [11]. Other potential applications include free-space communications [12] and semiconductor research [13].

By 1921, Rubens had successfully extended classical infrared spectroscopy into the far infrared, reaching wavelengths of up to 400 μm. Although the term "terahertz" had not yet been coined, Rubens' meticulous, point-by-point measurements represent the first systematic spectroscopic exploration of this long-wavelength region, paving the way for bridging the gap between optics and electronics [14].

Despite advancements, progress was slow throughout much of the 20th century due to the lack of suitable coherent sources and sensitive detectors. Consequently, THz optics has emerged as a unique research area where scientists work to implement and modify techniques to create innovative methods and materials that can harness the features and applications of the THz spectrum.

The three most common optical methods of generating coherent, broadband THz radiation are via optical rectification, photoconductive antennas, and two-colour air plasma generation. All three rely on nonlinear optical processes that require a high-intensity, coherent light source, typically delivered by pulsed lasers. Therefore, it is not surprising that the emergence of femtosecond mode-locked lasers in the 1980s and 1990s facilitated the advancement of terahertz time-domain spectroscopy (THz-TDS). Originally demonstrated in 1988 by Smith *et al*. [15] and later refined by Grischkowsky *et al.* [16], this technique captures THz radiation in the time domain, distinguishing it from traditional spectroscopy methods that operate in the frequency domain. This provides an additional incentive to utilise THz-TDS as it provides both amplitude and phase information of the probed sample.

Building upon the foundations set by THz-TDS and with the emergence of few-cycle laser pulses and phase-stable detection schemes, the technique naturally evolved toward shorter wavelengths. This gave rise to field-resolved spectroscopy (FRS), where the time-domain principles of THz-TDS are applied to the infrared and visible ranges. As in THz-TDS, FRS records the full electric field waveform, providing direct access to a material's complex optical response [17].

A key breakthrough was reported by Pupeza *et al.* [18], where broadband field-resolved infrared spectroscopy was demonstrated, spanning three octaves. As highlighted by Ferenc Krausz in his 2023 Nobel Lecture [19], field-resolved methods mark a major shift in photonics, where the focus has been shifted from energy spectra measurements to the direct observation of electromagnetic field evolution in time. In summary, field-resolved spectroscopy stands as the most advanced approach for light-matter interaction studies, laying the foundation for the future developments in quantum-enhanced and attosecond spectroscopy.

1.1 Aims & Objectives

Electro-optical sampling (EOS) is a method commonly employed in THz-TDS, which involves spatiotemporally overlapping the THz field with a shorter optical pulse in a second-order nonlinear (electro-optical) crystal. The probe undergoes a phase shift induced by the unknown (THz) electric field, which is measured by polarimetry.

Although research is ongoing to define EOS's maximum sensitivity [20], the noise of the probe pulse limits its sensitivity. Shot noise, originating from the quantisation of the electromagnetic field, defines the fundamental noise limit of coherent pulses [21]. The signal-to-noise ratio (SNR) in shot-noise-limited measurements scales with the square of the photon number N, i.e., SNR $\propto \sqrt{N}$. Therefore, by increasing the energy (number of photons per pulse) of the probe pulses, a higher SNR can be achieved. However, it has recently been shown that an upper bound is set by nonlinear noise and back action [22]. Thus, a promising route to overcome the current constraints of EOS is by employing the tools delivered by quantum metrology for sub-shot-noise measurements [23].

The main goal of my PhD work has been to generate ultrafast (sub-picosecond) quantum-correlated fields, via parametric down-conversion in a second-order crystal and experimentally demonstrate an advantage in sensitivity when employing the quantum fields, compared to classical light.

Detecting and measuring such fields requires low-noise, high-quantum-efficiency optoelectronics. As these are application-specific devices, they are difficult to source commercially. Consequently, the design, development and characterisation of the balanced detector used to measure sub-shot noise properties of quantum fields has been a central deliverable of my research activity.

1.2 Thesis Structure

The thesis is structured is as follows:

Chapter 2 outlines the fundamental principles of nonlinear optics, with particular focus on second-order processes that underpin the generation of quantum-correlated light.

Chapter 3 discusses the merits of balanced detection, then establishes the theoretical foundation for low-noise transimpedance amplification. Subsequently, it reports the results on the design, development and characterisation of a custom ultra-low-noise balanced detector is presented, necessary to detect and measure quantum correlations leading to sub-shot noise sensitivities.

Chapter 4 begins by demonstrating shot-noise limited detection, using the developed detector, at nanowatt optical power levels. The development of two, two-mode squeezed light sources are described, aiming to demonstrate quantum-noise suppression below the shot-noise limit.

Chapter 5 introduces the theoretical background of the techniques employed to generate and detect THz pulses. It then describes the results of the initial THz-TDS system development, outlining its limitations and the optimisation steps undertaken to improve its performance. The integration of the twin-beams into the setup is described. Finally, the chapter concludes by presenting the experimental results for the THz-TDS system that employs a quantum source as the probe.

Chapter 6 concludes the findings of my PhD work, reflecting on the achievements and the limitations of the experimental approach, and outlining potential avenues for overcoming these limitations.

2 Nonlinear Optics

The interaction of light and matter is at the core of various areas of optics and photonics, including refraction, absorption, nonlinear and quantum effects. A key aspect of this interaction is how the applied electric field induces electric dipole moments, causing the positive and negative charges within atoms or molecules to shift slightly in opposite directions. The polarisation density $\boldsymbol{P}$ is given by the vector sum of all these moments. Traditionally, it was assumed that the polarisation density scales linearly with the applied electric field $\boldsymbol{E}$ so that the relationship between them is given by [24]

$$\boldsymbol{P}(t) = \epsilon_0 \chi \boldsymbol{E}(t), \tag{2.1}$$

where ϵ_0 represents the permittivity of free space, and χ is the electric susceptibility of the medium (we are here simplifying to homogeneous materials with an instantaneous response). From a time-varying polarisation vector, a scattered field emerges because of the light-matter interaction. Under the linearity assumption, optical properties such as the refractive index and absorption coefficient, are not affected by the intensity of the field that is propagating. Moreover, the principle of superposition applies, meaning that overlapping light waves do not interact with one another directly; instead, their individual electric fields combine linearly, producing interference effects.

The game changed in 1960 when Theodore Maiman demonstrated the first laser [25]. The coherent properties of the laser enabled scientists to investigate light-matter interactions at unprecedented intensities.

Experiments under these conditions swiftly discarded the assumption of linear optical media. Nonlinear optics emerged in 1961, when Franken *et al.* [26] first demonstrated second-harmonic generation, where it was proven experimentally that intense electromagnetic fields can induce nonlinear polarisation in matter. Between 1962 and 1965 numerous nonlinear phenomena were observed such as sum and difference-frequency generation [27], optical rectification [28], parametric amplification [29], [30], stimulated Raman and Brillouin scattering [31], third-harmonic generation [32] and the

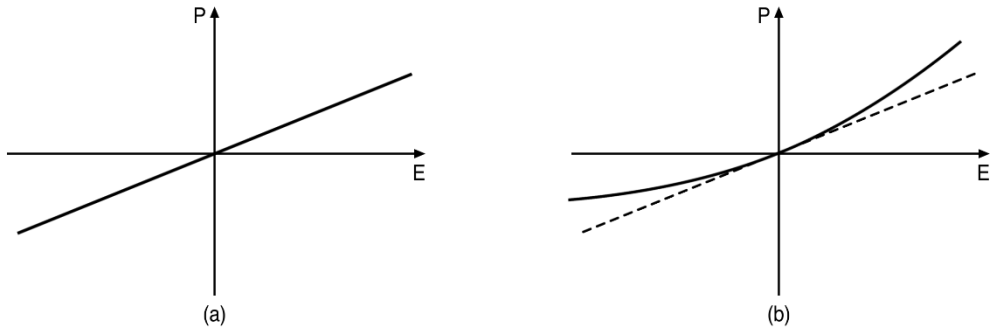

Figure 2.1 – Polarisation density P as a function of applied electric field E for (a) a linear medium, where $P = \varepsilon_0\chi^{(1)}E$, and (b) a nonlinear medium, where higher-order susceptibility terms contribute at large field amplitudes. In (b), the dashed line shows the linear response for comparison, highlighting the increasing deviation of the true response (solid curve) from linearity. [19].

optical Kerr effect [33]. Driven by the advent of high-power laser sources, these discoveries demonstrated that the optical properties of media can be altered by the very light propagating through it, implying that light can interact with itself. Therefore, the linear principle of superposition, a foundation of light-matter interaction in the linear regime, was no longer valid.

It is essential to note that linearity or nonlinearity is a property of the medium, not of the field. The presence of an optical field can alter the medium's properties, potentially influencing another optical field or even the original field itself. Thus, it is the medium that is the vehicle driving these light-light interactions.

In contrast to what is described by Eq. 2.1. In nonlinear media, the relationship between ***P*** and ***E*** is nonlinear. Examples of the polarisation dependence to the applied electric field for linear and nonlinear media are illustrated in Figure 2.1 [34].

Assuming that the electric field is weaker than the interatomic fields, the dipoles do not break, tunnelling effects can be ignored, and the polarisation density of the system can be modelled using a Taylor series expansion in powers of the electric field, beginning with the linear susceptibility term ($\chi^{(1)}$)

$$P(t) = \epsilon_0\left[\chi^{(1)}E(t) + \chi^{(2)}E^2(t) + \chi^{(3)}E^3(t) + \cdots\right]. \qquad \textbf{2.2}$$

Here, a lossless medium with isotropic permittivity has been assumed, the vector notation has been omitted, and an instantaneous response to excitation has been considered.

In typical centrosymmetric materials, the second order term is non-existent because symmetry requires that $\chi^{(2)} = 0$. On the other hand, crystals with non-centrosymmetric structures can exhibit second-order nonlinear effects, represented by the second term in the perturbative series. To understand how various nonlinear effects arise, we will examine the propagation of light in nonlinear media.

For simplicity, we will assume that all fields propagate along the same axis, omitting the vector notation and using the scalar approximation. The wave equation, derived from Maxwell's equations, for an arbitrary homogeneous dielectric medium, is

$$\nabla^2 E - \frac{1}{c_0^2}\frac{\partial^2 E}{\partial t^2} = \mu_0 \frac{\partial^2 P}{\partial t^2}, \tag{2.3}$$

where μ_0 is the magnetic permeability and c_0 the light speed.

Since the polarisation density is comprised of linear and non-linear terms, it can be expressed as

$$P = \epsilon_0 \chi E + P_{\mathrm{NL}}, \tag{2.4}$$

where

$$P_{\mathrm{NL}} = \epsilon_0 \left(\chi^{(2)} E^2 + \chi^{(3)} E^3 + \cdots\right), \tag{2.5}$$

considering that $n^2 = 1 + \chi$, $c_0 = 1/\sqrt{\mu_0 \epsilon_0}$ and $c = c_0/n$, Eq. 2.3 can be expressed as

$$\nabla^2 E - \frac{1}{c^2}\frac{\partial^2 E}{\partial t^2} = -S, \tag{2.6}$$

where

$$S = -\mu_0 \frac{\partial^2 P_{\mathrm{NL}}}{\partial t^2}. \tag{2.7}$$

A nonlinear polarisation $P_{\mathrm{NL}}$is induced by an optical field E. Because of the nonlinear dependency of both P_{NL}(and thus S) on E, Eq. 2.6 is, therefore, a nonlinear partial differential equation in E. It is commonly referred to as the nonlinear wave equation, which forms the basis of nonlinear optics theory. The source term S (Eq. 2.7) is a product of the time-varying nonlinear polarisation and serves as the physical mechanism which drives the nonlinear equation.

Engineering advanced optical technologies depends on solving the nonlinear wave equation. Solving it analytically is not always feasible or effective, so two approximated approaches are usually implemented. The first is the Born approximation, an iterative approach, and the second is the coupled-wave theory. Here, we consider the Born approximation as it allows for a more simplified introduction to nonlinear optics.

The source term S is a function of the optical field E which generates it. This self-reinforcing relationship can be appreciated by considering an initial optical field E_0 incident on a nonlinear medium. As aforementioned, this creates a source term $S(E_0)$, which radiates a resulting field E_1. In turn, this field creates another source term $S(E_1)$ that will generate a field at E_2 and so forth. The nature of the process invites an iterative solution, where the initial step is known as the first Born approximation.

The first Born approximation can be considered when the light intensity, and hence the nonlinearity, is weak. Here, the light propagating through a nonlinear medium is modelled as a scattering process. Firstly, the nonlinear polarisation density is determined by the initial field E_0 using Eq.2.5. P_{NL} is then used to compute $S(E_0)$, using Eq.2.7, which is subsequently utilised to evaluate E_1. Due to the nonlinear dependence of $S(E_0)$ on the input field, new frequency components are generated in the emitted field E_1 that did not exist in the original field. In this case, light is modifying its own spectral content. This effect, among other interesting phenomena, is routinely employed to engineer light for a host of applications [24]. In the following sections of this chapter, we will cover second-order nonlinear processes relevant to the experimental work undertaken for the project.

2.1 Second-Harmonic Generation

Second-harmonic generation (SHG) was the first experimentally observed nonlinear effect, just a year after the laser was invented. Given its historical importance and role, it provides a natural entry point into second-order optical effects.

Since we are assuming that nonlinearities of higher than the second order are negligible and $d = \epsilon_0 \chi^{(2)}$, P_{NL} becomes

$$P_{\mathrm{NL}} = 2dE^2. \tag{2.8}$$

Suppose a nonlinear medium is driven by a harmonic electric field with angular frequency ω and complex amplitude *E(ω)*

$$E(t) = \mathrm{Re}\{E(\omega)e^{j\omega t}\}. \tag{2.9}$$

To acquire the nonlinear polarisation density induced by this field, we substitute Eq. 2.9 into Eq. 2.8 so that

$$P_{\mathrm{NL}} = P_{\mathrm{NL}}(0) + \mathrm{Re}\{P_{\mathrm{NL}}(2\omega)e^{j2\omega t}\}, \tag{2.10}$$

where

$$P_{\mathrm{NL}}(0) = dE(\omega)E^*(\omega), \tag{2.11}$$

and

$$P_{\mathrm{NL}}(2\omega) = dE(\omega)E(\omega). \tag{2.12}$$

This process is illustrated in Figure 2.2, highlighting both contributions to the nonlinear polarisation density. The P_{NL} (0) component is a constant, time-invariant polarisation density, which creates a potential difference across the material [35]. This nonlinear effect, known as optical rectification, is crucial to the generation of THz radiation where femtosecond pulses are transformed to broadband THz pulses. A detailed discussion will

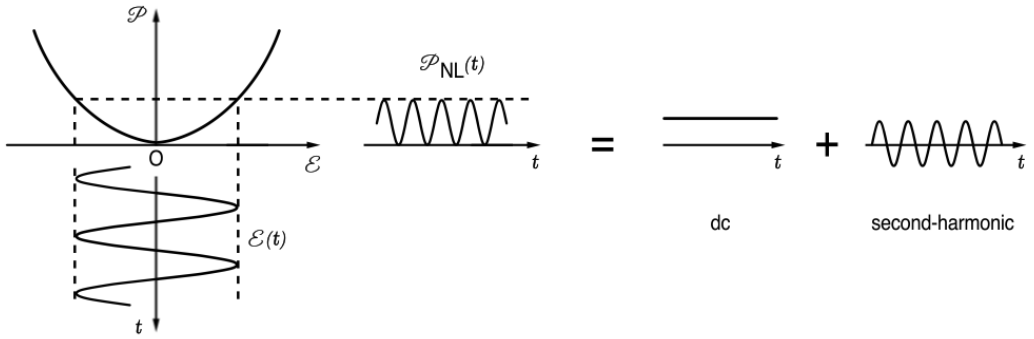

Figure 2.2 - Decomposition of P_{NL} generated when a harmonic electric field propagates through a second-order nonlinear medium. The quadratic dependence of P_{NL} on the electric field produces a DC component (optical rectification) and a field oscillating at twice the frequency of the incident field, reconstructed from [24].

be presented in Chapter 5. For now, we will concentrate on the oscillating polarisation density component.

By applying the Born approximation and considering Eq. 2.12 and Eq. 2.7 it can be deduced that $S(E_0)$ consists of frequencies at 2ω. Therefore, the emitted field E_1 oscillates at twice the input field frequency, a phenomenon known as second-harmonic generation (SHG).The complex amplitude of the second-harmonic source term is proportional to $S(2\omega) = 4\mu_0\omega^2 dE(\omega)E(\omega)$. The resulting second-harmonic intensity is given by $|S(2\omega)|^2 \propto \omega^4 d^2 I^2$, where I is the intensity of the input field, defined as $I = n\epsilon_0 cE^2$.

The conversion efficiency scales as $I = P/A$, where P is the optical power and A is the beam cross-sectional area. Consequently, tight focusing and high optical power both significantly enhance SHG efficiency. This makes pulsed laser sources particularly well-suited to nonlinear interactions, owing to their high peak powers

2.2 Three-Wave Mixing

Although it may not be completely obvious at first, SHG is a specific case of a broader category of classical second-order nonlinear phenomena known as three-wave mixing, whereby an output field is generated by combining two input fields. In the case of SHG,

it can be considered the sum of two degenerate input fields ($\omega_1 = \omega_2$) oscillating at ω, generating an output field oscillating at 2ω. This is known as Sum Frequency Generation (SFG).

To better understand how three-wave mixing is realised, we examine the scenario in which the input electric field is comprised of waves oscillating at two distinct frequencies, ω_1 and ω_2,

$$E(t) = \mathrm{Re}\{E(\omega_1)e^{j\omega_1 t} + E(\omega_2)e^{j\omega_2 t}\}. \quad \textbf{2.13}$$

By inserting Eq. 2.13 into Eq. 2.8 it follows that P_{NL} mathematically consists of five terms oscillating at 0, $2\omega_1$, $2\omega_2$, $\omega_+ = \omega_1+\omega_2$, $\omega_- = \omega_1-\omega_2$ with their amplitudes are expressed as

$$P_{\mathrm{NL}}(0) = d[|E(\omega_1)|^2 + |E(\omega_2)|^2], \quad \textbf{2.14}$$

$$P_{\mathrm{NL}}(2\omega_1) = dE(\omega_1)E(\omega_1), \quad \textbf{2.15}$$

$$P_{\mathrm{NL}}(2\omega_2) = dE(\omega_2)E(\omega_2), \quad \textbf{2.16}$$

$$P_{\mathrm{NL}}(\omega_+) = 2\,dE(\omega_1)E(\omega_2), \quad \textbf{2.17}$$

$$P_{\mathrm{NL}}(\omega_-) = 2\,dE(\omega_1)E^*(\omega_2)\,. \quad \textbf{2.18}$$

These terms in P_{NL} act as sources in the nonlinear wave equation **(**Eqs. 2.6 - 2.7), driving new electromagnetic waves at their oscillating frequency.

2.3 Phase Matching

In the previous section, it was shown that it is possible to induce a nonlinear polarisation consisting of components at several frequencies by combining two optical fields in a second-order nonlinear medium. These frequencies results from the processes of Sum-

Frequency Generation (SFG), Difference-Frequency Generation (DFG), and SHG which are denoted by Eqs. 2.15-2.18. Although the P_{NL} consists of these components, electromagnetic waves oscillating at the respective frequencies are not necessarily generated. For a propagating optical field to be generated, the electromagnetic wave generated at a coordinate inside the nonlinear material needs to constructively interfere with the one generated at a different component along the propagating direction. Physically speaking this requires that they remain synchronised with the driving field throughout the nonlinear material [36].

Let's consider the case where we want to generate SFG between two plane waves of wavevectors k_1 and k_2 that are propagating in a nonlinear medium. Their associated electric fields are expressed as $E(\omega_1) = A_1 \mathrm{e}^{-\mathrm{j}k_1 r}$ and $E(\omega_2) = A_2 \mathrm{e}^{-\mathrm{j}k_2 r}$. Then, as per Eq. 2.17, $P_{\mathrm{NL}}(\omega_3) = dE(\omega_1)E(\omega_2) = 2dA_1A_2e^{-\mathrm{j}k_3 r}$

where

$$\omega_3 = \omega_1 + \omega_2 \qquad \textbf{2.19}$$

and

$$k_3 = k_1 + k_2. \qquad \textbf{2.20}$$

From these equations (Eqs. 2.19 - 2.20) which represent the energy (frequency) and momentum (phase) matching conditions, we can picture the nonlinear medium acting as source, which emits light at ω_3 with its spatial evolution described by $\mathrm{e}^{-\mathrm{j}k_3 r}$. The emitted field's wavevector therefore must satisfy Eq. 2.20. Because the field's spatiotemporal behaviour is governed by $\omega t - kr$, spatial and temporal phase matching is guaranteed if the two conditions are met. This is essential for maximising and sustaining the nonlinear conversion from the input fields to the output scattered wave within the nonlinear medium, increasing the efficiency of the process.

The full derivation of nonlinear processes using the coupled-wave formalism will not be presented here as it is not in the scope of this work, however a detailed coupled-wave

analysis of SFG is available in [36], providing an expression for the output intensity of ω_3 given by

$$I_3 = \frac{2d_{\text{eff}}^2\omega_3^2 I_1 I_2}{n_1 n_2 n_3 \varepsilon_0 c^3} L^2 \text{sinc}^2\left(\frac{\Delta kL}{2}\right). \quad \textbf{2.21}$$

Here, d_{eff} is the nonlinear coefficient, I_1 and I_2 are the intensities of the input fields, n_i is the refractive index of the medium at frequency i, and L is the propagation length. Additionally, Δk denotes the wavevector mismatch, which for perfect phase-matching must satisfy

$$\Delta k = 0 = k_1 + k_2 - k_3. \quad \textbf{2.22}$$

As it can be deduced from Eq. 2.21, in this condition ($\Delta k = 0$) the intensity of the output field is at maximised, as depicted in Figure 2.3. When L becomes larger than $1/\Delta k$, the generated wave can drift out of phase of the driving nonlinear polarisation. In turn, this causes energy to flow from the generated field back to the input fields.

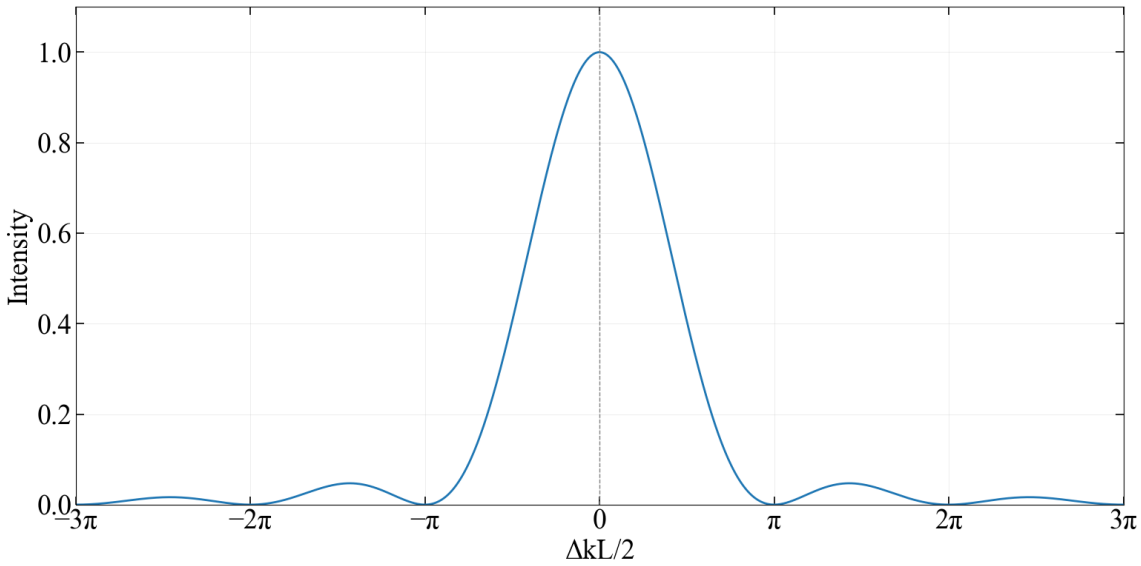

Figure 2.3 - Effect of wavevector mismatch on SFG. The intensity of the generated field follows a $\text{sinc}^2(\Delta kL/2)$ dependence where L is the interaction length and Δk is the phase mismatch.

Thus, the coherence length is defined as [24]

$$L_{\text{coh}} = \frac{\pi}{|\Delta k|}, \tag{2.23}$$

specifying the effective length over which the generated field grows constructively.

If we assume the three waves propagating collinearly in a nondispersive medium, then the phase-matching condition is simplified to

$$\frac{n\omega_3}{c_0} = \frac{n\omega_2}{c_0} + \frac{n\omega_1}{c_0}. \tag{2.24}$$

In this ideal scenario, frequency matching ensures phase matching, and it will automatically be satisfied since energy must be conserved (Eq. 2.19). In practice, since all materials are dispersive, the waves travel at different phase velocities due to the refractive index dependence on wavelength. Consequently, the phase-matching condition becomes decoupled from the frequency-matching condition and must be satisfied separately.

2.3.1 Critical Phase Matching

Careful manipulation of the refractive indices at each of the three interacting optical frequencies is therefore required. This can be achieved either through angle tuning or temperature tuning, known as critical and non-critical phase matching, respectively.

A widely adopted technique to achieve phase matching is to exploit the birefringence displayed by a host of crystals. Birefringence is when the refractive index depends on the light's direction of polarisation. Not all crystals exhibit this property, notably, those belonging in the cubic crystal system are optically isotropic and therefore cannot be phase

matched using this technique. To match the phase velocities of the interacting waves, the highest frequency wave (ω_3) is typically polarised in the direction with the lowest refractive index. This depends on the crystal.

Critical phase matching requires careful tuning of the angle between the crystal's optical axis and the direction of the incoming light. For simplicity, we will assume a uniaxial crystal which has a single optic axis, at a specific direction within the crystal. The optic axis defines the direction along which no birefringence occurs and thus light propagating in the optic axis direction, irrespective of polarisation experiences the same refractive index, which depends only on the wavelength.

For propagation at an angle to the optic axis, the electric field can be decomposed into two orthogonal components. The ordinary ray, which is light polarised perpendicularly to the principal plane, defined by the propagation vector k and the optical axis, experiences a fixed refractive index $n_{\mathbf{o}}$. On the other hand, light polarised within the principal plane, is called the extraordinary ray and experiences a refractive index $n_{\mathrm{e}}(\theta)$ that can be engineered by tuning the angle θ between the propagation vector k and the optic axis as described by

$$\frac{1}{n_{\mathrm{e}}(\theta)^2} = \frac{\sin^2\theta}{\bar{n}_{\mathrm{e}}^2} + \frac{\cos^2\theta}{n_{\mathrm{o}}^2}, \qquad \textbf{2.25}$$

where $\bar{n}_{\mathrm{e}}$ is the principal value of the extraordinary wave such that $n_{\mathrm{e}}(\theta) = \bar{n}_{\mathrm{e}}$ when $\theta = 90°$ and $n_{\mathrm{e}}(\theta) = n_{\mathrm{o}}$ when $\theta = 0°$. By varying θ, phase matching can be achieved so that the phase mismatch between the interacting waves is minimised, and the interaction length is maximised. Figure 2.4 illustrates phase-matching conditions of type-I second harmonic generation in a beta-barium borate (BBO) crystal.

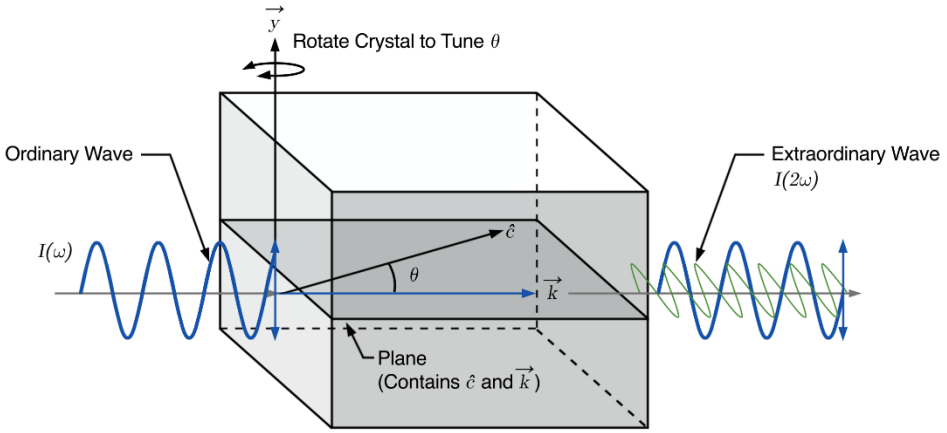

Figure 2.4 - Angle-tuned Type I phase matching for second-harmonic generation (BBO). The optic axis of the crystal is denoted by $\hat{c}$, $\vec{k}$ represents the propagation direction of the light. By rotating the crystal around the y-axis, θ is varied and therefore the refractive index of the extraordinary wave can be tuned.

In positive uniaxial crystals the extraordinary ray is slower than the ordinary ray whereas in negative uniaxial (such as BBO) crystals it is the opposite. For the two lower-frequency waves $(\omega_1 + \omega_2)$ there are two possible polarisation configurations, commonly referred to as type I and type II. In type I, both input fields have the same polarization and are orthogonal to ω_3, whereas in type II they are orthogonally polarized with respect to each other. The complete set of configurations are listed in Table 2.1 [36].

Table 2.1 Phase-matching configurations for uniaxial crystals

	Positive Uniaxial $(n_e > n_o)$	Negative Uniaxial $(n_e < n_o)$
Type I	$n_3^o\omega_3 = n_1^e\omega_1 + n_2^e\omega_2$	$n_3^e\omega_3 = n_1^o\omega_1 + n_2^o\omega_2$
Type II	$n_3^o\omega_3 = n_1^o\omega_1 + n_2^e\omega_2$	$n_3^e\omega_3 = n_1^e\omega_1 + n_2^o\omega_2$

A serious drawback of critical phase matching is spatial walk-off. For extraordinary rays, when the angle θ is neither 0°nor 90°, the direction of energy flow (the Poynting vector S) differs from that of the wavevector k. In isotropic media, these two vectors are normally collinear. However, in this case, spatial walk-off causes the interacting beams to separate spatially. This separation reduces the efficiency of the nonlinear process and introduces asymmetries that can, in some cases, compromise the expected behaviour.

2.3.2 Non-Critical Phase Matching

In some crystals, such as in lithium niobate, the amount of birefringence depends significantly on temperature, facilitating phase-matching with a fixed propagation angle ($\theta = 90°$). This is achieved by tuning the temperature of the crystal. Temperature tuning is widely employed in integrated photonic circuits where angle-tuning is not possible [37].

Birefringent phase matching is not always feasible. In some materials like gallium arsenide, birefringence is completely absent. Other materials cannot provide enough birefringence to compensate for the dispersion of the linear refractive indices across the desired spectral range. This is more prevalent for shorter wavelengths. Furthermore, some applications require the use of more efficient nonlinear coefficients (e.g. d33) which need co-polarized interacting waves and therefore birefringence phase matching cannot be employed. Quasi-phase matching (QPM) serves as a viable alternative method to constructive interference between the input fields. Instead of eliminating the phase mismatch, QPM corrects for it by periodically reversing the sign of the nonlinear susceptibility $\chi^{(2)}$ after each coherence length. Consequently, the phase relationship between the interactive waves is reset, maintaining net growth of the output field [38], as shown in Figure 2.5.

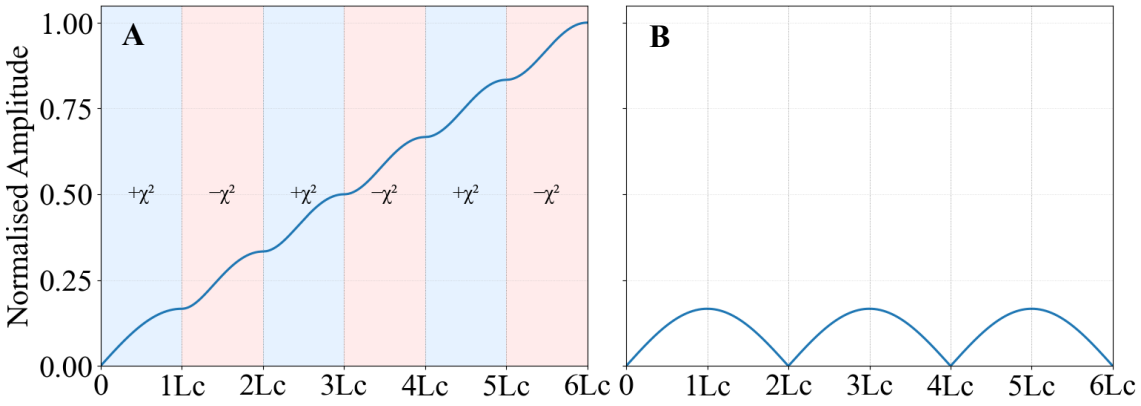

Figure 2.5 - Comparison between quasi-phase-matched and phase-mismatched interactions. **A**: periodic inversion of $\chi^{(2)}$compensates for the phase mismatch and enables continuous field growth | **B**: generated field oscillates thus has negligible net conversion efficiency. Here, L_c denotes the coherence length.

2.4 Spontaneous Parametric Down Conversion

Among the various second-order nonlinear processes, parametric down-conversion (PDC) plays a particularly significant role in this work. PDC is a second-order nonlinear process where a pump (p) photon of a higher frequency is converted into two lower-frequency photons, typically known as signal (s) and idler (i). The process is called parametric as there is no energy exchange between the photons and the medium, and "down-conversion" indicates that the output photons are lower in frequency than the input photon [39]. The frequencies, and wavevectors of the down-converted fields must satisfy Eqs. 2.19 and 2.20, so that both energy and momentum is conserved, as illustrated in Figure 2.6.

In essence, PDC can be in a way regarded to as the reverse of SHG, where instead of two lower energy photons are combined to output one of a higher frequency, a single higher-frequency photon is split into a pair that share its energy. It can also be understood as a quantum form of DFG where both output fields are generated simultaneously [40]. In classical DFG, two classical electromagnetic waves combine, generating a field oscillating at the difference of the input fields. Whereas in spontaneous parametric down-conversion (SPDC) the inputs are the pump field and quantum vacuum fluctuations. Both

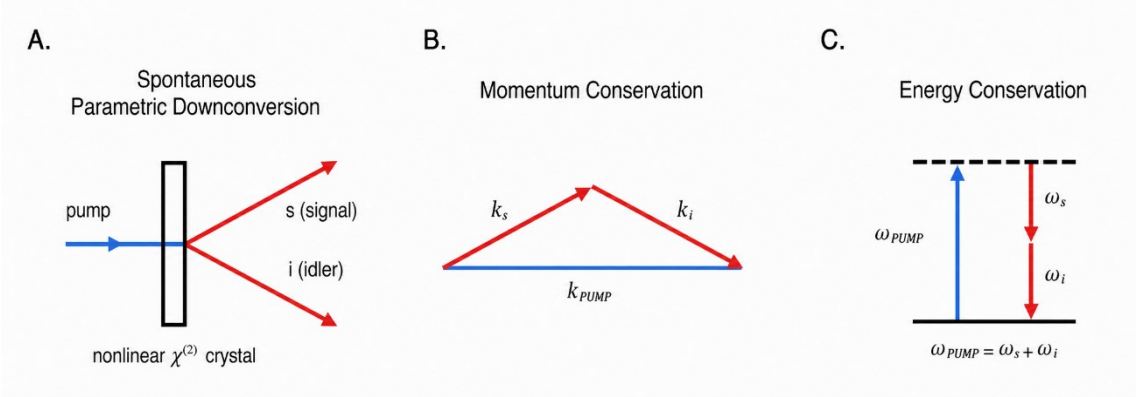

Figure 2.6 - A: In Spontaneous Parametric Down-Conversion (SPDC) a pump photon is annihilated in a nonlinear crystal, generating two lower-energy photons termed signal (s) and idler (i). | **B**: Momentum conservation requires $k_{pump} = k_s + k_i$ | **C**: Energy conservation requires $\omega_{pump} = \omega_s + \omega_i$. Diagram reconstructed from [24].

cases are driven by the same nonlinear interaction but differ in the way in that they are initiated and their output characteristics.

The efficiency of the process as well as the spectral characteristics are dictated by the phase-matching conditions as well as other physical parameters, which will be covered in more detail in the relevant sections.

2.4.1 Single-Mode Squeezing

Beyond the classical interpretation, SPDC serves as a pivotal tool for generating nonclassical states of light. It is an inherent quantum process whereby vacuum fluctuations of the electromagnetic field stimulate the conversion of a pump photon into a signal-idler pair. The generated fields exhibit quantum correlations in their photon number and anticorrelation in the phases, and the correlation properties require a quantum optical framework to be properly described. A full quantum treatment is beyond the present scope. Instead, we focus on a phenomenological description highlighting the key observable features of the generated light.

To fully appreciate the nature of PDC and how it can lead to nonclassical states of light, it is helpful to begin with the concept of a coherent state. Such states, are employed in quantum optics to approximate the output of ideal laser sources, representing minimum uncertainty states obeying the minimum uncertainty principle, $\sigma_{\mathrm{N}}{}^2\,\sigma_{\varphi}{}^2 \geq \frac{1}{4}$, where $\sigma_{\mathrm{N}}{}^2$ and $\sigma_{\varphi}{}^2$are the photon-number and phase variance respectively. In a coherent state the uncertainty is symmetrically distributed between the two conjugate variables, therefore exhibiting equal variance. These intrinsic quantum fluctuations define the shot-noise level, which manifests as residual noise even in an ideal optical field.

Shot noise, sets a limit on classical measurement precision. While it imposes a practical constraint on sensitivity, it is not a fundamental limit like the Heisenberg limit. Quantum methods, such as squeezing allow us to engineer or redistribute the uncertainty between the field quadratures, thereby supressing quantum fluctuations below the shot-noise limit [41].

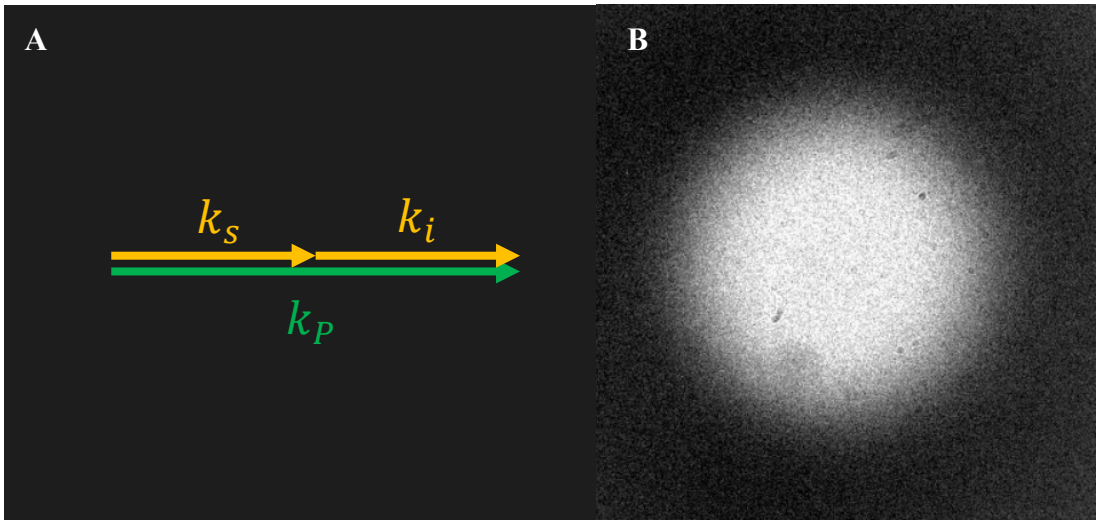

Figure 2.7 - A: In degenerate collinear SPDC, the signal and idler share equal wavevectors ($k_s = k_i$), both collinear with the pump wavevector k_p| **B**: Spatial profile of the degenerate parametric down-conversion output, measured by pumping a 1 mm BBO crystal with 515 nm pulses under collinear phase-matching conditions. A 10 nm bandpass filter centred at 1030 nm was placed in front of the camera.

Under type I (or type 0) phase-matching conditions, degenerate collinear SPDC can produce down-converted photons with identical frequency, direction and polarisation ($\Delta k = 0$), confining the quantum fluctuations to a single spatiotemporal mode. The wavevectors of this configuration are depicted in Figure 2.7A where *p*, *s* and *i* denote the pump, signal and idler respectively. The spatial profile of the output field is illustrated in Figure 2.7B.

The quantum state of the optical mode in which the photons are emitted is called "squeezed vacuum" (SV). To clarify, the vacuum state corresponds to the lowest-energy state of the electromagnetic field, thus the average number of photons present is zero. However, due to the uncertainty principle, quantum fluctuations of the electromagnetic field persist. The vacuum state represented in phase space is shown in Figure 2.8A, with the field quadrature associated with momentum and position denoted by $\hat{X}_\omega$ and $\hat{Y}_\omega$ respectively. The state's uncertainty is represented by the shaded blue region, illustrating that quantum noise is spread evenly among all quadratures.

By rotating the state's phase space with an optical frequency equal to $\omega/2\pi$, its temporal evolution may be observed. Additionally, the electric field can be analysed by observing

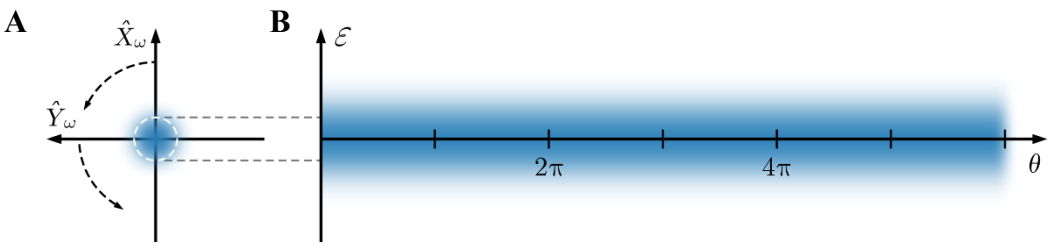

Figure 2.8 - A: Vacuum state shown in phase space | **B**: Corresponding electric field time evolution where $\theta = \omega t$. Figure reconstructed from [42].

the projection of the phasor onto a fixed vertical axis. For a vacuum state, the field fluctuations, or shot noise, remain constant, as shown in Figure 2.8B.

By employing degenerate SPDC, the quadrature uncertainties can be redistributed. Figure 2.9 illustrates this phenomenon where the momentum quadrature shows a reduction of variance (squeezing), while enlarging the other (anti-squeezing). Correspondingly, in the time-domain the electromagnetic field exhibits phase-dependent field fluctuations, with the uncertainty minimised at phases of $n\pi$.

Therefore, by employing balanced homodyne detection, one can select and measure the squeezed quadrature by tuning the phase of the local oscillator to surpass the shot-noise limit [42].

Quadrature squeezed-states have proven to be useful in surpassing classical limits of measurements with examples in spectroscopy [43] and laser-based particle tracking of living cells [44]. Moreover, such states of light have also been employed to establish secure quantum key distribution [45]. Most notably, they have been applied to gravitational wave detectors, as originally proposed in [46] and successfully realised in GEO600 [47] and LIGO [48].

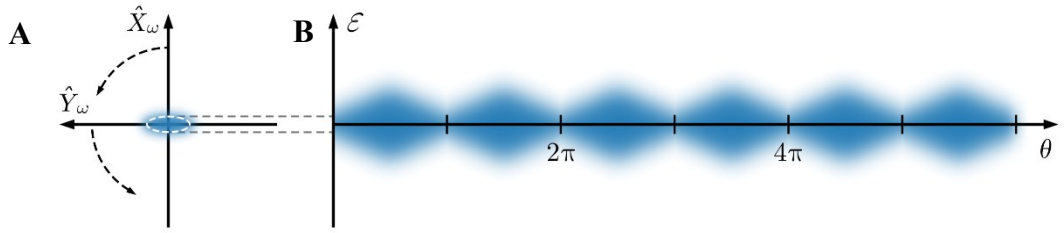

Figure 2.9 - A: Squeezed vacuum state shown in phase space | **B**: Corresponding electric field time evolution where $\theta = \omega t$. Figure reconstructed from [42].

2.4.2 Twin-Beam Squeezing

A state that is closely related in both its theoretical description and generation methods to quadrature squeezed states, is the two-mode squeezed state or otherwise, twin-beams [49].

For consistency type I phase-matching conditions are considered, as in Section 2.4.1. If angle θ between the pump field and the crystal's optic axis is tuned so that $\Delta k > 0$ then we enter the non-collinear regime of phase matching. The SPDC output is then emitted in a cone around the pump beam, producing a dark central region in the far-field spatial profile.

Radiation emitted via SPDC is fundamentally multimode, consisting of a wide distribution of both spectral and spatial modes. This occurs because of the broadband nature of vacuum fluctuations which seed the parametric process. Consequently, this leads to photon pairs being emitted into a continuum of modes which satisfy the phase-matching criteria. The continuum spans a wide angular spectrum relative to propagation axis of the pump field. The radius of the SPDC field at the far-field is determined by the phase mismatch Δk. As shown in Figure 2.10. Increasing Δk leads to a wider emission angle (at degeneracy and for the typical interaction that generates squeezed vacuum states in the near infrared).

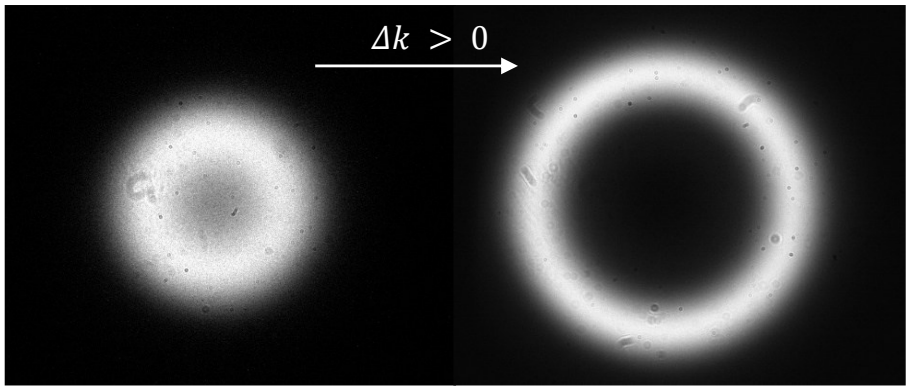

Figure 2.10 - Far-field spatial profiles of SPDC emission from a 1 mm BBO crystal, showing that increasing phase mismatch Δk broadens the emission cone. Measurements performed by pumping with 515 nm pulses under different phase-matching conditions, with a 10 nm bandpass filter centred at 1030 nm placed in front of the camera.

A key phenomenon is that the down-converted photons appear as phase-conjugate pairs. Hence, detecting photons that are at opposing points on the SPDC emission cone reveals strong correlations stemming from the energy-time and space-momentum entanglement of the down-converted pairs. Upon balanced photodetection, the statistics of the photocurrent difference of the conjugate regions exhibit quantum-noise suppression due to the photon-number correlations.

It is possible to achieve twin-beam squeezing via type-II phase matching. In this case, the signal and idler photons are orthogonally polarized, experiencing different refractive indices within the crystal. Consequently, the cone rings are centred on different propagation directions and may not overlap. The geometry of type-II SPDC emission is illustrated in Figure 2.11 [50].

In this work, we focus on employing squeezed light in the continuous-variable regime. This is consequence of previous practical limitations encountered when trying to gain a quantum advantage in THz-TDS with discrete-variable schemes [51].

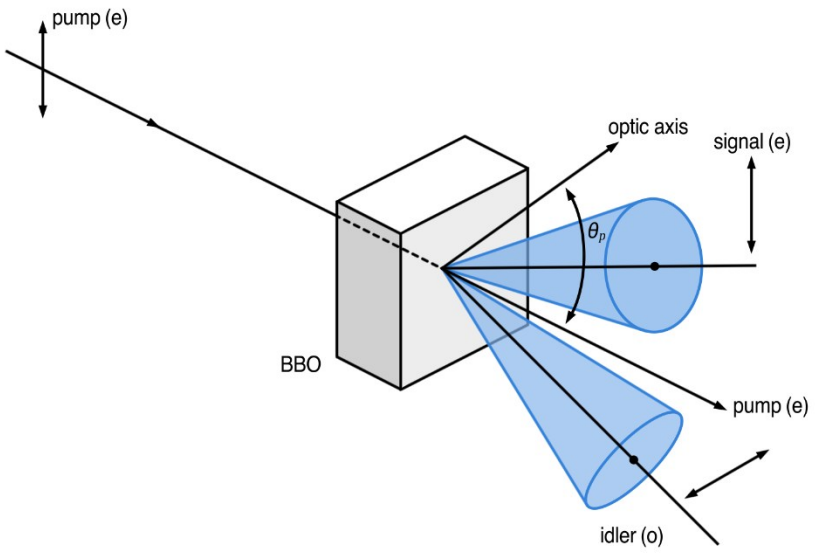

Figure 2.11 - Sketch of Type-II SPDC in a BBO crystal, where the pump (extraordinary, e) generates signal (e) and idler (o) photons with orthogonal polarisations, emitted into two distinct cones.

A significant portion of the progress within quantum-enhanced sensing has been achieved in the discrete-variable regime, where single-photon states are employed possessing well-defined photon numbers. For instance, NOON states, represented by wavefunctions of the form $(|N,0\rangle + \langle 0,N|)/\sqrt{2}$, have been employed to perform quantum-enhanced phase estimation [52]. Although remarkably precise, these approaches depend on single-photon or photon-counting detectors. Since they require to have small number of photons (typically less than one) for each acquisition, the overall number of detected photons is inherently limited. In turn, this limits the sensitivity of the measurement, which at best scales with the inverse number of measured photons.

In contrast, continuous-variable schemes employ bright optical fields, comprising many photons. Such approaches are better aligned for the objectives of this work, to improve the sensitivity of time-resolved THz electric field sensing. Previous work by our group has shown both the feasibility and limitations of performing THz sensing at the typical fluxes associated with standard discrete-variable approaches [53], motivating the use of bright-squeezed-light sources to overcome the limitations.

The first experimental realisation of squeezed light was reported in 1985 via four-wave mixing in sodium atoms [54]. Shortly thereafter, squeezed states were produced via optical parametric amplification (OPA) within an optical resonator [55]. This topology, now a well-established approach for producing squeezed light, has enabled record-breaking levels of noise suppression. Notably, Vahlbruch *et al.* [56] demonstrated 15 dB of squeezing, with Eberle *et al.* [57] also reporting an impressive 12.7 dB of squeezing. This approach underpins the squeezed light sources employed in the gravitational wave detectors.

To enhance second-order nonlinear effects, pulsed light is used to exploit its high peak power. However, despite efforts [58],[59],[60], quadrature noise suppression with pulsed systems is limited compared to that of CW systems, with the current record set at 5.88 dB [61]. While the result is impressive, it required phase stabilisation, pulse shaping and advanced mode-matching techniques aided by machine learning. This confirms that, albeit ultrafast quadrature squeezing is possible, it is experimentally complex.

Single-pass OPAs have served as a practical alternative for generating pulsed twin-beams with strong intensity correlations. Following the first experimental observation of squeezed light in 1985, Aytür and Kumar [62] published the results of the first intensity squeezing experiment employing nanosecond pulses, surpassing the quantum limit by 6 dB.

Various efforts generating pulsed twin-beams in the picosecond to nanosecond pulse duration range are limited in their power of the output fields, posing a potential limitation on the viability of such sources in differential absorption measurements, as listed in Table 2.2.In recent years, several studies have demonstrated that twin-beams can maintain quantum correlations at sub-picosecond timescales, utilising both $\chi^{(2)}$ [63] and $\chi^{(3)}$ [64] interactions.

Ultrafast twin-beam states in the near-infrared are particularly attractive, as they leverage the capabilities of established femtosecond laser sources and mature detection technologies, which offer high pulse energies, high repetition rates, and high quantum efficiency. Generating femtosecond pulses that employ strong photon-number correlations would open the way to sub-shot-noise measurements in sub-picosecond timescales without needing to average extensively. Among the aims of this thesis is the realisation and characterisation of ultrafast twin-beams tailored for quantum-enhanced differential transient absorption measurements.

Table 2.2 Pulsed twin-beam works

Paper	Pulsed Duration	NRF	Average Power [W]
Guo *et al.*, *Applied Physics Letters*, 101, 261111 (2012)	4ps	3 dB	2E-6
Smithey *et al.*, *Physical Review Letters*, 69, 2650 (1992)	300 ps	5 dB	2E-11
Iskhakov *et al.*, *Physical Review Letters*, 102, 183602 (2009)	17 ps	3 dB	1E-10
Bondani *et al.*, *Physical Review A*, 76, 013833 (2007)	4.5 ps	3.3 dB	2E-13
Brida *et al.*, *Physical Review Letters*, 102, 213602 (2009)	5 ns	1.5 dB	1E-10
Iskhakov *et al.*, *Physical Review A*, 93, 043849 (2016)	18 ps	3 dB	7.5E-11
Brida *et al.*, *Nature Photonics*, 4, 227 (2010)	5 ns	3.5 dB	5.6E-14
Jedrkiewicz *et al.*, *Physical Review Letters*, 93, 243601 (2004)	1 ps	3 dB	8.5E-18
Agafonov *et al.*, *Physical Review A*, 82, 011801(R) (2010)	17 ps	4 dB	3E-10

3 Balanced Detector Development

Before starting to investigate quantum-correlated light sources and measuring their statistical properties down to the shot-noise limit, it was imperative to ensure that the underlying detection system itself would perform in a way so that it would not be "blinded" by its noise when trying to resolve optical noise.

At high optical powers, this requirement is easily satisfied. However, as the optical power incident on the photodetector decreases, it becomes increasingly challenging to keep the electronics quiet relative to the optical noise.

Balanced detection is widely used to perform measurements at the shot-noise limit, by supressing classical amplitude fluctuations originating from the laser source or the environment. To meet the stringent requirements of this work, a custom balanced detector was developed in-house, specifically tailored to our sensitivity and bandwidth requirements. The detector was designed to maximise quantum efficiency and minimise electronic noise, allowing reliable detection and analysis of optical noise statistics.

The chapter commences with a discussion on the rationale behind using balanced detection to achieve shot-noise-limited performance. It proceeds to describe the design and experimental characterisation of the developed low-noise detector, followed by the evaluation of its figures of merit, confirming its suitability for high-precision optical measurements.

3.1 The Role of Balanced Detection in Noise Suppression

Firstly, in direct photodetection, as shown in Figure 3.1 , assuming the amplifying electronics (in this case a transimpedance amplifier) are low noise so that its noise contribution is negligible, a DC voltage will be observed at the output that is superimposed with some faster varying optical noise.

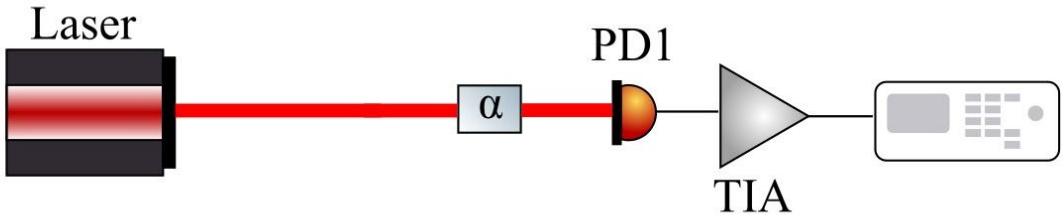

Figure 3.1 - Schematic of a setup demonstrating direct photodetection: the beam passes through an absorber (α) and is incident on a photodiode (PD1), the resulting signal is then amplified by a transimpedance amplifier (TIA).

We can paint a more intuitive picture by creating a model where, for simplicity, we consider only optical shot and flicker noise.

The voltage power spectral density due to flicker noise is described by

$$S_{\mathrm{v}}^{\mathrm{flicker}}(f) = \frac{A_{\mathrm{flicker}}^2}{f}, \tag{3.1}$$

where A_{flicker} is the amplitude of the flicker noise in $\mathrm{V}/\sqrt{\mathrm{Hz}}$ at 1 Hz and f is frequency. The total root mean square (RMS) noise from flicker can therefore be described by

$$V_{\mathrm{RMS}}^{\mathrm{flicker}} = A_{\mathrm{flicker}} \sqrt{\ln\left(\frac{f_{\mathrm{max}}}{f_{\mathrm{min}}}\right)}\ , \tag{3.2}$$

where f_{max} and f_{min} are the upper and lower limits of the detection bandwidth.

Shot-noise arises from the quantisation of the electromagnetic field. Even in the idealised case where the average photon arrival rate is steady, the number of detected photons fluctuates according to a Poisson distribution. In the context of photodetection, shot noise can be expressed as a one-sided voltage noise power spectral density so that

$$S_{\text{shot}}^2 = 2\text{q}IR^2, \tag{3.3}$$

where q is the elementary charge, I is the average (DC) photocurrent and R is the resistance of the amplifying electronics which sets the current-to-voltage gain. Thus, the RMS voltage noise is

$$V_{\text{RMS}}^{\text{shot}} = \sqrt{2\text{q}IR^2\Delta f}, \tag{3.4}$$

where Δf is the single sided detection bandwidth.

To compute the total time-domain noise, one can add the noise sources in quadrature like so

$$V_{\text{RMS}}^{\text{total}} = \sqrt{{V_{\text{RMS}}^{\text{shot}}}^2 + {V_{\text{RMS}}^{\text{flicker}}}^2}. \tag{3.5}$$

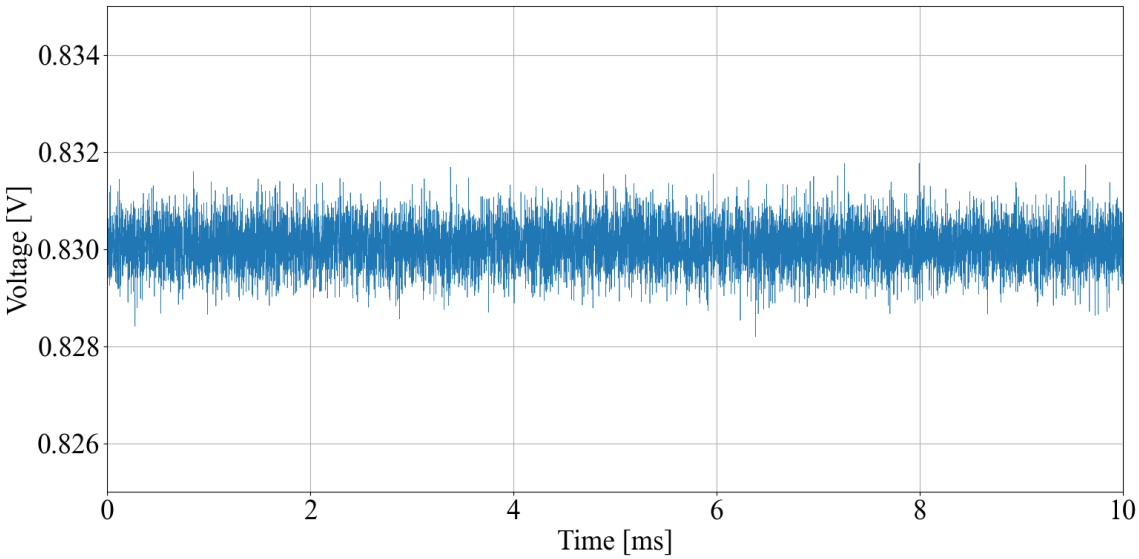

Figure 3.2 - Simulated time-domain voltage output of a modelled detector, where optical shot noise and flicker noise have been considered. A quantum efficiency of unity, a transimpedance gain of 100 kV/A, a detection bandwidth of 1 MHz, and a laser emission power of 10 mW were assumed.

Assuming a photodiode with unity quantum efficiency, a laser emitting 10 mW of optical power, and a transimpedance amplifier with gain and bandwidth of 100 V/A and 1 MHz, respectively, the output from the detector will be influenced by both shot and flicker noise. In this model, the flicker noise is arbitrarily set to $100\ \mu V/\sqrt{Hz}$ at 1 Hz. Under these conditions, the resulting amplified photocurrent is shown in Figure 3.2.

Under the same conditions, if a broadband absorber of absorbance $\alpha = 0.001$ is placed in the beam path, as shown in Figure 3.1, at $t = 5$ ms, the resultant trace would look like Figure 3.3

The signal-to-noise ratio (SNR) of Figure 3.3, based on the parameters above, is ~5. By splitting the beam with a beamsplitter and directing half of the optical field onto a second photodiode, the two photocurrents can be subtracted to perform a differential absorption measurement. This configuration, an evolution of the previous setup, is known as balanced detection, as shown in Figure 3.4.

Provided that our idealised transimpedance amplifier (TIA) can suppress common-mode signals, relative intensity noise (which includes flicker noise) and amplitude noise, are cancelled through photocurrent subtraction. Assuming the same absorber ($\alpha = 0.001$) is

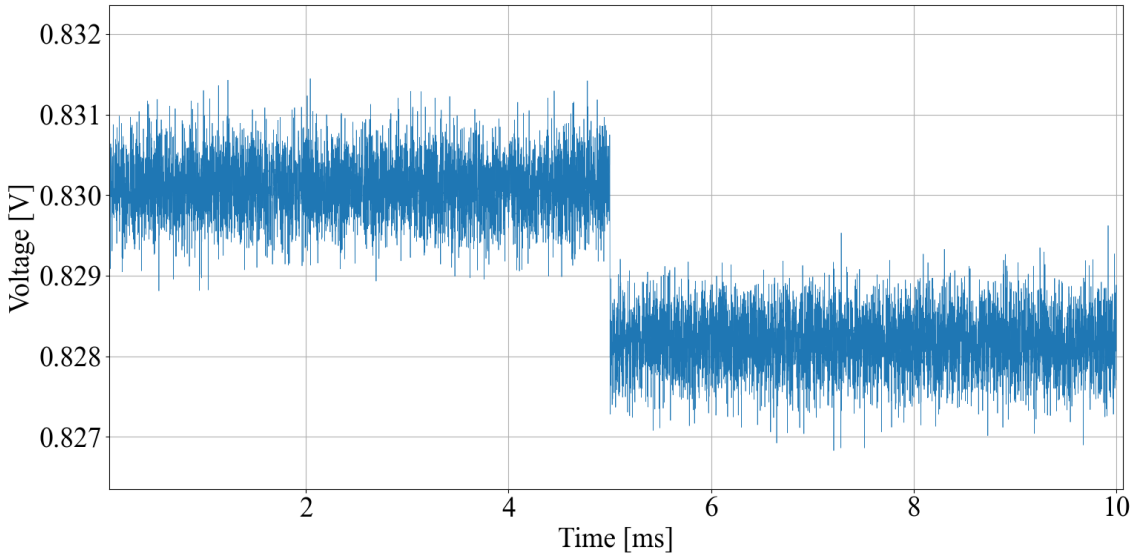

Figure 3.3 - Modelled direct absorption response. The same conditions as **Figure 3.2** apply, with a broadband absorber (α = 0.0001) is introduced in the beam path at exactly *t* = 5 ms.

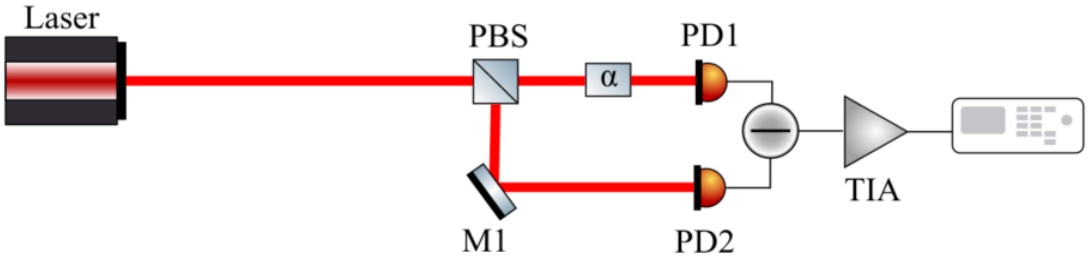

Figure 3.4 - Balanced differential absorption setup. PBS: polarising beam splitter | M1: mirror | α: absorber; PD1, PD2: photodiodes | TIA: transimpedance amplifier. The input beam is split equally by the PBS and directed onto two photodiodes. The resulting photocurrents are subtracted, suppressing common-mode fluctuations and eliminating technical noise.

introduced into one of the beam paths at $t = 5$ ms, a differential signal is induced. The corresponding response is illustrated in Figure 3.5.

The associated SNR of the trace below is 58, representing a more than tenfold increase in SNR when using balanced detection compared to direct absorption. Although this example may be somewhat idealised and exaggerated, with the flicker noise level arbitrarily selected, it highlights the motivation behind the widespread use of balanced detection, especially in systems targeting shot-noise limited detection. In the ideal case,

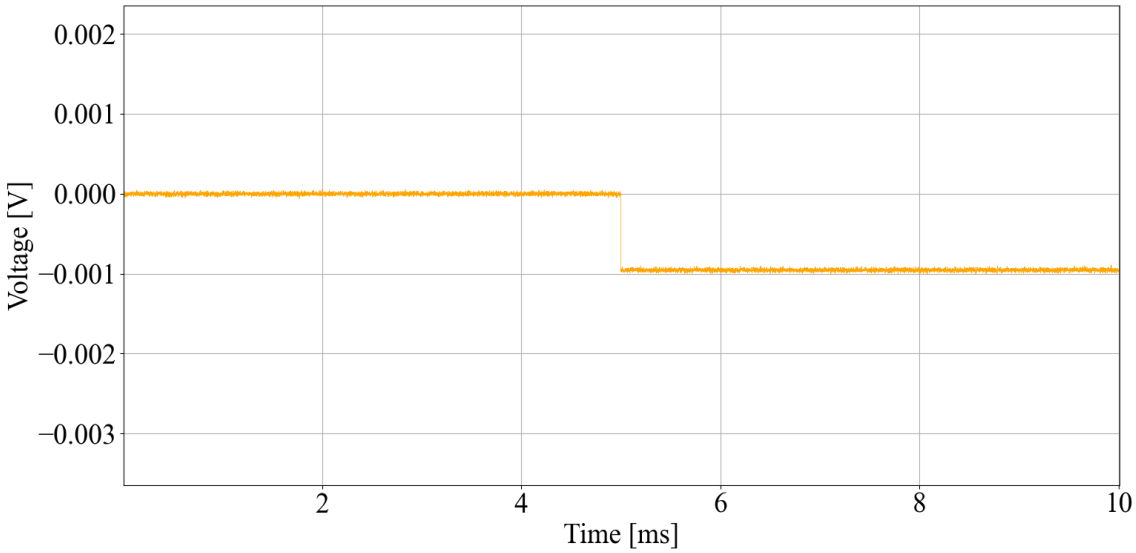

Figure 3.5 - Modelled differential absorption results. The same amount of optical power and absorbance used in **Figure 3.3** are considered here, with the difference that balanced detection is employed.

balanced detection supresses all correlated noise common to both beams thereby cancelling all common technical noise.

3.2 Design and Development of the Custom Detector

After brief survey of commercially available detectors, it became clear that a custom solution would have to be realised, due to the stringent performance requirements of this work. Detecting quantum correlations demands photodiodes with high quantum efficiency, closely matched in their responsivity and tailored to the wavelengths of interest [65]. Moreover, the detector needs to exhibit ultra-low electronic noise and offer flexibility with regards to sensitivity and bandwidth, accommodating different experimental regimes.

Transimpedance amplifiers are widely employed to convert photocurrents from photodiodes to voltage signals. Such circuits typically consist of one or more operational amplifiers (op-amps) and carefully chosen feedback components, depending on the application. Custom-designed TIAs using discrete components are possible but not considered in this work. Figure 3.6 illustrates the topology of a simple TIA circuit.

As the op-amp is operating in negative feedback, the voltage difference between the inputs must be equal. Since the positive terminal is grounded, the inverting input becomes a virtual ground, forcing the input current through the feedback resistor, resulting in an output voltage

$$V_{\mathrm{out}} = -I_{\mathrm{in}}\mathrm{R_f}\,. \qquad \textbf{3.6}$$

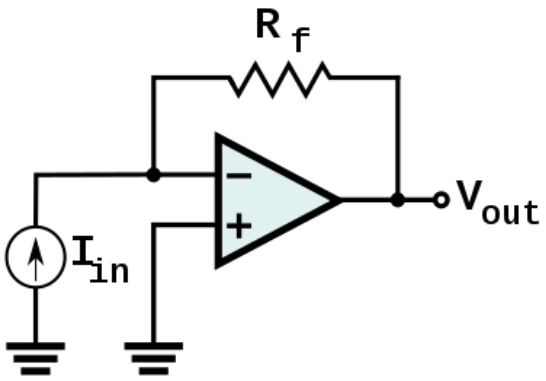

Figure 3.6 - Simplified transimpedance amplifier topology. Negative feedback forces the negative terminal to virtual ground. Current flows through the feedback resistor and is converted to a voltage.

Therefore, the transimpedance gain of the detector is set by the feedback resistor. Like all electronic components, op-amps exhibit intrinsic noise. This is typically quantified in datasheets as voltage (e_{n}) and current noise density (I_n), expressed in $\mathrm{V}/\sqrt{\mathrm{Hz}}$ and $\mathrm{A}/\sqrt{\mathrm{Hz}}$ respectively. These values, represent the root-mean-square noise per square root of bandwidth. In practical terms, it means that to compute the time-domain RMS voltage, one must integrate the voltage noise spectral density over the measurement bandwidth.

Figure 3.7 illustrates the voltage noise density of an typical op-amp. Flicker noise, or $1/f$ noise dominates at low frequencies and is a consequence of a mixture of microscopic processes within electronic devices. At higher frequencies, thermal and shot noise contribute to the white noise that usually dominates. It is imperative that we stress that the electronic shot noise stems from the quantised nature of electron flow and is distinct from optical shot noise. Similarly, the flicker noise described here should not be confused with the laser flicker noise mentioned in Section 3.1**.** Thermal (or Johnson-Nyquist) noise, however, is a consequence of the random thermal motion of carriers due to temperature.

It is also important to highlight the main goal; to amplify and measure optical shot noise which is a current noise density $\left(\mathrm{A}/\sqrt{\mathrm{Hz}}\right)$. The transimpedance amplifier will amplify this so that it appears as a voltage noise density at the output $\left(\mathrm{V}/\sqrt{\mathrm{Hz}}\right)$.

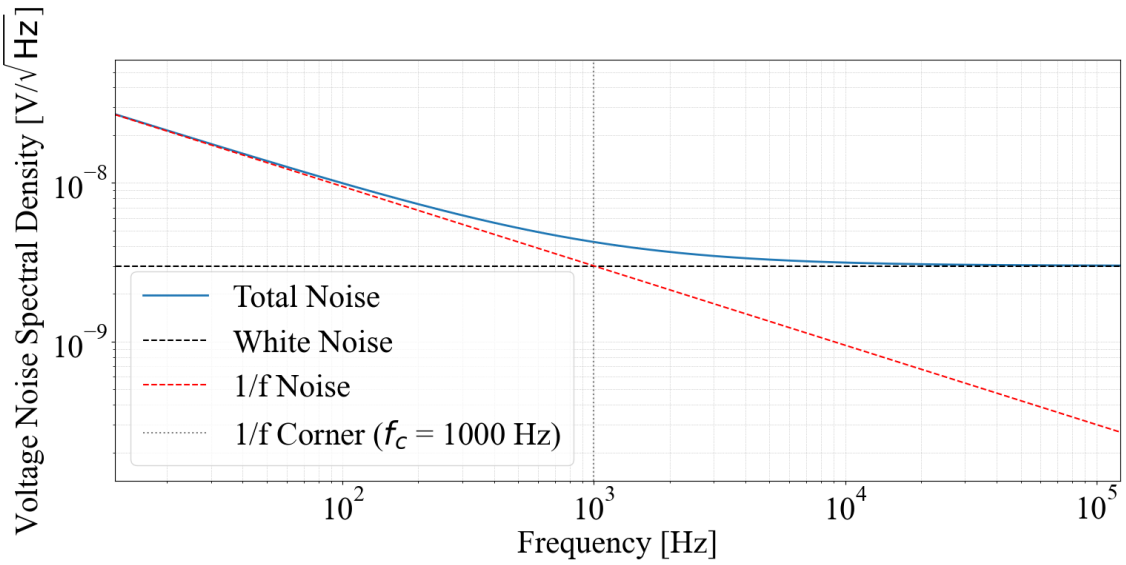

Figure 3.7 - Voltage noise spectral density of a typical operational amplifier, showing the low-frequency 1/f region dominated by flicker noise and the high-frequency white-noise floor where shot and thermal noise contribute. The two regions meet at the corner frequency f_c = 1000 Hz.

Additionally, electronically induced current noise density at the inverting input of the amplifier will be amplified in the exact same manner. It is therefore obvious that, the design goal is to maximise the optical-to-electronic noise clearance.

To achieve this, all noise contributions within the circuit must be understood, enabling the design of a low-noise system with high SNR, tailored to our measurement goals.

3.2.1 Transimpedance Amplification Theory

The topology of the circuit significantly impacts how various noise sources are amplified. Figure 3.8 depicts a representative model combining the photodiode (PD) and the transimpedance amplifier, highlighting the components and device characteristics that shape the output voltage noise.

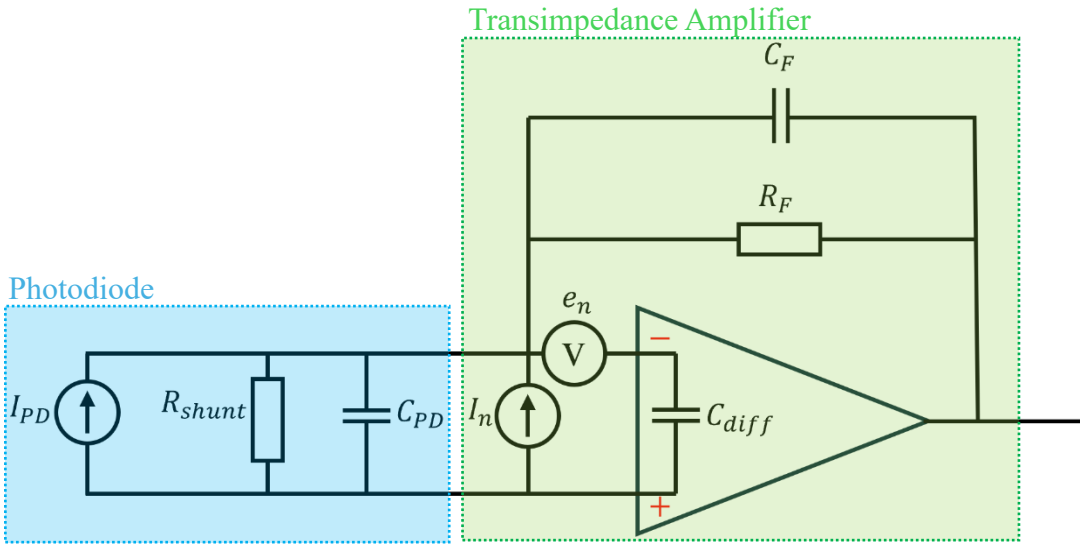

Figure 3.8 - Equivalent circuit model of a photodetector (PD) connected to a transimpedance amplifier (TIA), showing key noise sources and parasitic elements. The photodiode is modelled as a current source I_{PD} in parallel with a shunt resistance R_{shunt} and junction capacitance C_{PD}. The TIA feedback network consists of a resistor R_F, which sets the transimpedance gain, and a parallel capacitor C_F, which limits the bandwidth and ensures stability. The voltage and current noise of the op-amp are represented by e_n and i_n respectively, and C_{diff} is the inherent differential input capacitance of the amplifier.

We'll start with R_F, a pivotal component. As it was aforementioned, R_F sets the transimpedance gain of the circuit. In the context of noise, the feedback resistor generates a thermal input current noise density of

$$i_n = \frac{e_n}{R_F} = \frac{\sqrt{4kT}}{R_F} \text{A}/\sqrt{\text{Hz}}, \qquad \textbf{3.7}$$

where R is resistance, T is absolute temperature and k is the Boltzmann constant. Therefore, to minimise the generated current noise, a large feedback resistance should be chosen.

The total input capacitance (C_{in}) appearing between the amplifiers input and ground, consists of the op-amps inherent differential input capacitance (C_{diff}) and the total photodiodes' junction capacitance(C_{PD}). The value of the total capacitance plays an important role in the total output noise. The internal differential voltage noise(e_n) of the

op-amp can be modelled as a voltage source relative to the negative input terminal thereby creating an input current,

$$i_{\mathrm{n}}(t) = C_{\mathrm{in}} \frac{\mathrm{d}e_{\mathrm{n}}(t)}{\mathrm{d}t}. \quad \textbf{3.8}$$

When expressed as a noise spectral density, this becomes

$$i_{\mathrm{n}} = 2\pi e_{\mathrm{n}} C_{\mathrm{in}} f. \quad \textbf{3.9}$$

A frequency-dependent current noise, whose magnitude is determined by the total input capacitance, increasing with frequency, known as *EnC* noise [66].

The photodiodes' junction capacitance can be reduced, by operating in photoconductive mode, where both photodiodes are in reverse-biased conditions. Since this capacitance comes from the depletion region acting as a parallel-plate capacitor, increasing the reverse bias increases the separations of the "plates" and thus reducing capacitance. Additionally, PIN photodiodes which have an intrinsic (undoped) layer sandwiched between the p-n junction, have lower junction capacitance by design, and are ideal for low-noise applications.

While reverse biasing effectively reduces junction capacitance, it introduces a drawback, an increase in dark current. Dark current, which flows even in the absence of light, originates from the thermal excitation of electrons across the semiconductor bandgap. When reverse bias is applied, the depletion region is widened. Although this region is depleted of free carriers, electron-hole pairs can still be thermally generated within it. So, by increasing its volume, the number of thermally excited carriers increases. Additional contributions may arise from surface leakage, edge leakage, and when large reverse bias is applied, even tunnelling. The dark current's temperature dependence is determined by the underlying mechanism. In the most common case, where thermal generation within the depletion region dominates, the dependence is strong, and cooling significantly reduces the dark current [67].

As already established, current noise sources are amplified by the transimpedance gain. In contrast, the op-amp's input voltage noise, which appears differentially between the inputs, is amplified by the noise gain transfer function. Under the assumption of infinite open-loop gain $A_{\mathrm{OL}}(j\omega)$, the noise gain is described by [68]:

$$\text{Noise Gain}(j\omega) = 1 + \frac{Z_{\mathrm{f}}(j\omega)}{Z_{\mathrm{in}}(j\omega)} = \frac{1}{\beta(j\omega)}, \tag{3.10}$$

where

$$Z_{\mathrm{f}} = \frac{R_{\mathrm{f}}}{1 + j\omega R_{\mathrm{f}} C_{\mathrm{f}}}, \tag{3.11}$$

$$Z_{\mathrm{in}} = \frac{R_{\mathrm{PD}}}{1 + j\omega R_{\mathrm{PD}} C_{\mathrm{in}}}, \tag{3.12}$$

and β is the feedback factor, which represents the portion of output signal that is fed back into the op-amp's input. Eq. 3.10 can be written as pole-zero form as follows:

$$v_{\mathrm{n}}^{\mathrm{out}} = \frac{1 + j\omega R_{\mathrm{f}}(C_{\mathrm{in}} + C_{\mathrm{f}})}{1 + j\omega R_{\mathrm{f}} C_{\mathrm{f}}} v_{\mathrm{n}}^{\mathrm{in}}, \tag{3.13}$$

where $v_{\mathrm{n}}^{\mathrm{out}}$ is the circuit output noise, and $v_{\mathrm{n}}^{\mathrm{in}}$ is the inherent voltage noise of the op-amp. From Eq. 3.13, the zero and pole frequencies can be extracted as $f_{\mathrm{z}} = 1/(2\pi R_{\mathrm{f}}(C_{\mathrm{in}} + C_{\mathrm{f}})$ and $f_{\mathrm{p}} = 1/(2\pi R_{\mathrm{f}} C_{\mathrm{f}})$ respectively. Figure 3.9 shows the noise gain of a typical transimpedance amplifier circuit where the pole and zero frequencies are annotated.

Therefore, this gain profile determines how the input voltage noise density is amplified. As expected, it is not amplified indefinitely beyond $\mathrm{f_p}$ as the circuit's bandwidth eventually limits the response.

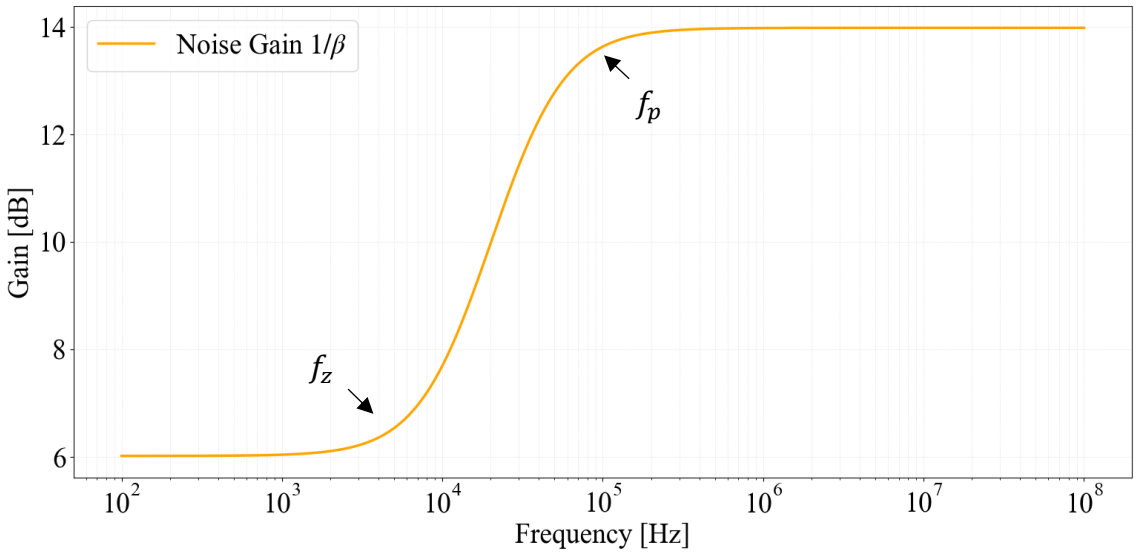

Figure 3.9 - TIA Noise Gain ($1/\beta$) profile of an arbitrary TIA, showing the characteristic zero and pole frequencies.

The noise gain does not only determine how the input referred noise is amplified, but it also serves as a tool when investigating the circuit's stability.

The feedback systems work based on the loop gain which is defined as

$$A_{\mathrm{OL}}(j\omega) \cdot \beta(j\omega). \qquad \textbf{3.14}$$

The open-loop gain $A_{OL}(j\omega)$ refers to the gain of the op-amp when no feedback is applied, and it is typically specified by the manufacturer.

The intersection points between the noise gain curve ($1/\beta(j\omega)$) and the open-loop gain corresponds to the frequency when the loop-gain equals one. Also referred to as the gain - crossover frequency, where the magnitude of the loop gain is 0 dB. This frequency plays a critical role in the stability analysis of the circuit. Fundamentally, feedback serves as an error correction mechanism where the output of the amplifier is compared to the input (through feedback), and the output is then corrected, minimising the difference error. However, the op-amp and the feedback signal introduce delays which correspond to a phase shift between the input and the feedback signal. If the phase shift is small, the correction signal arrives in time and helps reduce the error, this is stable feedback.

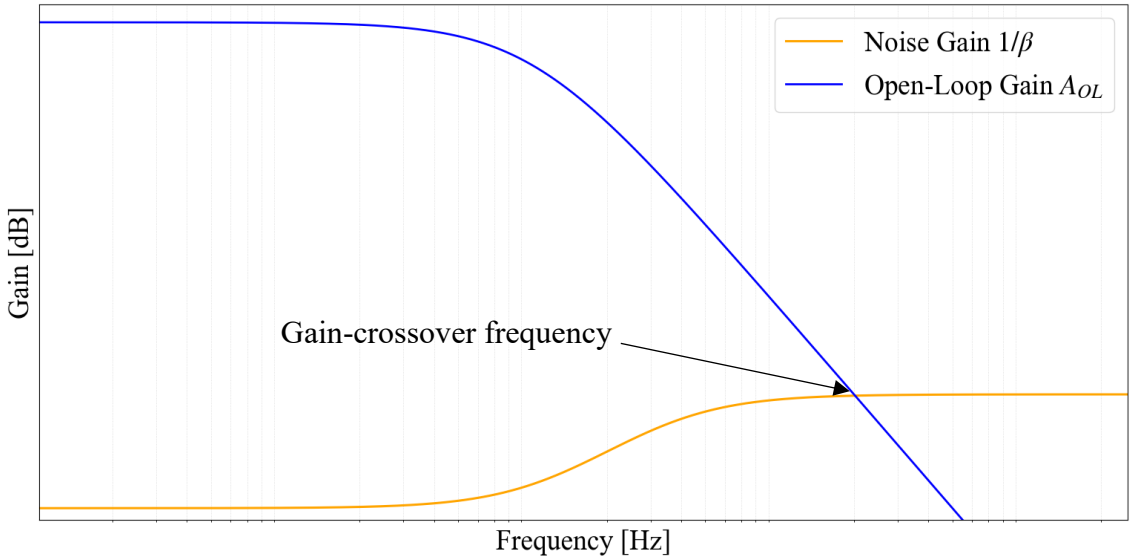

Figure 3.10 - Open-loop gain and noise-gain profiles of a transimpedance amplifier. The gain-crossover frequency is annotated, where the circuit is most susceptible to phase shifts and consequently to instability.

At the gain-crossover frequency, the system is particularly sensitive to phase shifts. This is because the feedback no longer has the gain to "overpower" the delays. So, if the signal frequency is close to the gain-crossover frequency and the phase shift at this point is close to 180°, the feedback becomes positive, causing oscillations and instability. This is why it is important to evaluate the phase margin at the gain-crossover frequency, the circuit's most vulnerable region.

A large phase margin means the feedback is "on time" and of the correct polarity, ensuring stability. This is illustrated in Figure 3.10 where the noise gain and the A_{OL} is plotted for an arbitrary TIA circuit using an arbitrary op-amp, the gain-crossover frequency is annotated [69].

3.2.2 Ultra-low-noise TIA Design

Now that the TIA details have been introduced in Section 3.2.1, I will report on the design, thought process, and the decision-making process I have employed to design the ultra-low-noise TIA required for sub-shot-noise measurements. The first point that needed to

be addressed is the transimpedance gain. The value of the feedback resistor plays a significant role in the input-referred current noise. Therefore, the target is to design and build a detector with the highest sensitivity and lowest noise possible. If required, the feedback resistance can be later reduced. Flexibility is one of the advantages of opting for a custom solution, as it allowed me to alter the detector, depending on the experimental conditions. A feedback resistance of 1 GΩ was chosen, which from Eq. 3.7 it can be deduced that it generates a current noise of 4.07 $\mathrm{fA}/\sqrt{\mathrm{Hz}}$.

The feedback capacitance is aimed to be kept at around 100 fF, which in combination with the feedback resistance would limit the bandwidth of the detector to ~1.6 kHz, as

$$f_{3\ \mathrm{dB}} = \frac{1}{2\pi R_f C_f}. \qquad \textbf{3.15}$$

Since the objective is not to resolve events on a pulse-by-pulse basis, the bandwidth of the amplifier is sufficient. What matters is to maximise the optical shot noise to electronic noise clearance within this bandwidth, requiring high transimpedance amplification, and low electronic noise.

Next, the op-amp had to be selected. Two candidates were considered, the LTC6268-10 by *Analog Devices* and the OPA827 by *Texas Instruments*. Both exhibit low current-noise density. The LTC6268-10 is a much faster device, making it ideal for high-bandwidth applications. It also exhibits very low differential-input capacitance, minimising the op-amp's contribution to input current noise, in accordance with Eq. 3.9. The figures of merit are summarised in Table 3.1.

Table 3.1 Op-amp figures of merit

	OPA827	LTC6268-10
Input Current Noise Density [$\mathrm{V}/\sqrt{\mathrm{Hz}}$]	2.2 $\mathrm{fA}/\sqrt{\mathrm{Hz}}$ @ 1 kHz	7 $\mathrm{fA}/\sqrt{\mathrm{Hz}}$ @ 100 kHz
Differential Input Capacitance	9 pF	0.1 pF
Gain Bandwidth Product	22 MHz	4 GHz

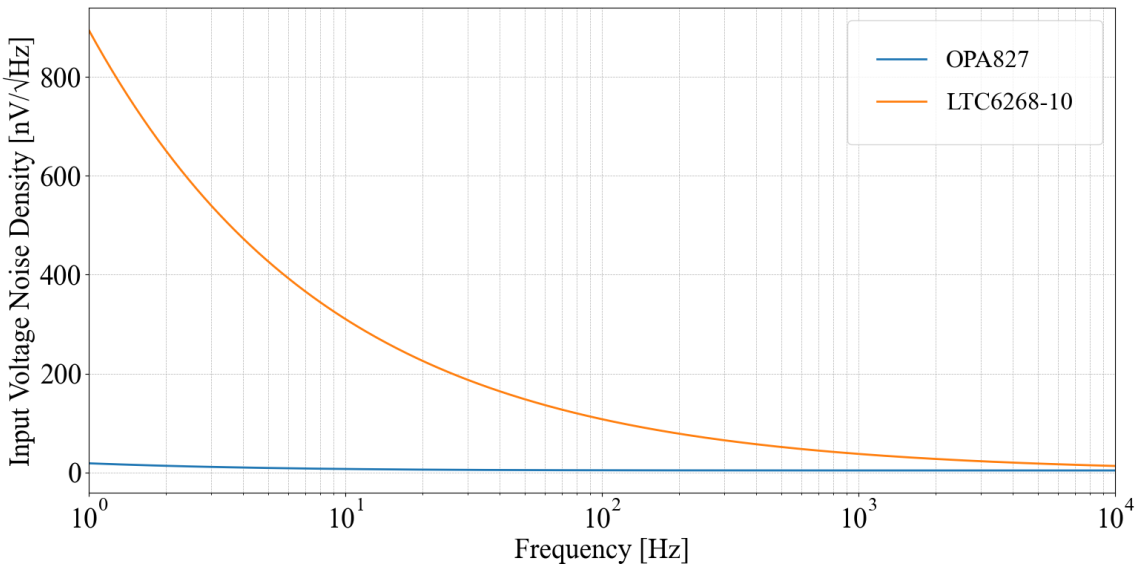

Figure 3.11- Input voltage noise density of the two op-amp candidates. Values were extracted from simulations using LTspice (LTC6268-10) and TINA-TI (OPA827).

The LTC6268-10 does have one parameter that, at first glance, may suggest it is unsuitable, its relatively poor 1/f voltage noise. The input-referred voltage noise for both devices is compared in Figure 3.11. To extract input noise, the circuits shown in Figure 3.12 were employed, where each device was simulated in a voltage-follower configuration. The simulations of the LTC6268-10 and the OPA827 were carried out using *LTspice* and *TINA-TI*, respectively, where manufacturer-supplied SPICE macromadels were imported. These macromodels comprise of the device's noise characteristics, as specified in the datasheets. To perform a noise analysis in the small-signal domain, the simulator accounts for all contributing noise sources and propagates them to the output. In the voltage-follower configuration, there are no external components, and the closed-loop gain is unity. Therefore, the input-referred voltage noise is directly represented by the output-noise spectral density.

To understand the contribution voltage-noise has on the performance, the input-referred voltage noise must be multiplied by the noise gain of the circuit. For this reason, arbitrary photodiodes were assumed in the initial simulation, with junction capacitances of 10 pF and shunt resistances of 500 MΩ. These values are typical for PIN photodiodes with an active area of approximately 500-1000 µm in diameter.

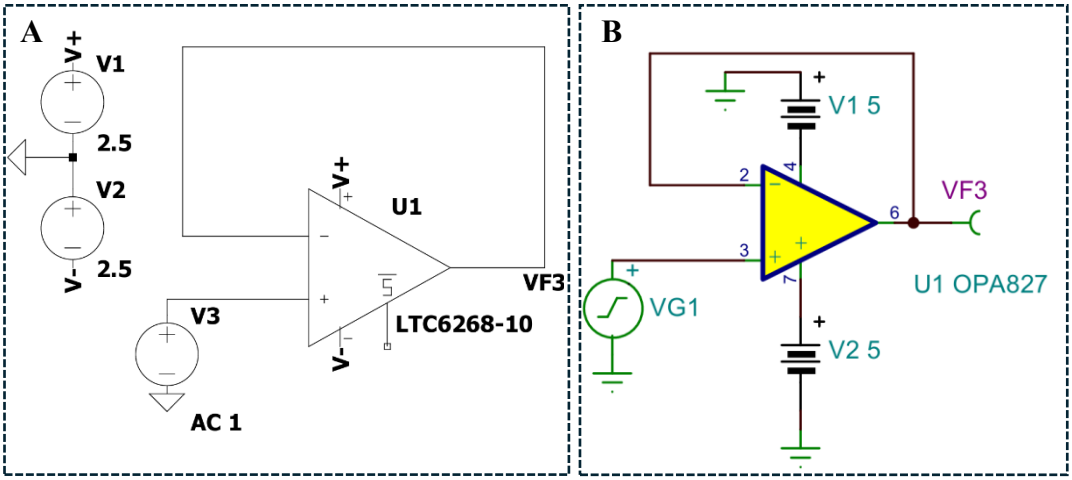

Figure 3.12 - Simulation circuits used to obtain the noise data shown in **Figure 3.11**. **A**: LTspice simulation setup | **B:** TINA-TI simulation setup.

Although the specific photodiodes had not yet been identified at this stage of the design, the expected size and type were known, allowing for reasonable estimations. The noise gain was computed in accordance with Eq. 3.10 and plotted together with the voltage noise of the associated op-amp. Figure 3.13 shows the data obtained from the LTC6268-10 simulations, while Figure 3.14 shows the corresponding results for the OPA827.

Finally, to evaluate the contribution of the voltage noise and determine whether there is a significant discrepancy in the output noise due to the inherent voltage noise, the input

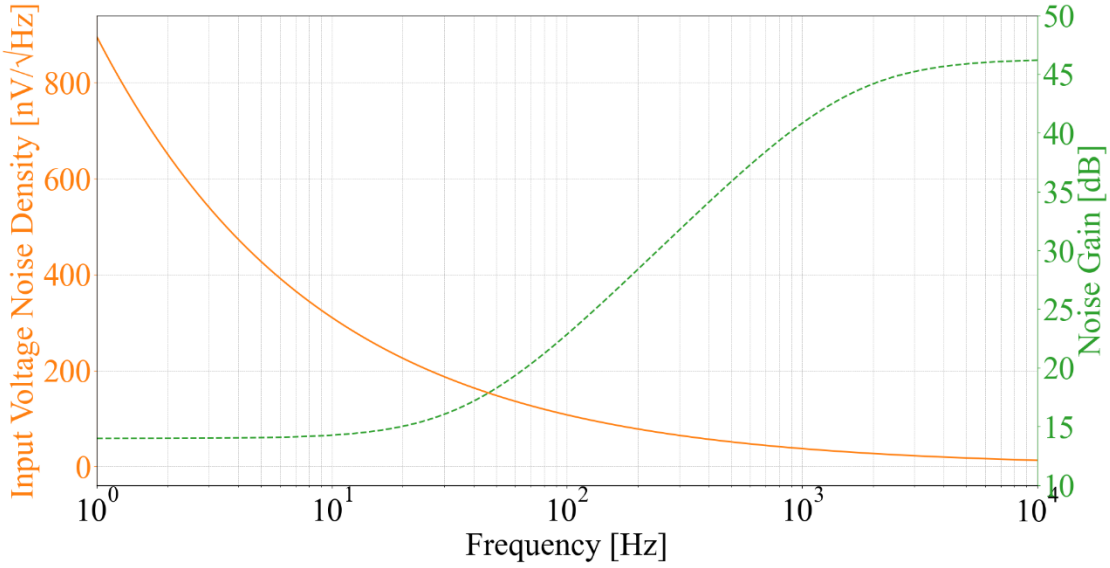

Figure 3.13 - Simulated input voltage noise and noise gain profiles for the LTC6268-10 op-amp. The output noise contribution due to the op-amp's input voltage noise is proportional to the product of these two quantities.

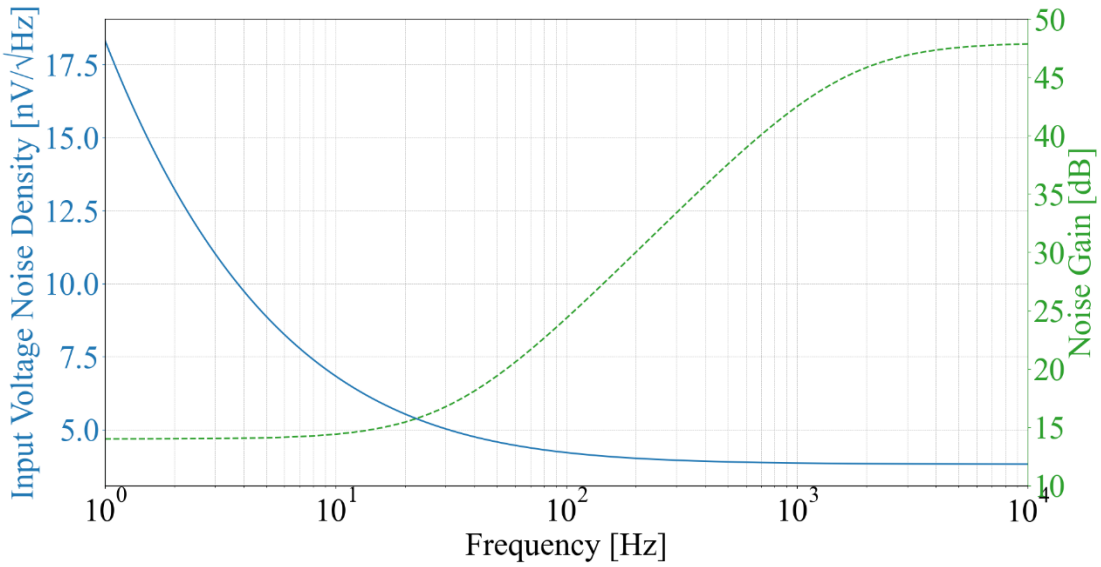

Figure 3.15 - Simulated input voltage noise and noise gain profiles for the OPA827 op-amp. The output noise contribution due to the op-amp's input voltage noise is proportional to the product of these two quantities.

voltage noise was multiplied by the associated noise gain. This was done for both devices, and the results are compared in Figure 3.15. It is evident that the noise arising from the product of the noise gain and voltage noise of the LTC6268-10 is significantly larger than that of the OPA827.

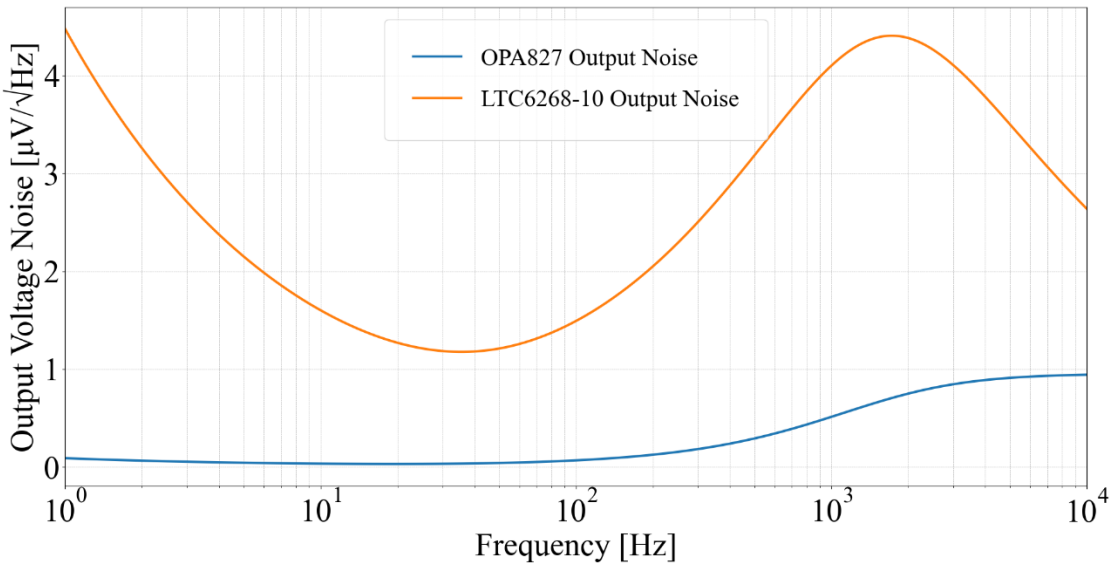

Figure 3.14 - Simulated output voltage noise due to the product of noise gain and input voltage noise for the OPA827 and LTC6268-10 operational amplifiers. Two photodiodes per simulation were considered with junction capacitance of 10 pF and shunt resistances of 500 MΩ.

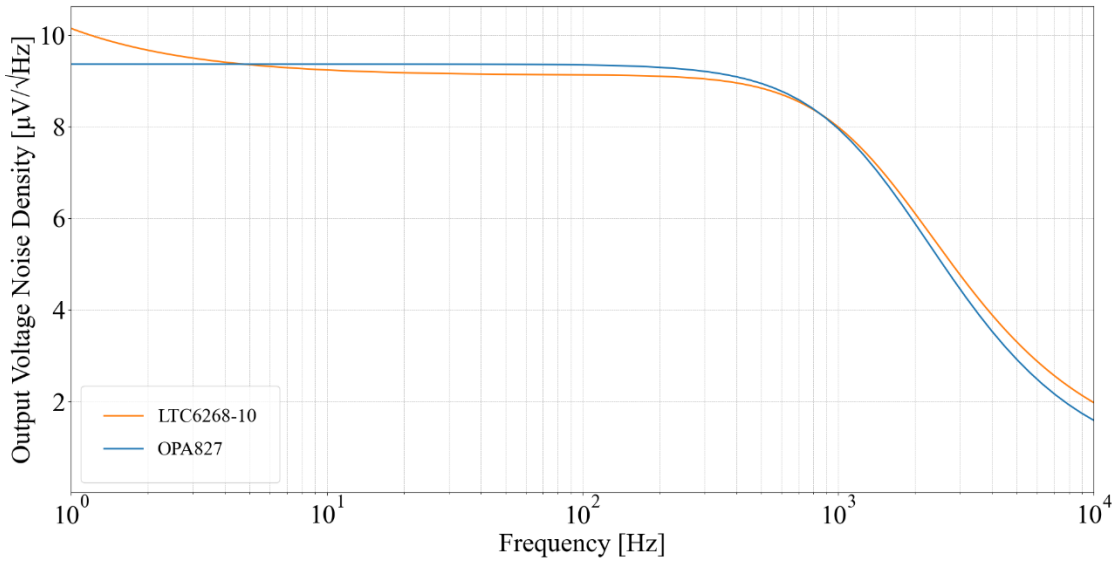

Figure 3.16 - Total simulated output voltage noise density for the OPA827 and LTC6268-10 transimpedance amplifiers, with all noise contributions considered. Two photodiodes per simulation were considered with junction capacitance of 10 pF and shunt resistance of 500 MΩ each.

For comprehensive analysis, full noise simulations were performed with the aid of *LTSpice* and *TINA-TI* where all noise sources were considered. The results are presented in Figure 3.16. Under the assumed photodiode conditions of $R_{\text{shunt}} = 500$ MΩ and $C_{\text{PD}} = 10$ pF the noise performance is nearly identical.

To establish which of the two op-amps is the more robust, the capacitance of the photodiodes was increased to 50 pF to ascertain which circuit is most sensitive to the (at that point) unknown parameters of the photodiodes. Resulting comparison is shown in Figure 3.17. Based on these findings, the OPA827 was selected for this application due to its ability, based on simulations, to maintain performance despite the uncertainties in photodiode parameters. This approach would result in a more future-proof design, as it would be very cumbersome if the photodiodes were to change in the future (for example, to operate at different wavelengths) and the noise performance were to deteriorate as a result. The circuits used in *TINA-TI* and *LTspice* for the full simulations are depicted in Figure 3.18, were R_{shunt} and C_{PD} can be adjusted to evaluate the output voltage noise depending on the photodiode parameters.

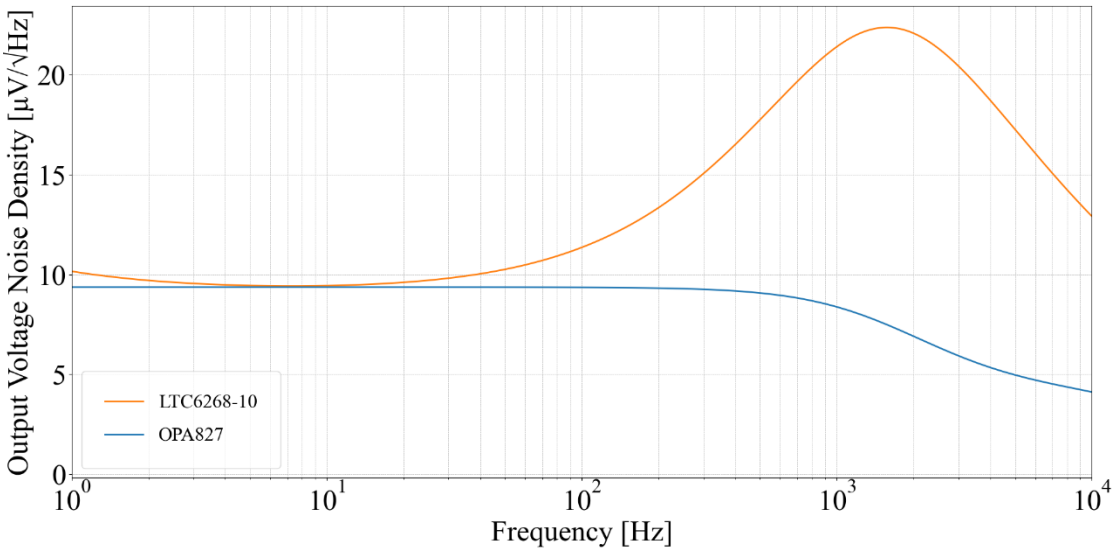

Figure 3.17 - Full noise simulation results for the OPA827 and the LTC6268-10 transimpedance amplifier with all noise contributions considered. The photodiode junction capacitance has now increased to 50 pF(each) to evaluate the robustness of the transimpedance circuit.

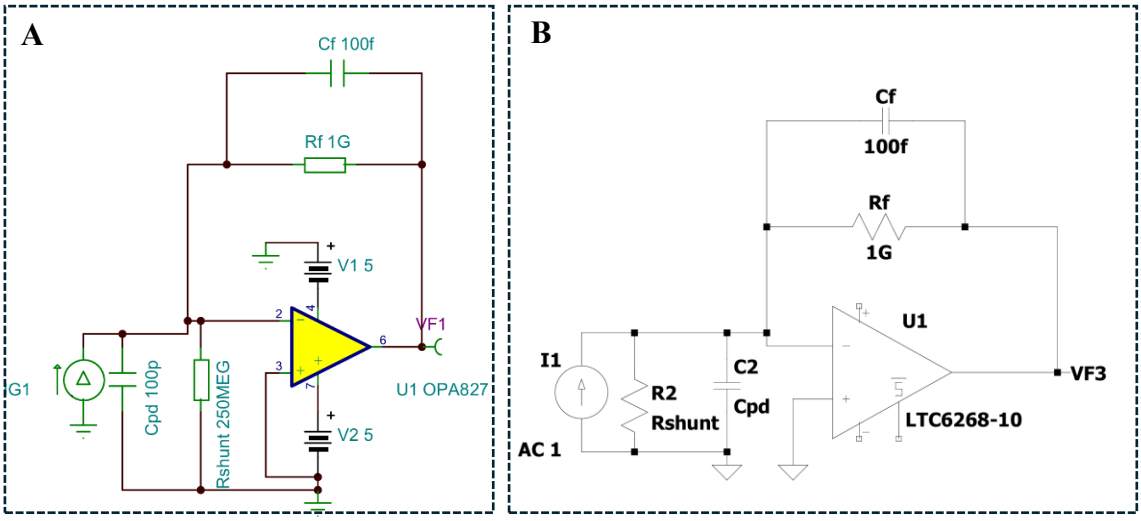

Figure 3.18 - Circuits used for the full simulations. **A**: TINA-TI simulation setup. | **B:** LTspice simulation setup. R_{shunt} and C_{PD} were adjusted according to the text.

While no stability issues were foreseen, due to the moderate speed of the OPA827, a stability analysis was performed using Tina-TI simulation software and the circuit in Figure 3.19, where the feedback loop has been broken, enabling the evaluation of the open-loop transfer function and the noise gain.

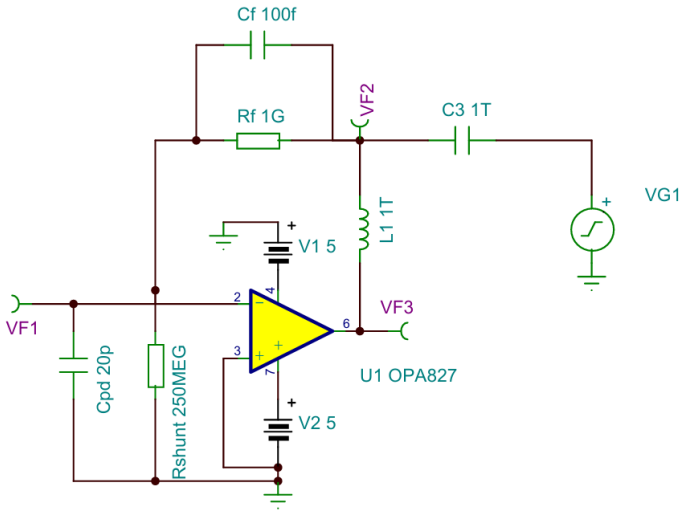

Figure 3.20 - Circuit used in TINA-TI to evaluate the stability of the transimpedance amplifier with the OPA827. The feedback loop is broken via L1, allowing the evaluation of the open-loop transfer function and noise-gain.

As shown in Figure 3.20, the loop-gain (Eq. 3.14) reaches 0 dB at 95.9 kHz. The corresponding phase margin of the loop-gain is 89°, representing a strongly overdamped response and thus ruling out any practical stability issues. On the photodiode front, it was decided that a custom solution would also be implemented, to meet the demanding performance requirements. Maximising the quantum efficiency was crucial so that quantum correlations are preserved by minimising the detection losses.

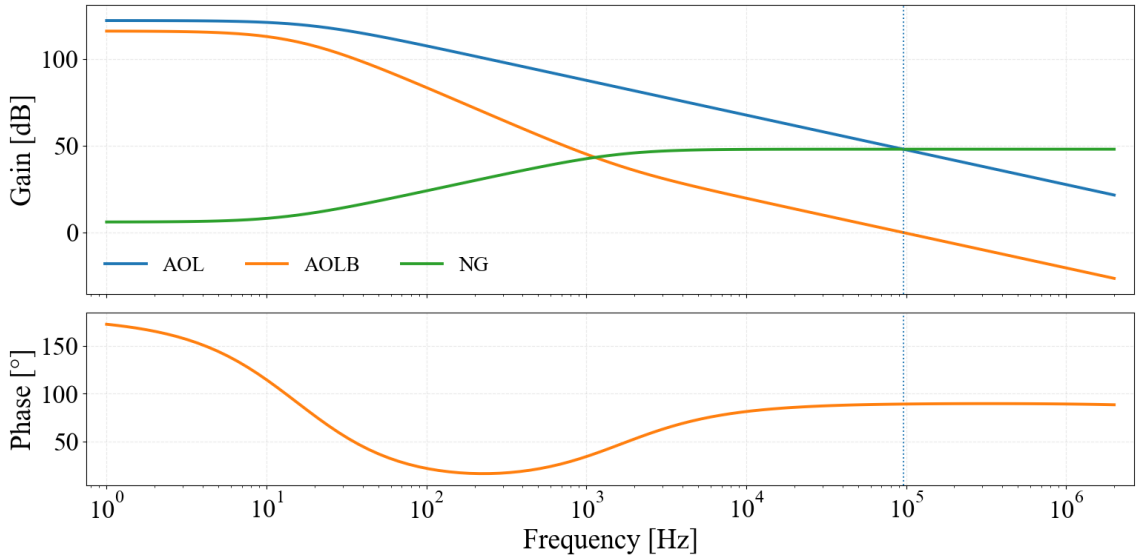

Figure 3.19 - Bode plot of the loop gain for phase margin evaluation. AOL: open-loop gain | AOLB: loop gain | NG: noise gain. The loop gain reaches 0 dB at 95.9 kHz with a phase margin of 89°, indicating a strongly overdamped and stable response.

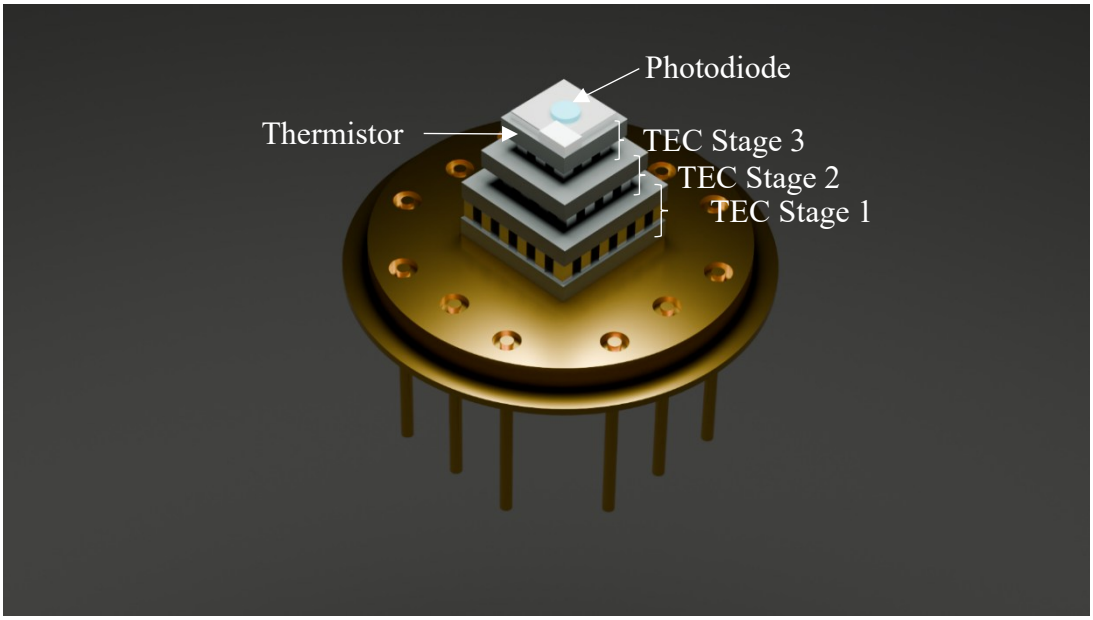

Figure 3.21 - 3D model the BayPhotonics photodiode assembly featuring three-stage thermoelectric cooling.

Moreover, minimising the dark current was also a priority as it directly impacts the noise floor. Consequently, active cooling of the photodiodes was essential. The photodiodes are InGaAs-based detectors, selected for their high responsivity at the target wavelength of 1030 nm. The dies were supplied by Fraunhofer, with an active area diameter of 750 µm and a specified quantum efficiency exceeding 90 %. However, limited additional information was provided such as capacitance and dark current.

The photodiodes were wire bonded and hermetically packaged in a TO-8 by *BayPhotonics*, a specialist photonics packaging company, based in the UK. The TO-8 package also included three-stage thermoelectric cooling with maximum voltage and current ratings set at 2.2 V and 2.4 A respectively. The package also includes a thermistor (10 kΩ at 25 C°), which allowed us to test the cooling capabilities. A model of the device is shown in Figure 3.21, illustrating the three-stage thermoelectric cooling (TEC) system.

The device has six electrical connections: two for the photodiode (anode and cathode), two for the TEC (+/−), and two for the thermistor. The top-view schematic of the device (Figure 3.22) illustrates all the connections; pins marked with a red ‘X’ are NC (no connection).

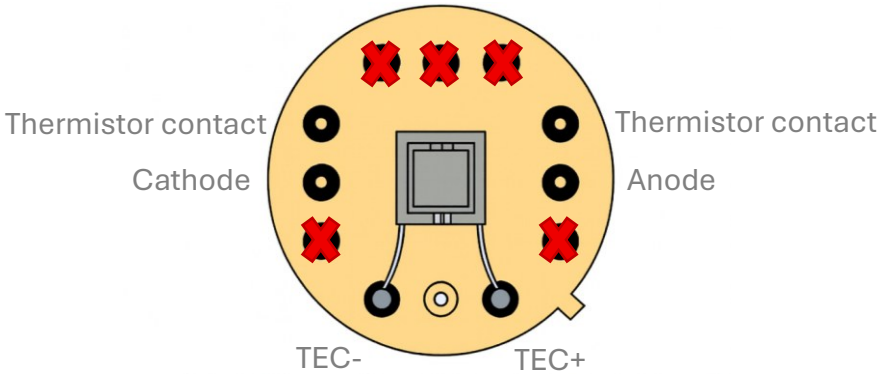

Figure 3.22 - Top view schematic of the thermoelectrically cooled photodiode.

With the key parameters such as transimpedance gain, op-amp selection and photodiodes determined, the detector schematic design could commence. Two key requirements were set for the power distribution design: (a) stable, low-noise bias voltages for the photodiodes (for reverse biasing), and (b) appropriate voltage supply for the op-amps.

Two op-amps were used in total. An additional buffer stage was implemented using the OPA277, which isolates the TIA from the load and improves the circuit's ability to drive higher capacitive loads, such as longer BNC cables. The unity gain buffer presents a very high impedance to the TIA output and a low impedance to the load, preventing capacitive loading from influencing the TIA's feedback network.

To power the op-amps, two low - dropout voltage regulators were chosen, the XC6705B501MR-G by *Torex Semiconductor* and the ADP7182AUJZ-5.0 by *Analog Devices*, providing stable +5 V and -5 V supply rails, compatible with both op-amps. The required input and output capacitors, as specified in the respective datasheets, were added to ensure low-noise and stable operation. The regulator circuitry is shown in Figure 3.23A with the +Vin and −Vin inputs supplied via a benchtop power supply.

To reverse bias the photodiodes, LM4040 Precision Micropower Shunt Voltage Reference by *Texas Instruments* were chosen. These simple devices provide stable, low-noise and accurate bias voltages whilst needing little current. Another great advantage is that these devices are available at multiple fixed-output voltages (e.g., 2.048 V, 4.096 V, 5.0 V, etc.). Thus, by replacing the device and the current-limiting resistors (6.04 kΩ in the present

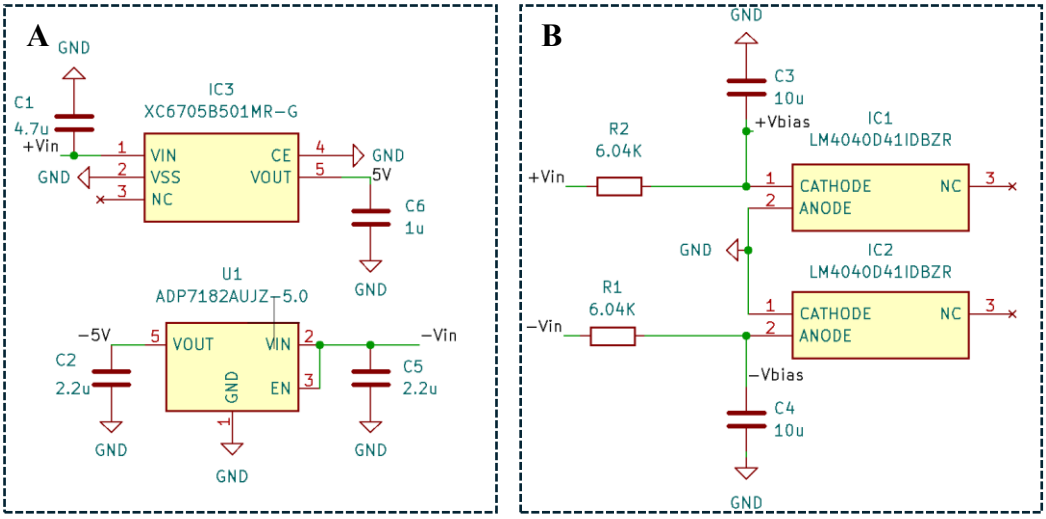

Figure 3.23 - Power distribution integrated chips. **A**: Voltage rails supplying +-5V to the circuit | **B**: Voltage references supplying bias voltage to the photodiodes.

schematic) the photodiode biasing conditions can be changed without redesigning the circuitry. The implementation of the voltage references is shown in Figure 3.23B. The bias voltages are subsequently heavily filtered using three-pole low-pass filters (1.28 Hz 3 dB bandwidth), to prevent any noise coming from the LM4040 reaching the photodiodes. Since the thermoelectric cooling requires a lot of current, it is powered directly from a benchtop power supply (TEC+/- on the schematic). The filters and the photodiode connections are depicted in Figure 3.24.

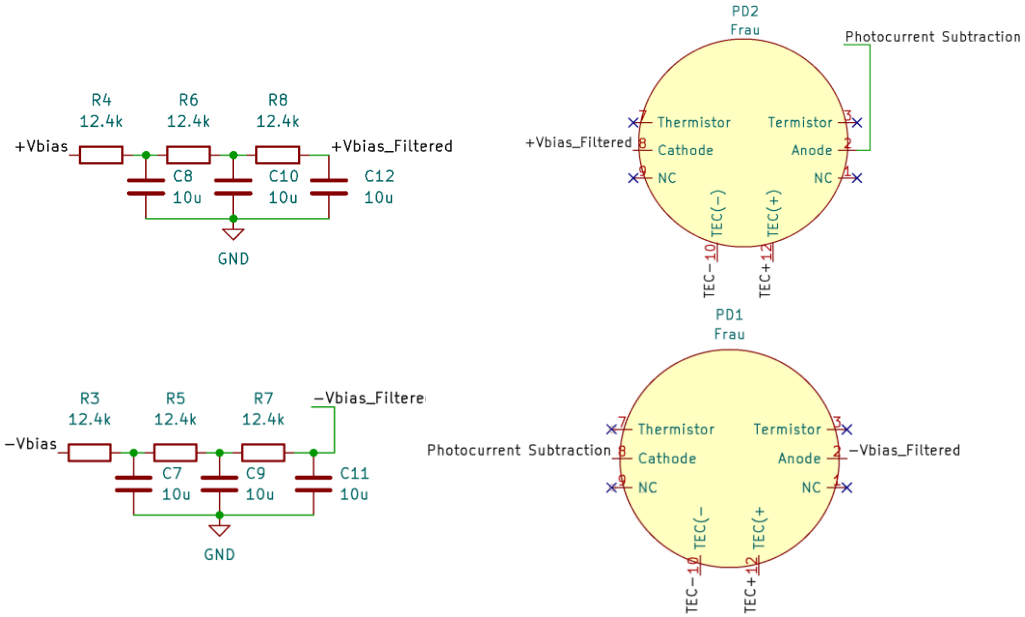

Figure 3.24 - Three-pole low pass filters and corresponding photodiode connections. Filtered bias voltages are supplied to the photodiodes through the RC networks.

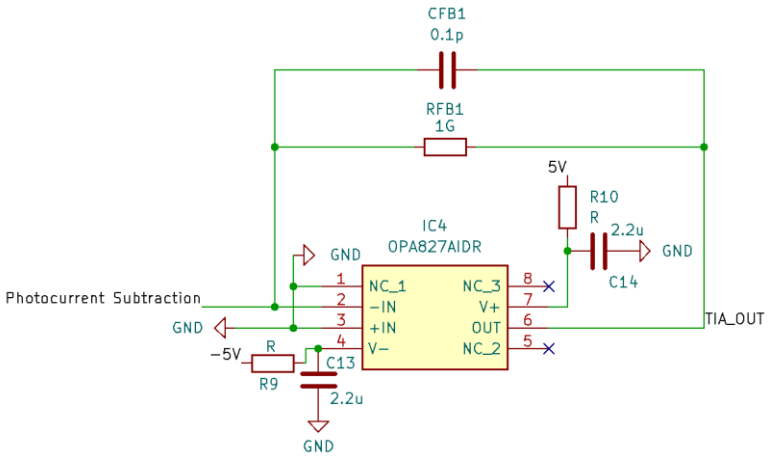

Figure 3.25 - TIA stage based on the OPA827 op-amp. R9 and R10 combine with C13 and C14 respectively to form a low-pass filters, attenuating any potential high-frequency noise on the supply rails. The feedback network consists of CFB1 and RFB1, defining the transimpedance gain and bandwidth.

The generated photocurrents are combined and subtracted (due to opposite polarity) before being fed into the TIA stage, where the net differential photocurrent is converted to a voltage and amplified. The TIA stage, illustrated in Figure 3.25, is built around the OPA827 op-amp, with the feedback network comprising CFB1 (0.1 pF) and RFB1 (1 GΩ), which define the transimpedance gain and bandwidth. The power supply pins are low-pass filtered via R9/C13 and R10/C14 to prevent noise from the regulators coupling into the OPA827.

Finally, as noted earlier, a voltage buffer (Figure 3.26) isolates the TIA stage from the load. A low-pass filter precedes this stage (R11 + C15), which has been inserted provisionally in case further filtering is required.

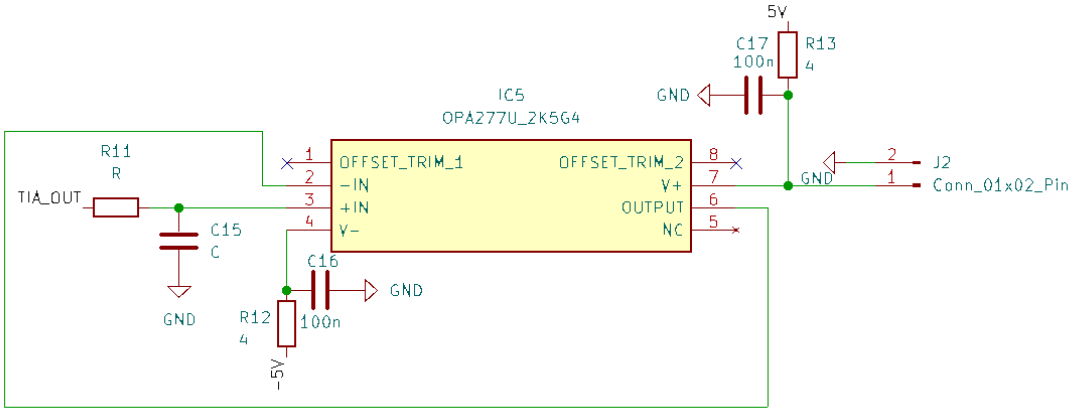

Figure 3.26 - Unity-gain voltage buffer stage based on the OPA277U, isolating the TIA from capacitive loads.

The complete schematic is shown in Figure 3.27.

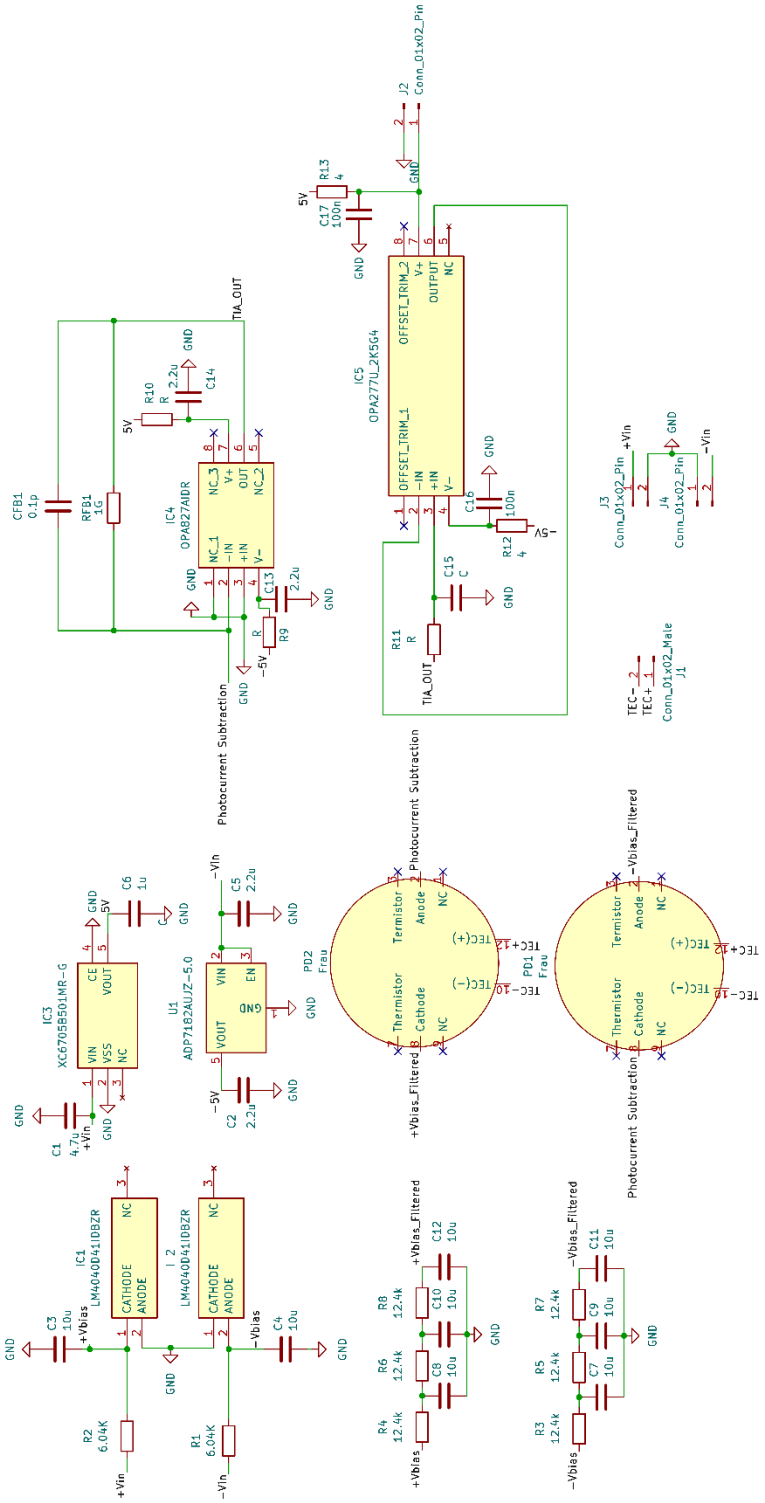

Figure 3.27 - Complete schematic integrating all the functional blocks presented in **Figure 3.23 - Figure 3.26.**

A 9.5 cm × 6 cm printed-circuit-board (PCB) was designed incorporating a guard ring around the high impedance node. This solution offers protection from potential leakage currents. The guard ring's potential is the same as the inverting input of the OPA827, due to the virtual ground principle.

The ring is also routed underneath the feedback components, reducing the effects of stray capacitance. Because the end conductors of the feedback components are at different potentials, they form an electric field which can store energy. This manifests as extra, unwanted capacitance that is minimised via the guard ring technique. Additionally, on the bottom side of the PCB, the ground plane was cut underneath the op-amp locations, to minimise input capacitance between the input pins and ground.

To aid visual clarity, photorealistic renders have been generated by exporting the *KiCad* PCB model and importing it into *Blender*, where appropriate materials and lighting were applied. This produced a clean and accurate visualisation of the placement, orientation and interconnection of components. Figure 3.28 shows 3D renders of the final PCB layout.

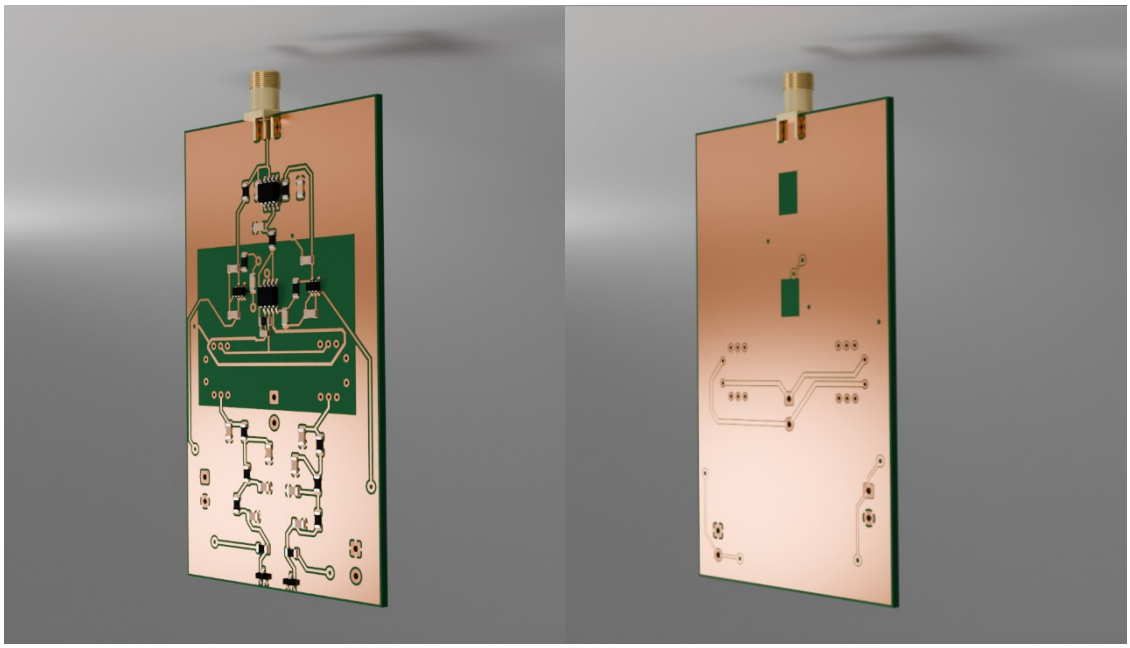

Figure 3.28 - 3D photorealistic renders of final PCB layout, showing both sides of the TIA board.

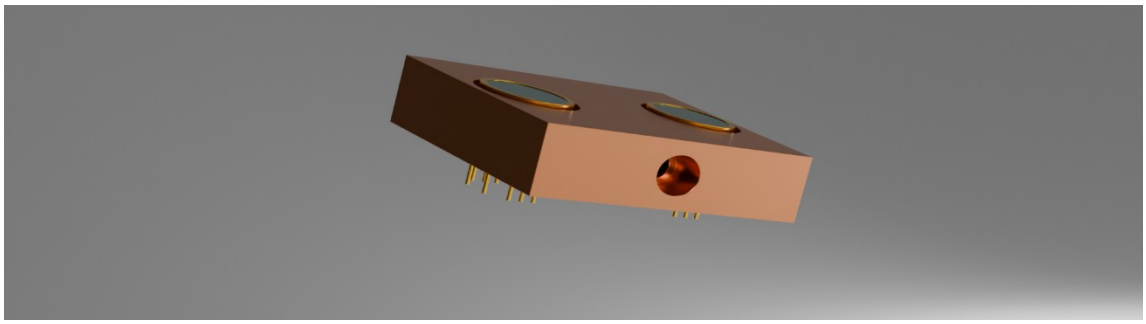

Figure 3.29 - 3D photorealistic render of heatsink copper block & photodiode assembly

When a DC current is applied to the TEC, heat is moved from one side of the module to the other, making one plate hot and the other cold. Some energy, however, is lost as joule heating (I^2R) due to the resistance of the module and it ends up on the hot surface. To efficiently maintain this temperature difference between these two surfaces and achieve better cooling performance, heat must be dumped from the hot side. To this end, a custom heat-removal solution was implemented. A copper block was machined to house the photodiodes so that the bottom of the TO-8 package has maximum contact with the copper block, a high-thermal-conductivity compound was used as a medium. The photodiode leads were insulated from the copper block using sections of plastic insulation. A model showing the photodiodes positioned within the recesses of the copper block is shown in Figure 3.29.The photodiode and heatsink assembly integrated with the PCB is visualised with the aid of a 3D render in Figure 3.30.

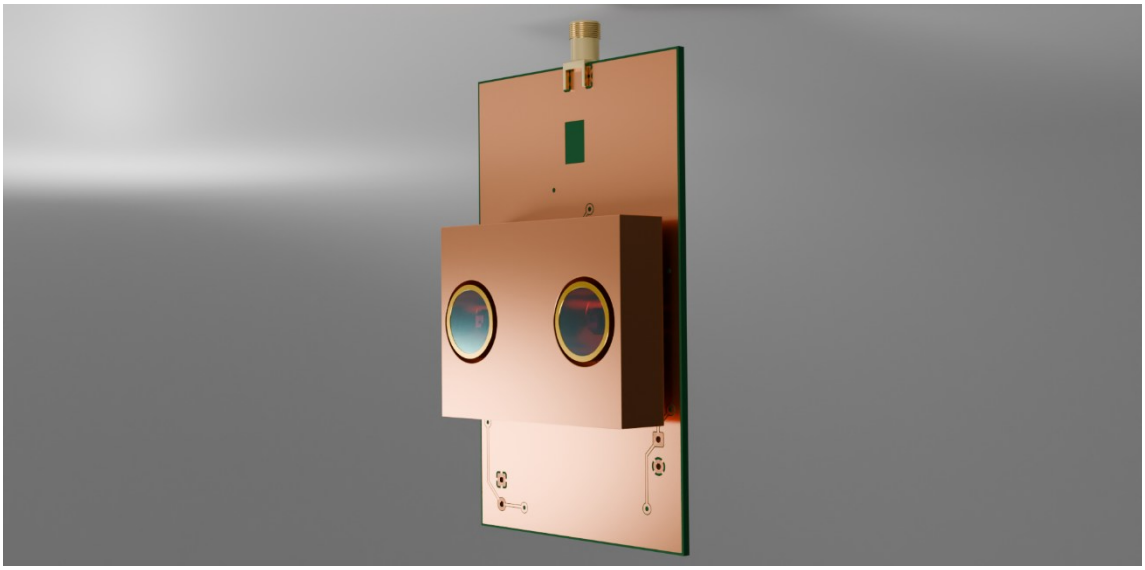

Figure 3.30 - 3D photorealistic render of heatsink and photodiode assembly integrated with PCB.

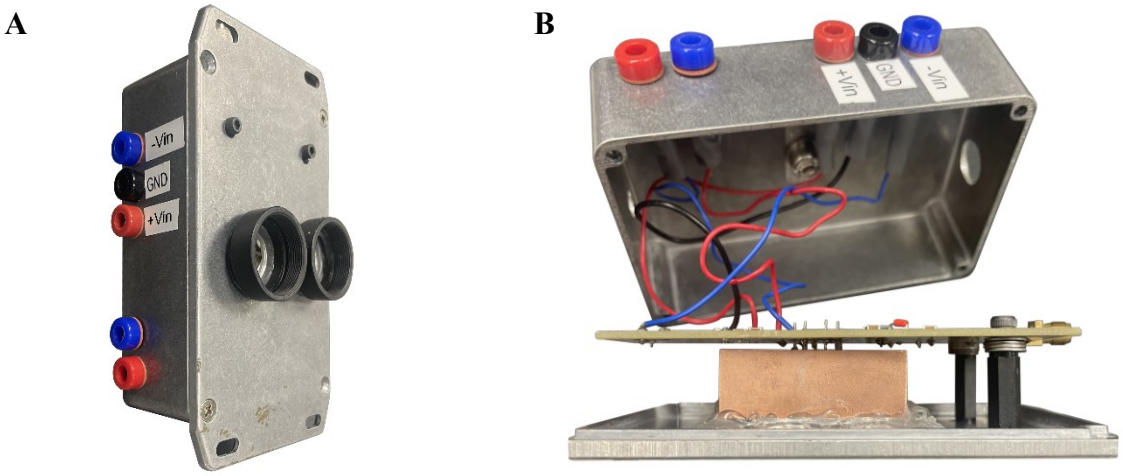

Figure 3.31- The completed ultra–low-noise balanced detector. **A**: Enclosed assembly showing the top blue, black and red banana input providing power to the regulators. The bottom banana inputs are dedicated for the TEC drive | **B**: Opened side view of the detector, showing the internal assembly.

The assembly was packaged in an aluminium case, providing shielding from environmental noise. Plastic standoffs were used to secure the PCB to the case, providing mechanical support whilst electrically isolating the board from the aluminium case which acts as a Faraday cage. Adapters were placed concentrically with the photodiodes, allowing easy integration of SM1-threaded-mounted optics. The completed ultra–low-noise balanced detector is presented in Figure 3.31.

3.2.3 Balanced Detector Characterisation

Following the completion of the balanced detector, the first parameter to be characterised was its AC bandwidth. This is the frequency range in which AC signals are amplified, without attenuation. In the context of pulsed sources, when the repetition rate is low the detector electronics can follow and amplify the individual pulses. As the repetition rate

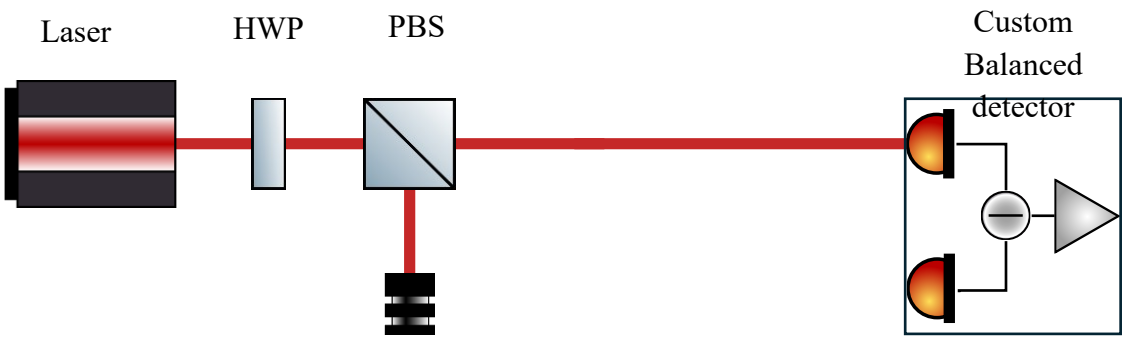

Figure 3.32 - Detector AC bandwidth characterisation setup. A HWP and a PBS were used to attenuate the optical power incident on one of the photodiodes. The laser repetition rate was varied, and the corresponding AC output voltage was recorded.

increases, the pulses arrive too quickly for the detector to follow, so the output consists of an AC signal superimposed on a growing DC offset. The -3 dB point denotes the frequency where the AC transimpedance falls below 70.7 % of its low frequency value. Beyond this point, the detector cannot resolve individual pulses, and the output becomes dominated by DC. This is only a drawback if individual pulse statistics are relevant, in the broader context of this work, pulse-to-pulse variations are not of interest, instead, understanding the detector's bandwidth is the central requirement.

To test this, the *Light Conversion Carbide CB3-40W* laser was used. This source emits 1030 nm, 245 fs pulses and the repetition rate can be varied up to 1 MHz. A simplified schematic of the AC bandwidth characterisation setup is illustrated in Figure 3.32.

The source repetition rate was swept from 100 Hz to 10 kHz, and the voltage-time series traces (100 ms window) were recorded with a *Zurich MFLI* instrument. The AC amplitude of the detector output was extracted from the recorded time traces by correcting the baseline and measuring the base-to-peak voltages of the acquired pulses. The resulting values were averaged and plotted as the AC transimpedance response, normalised to the low-frequency (100Hz) response in dB. The -3 dB point was found to be around 1.7 kHz as illustrated in Figure 3.33, in agreement with the *Tina-TI* simulation.

Building upon the AC bandwidth measurements, the next step was to establish the optimal combination of the thermoelectric cooler (TEC) drive and photodiode reverse bias to ensure low-noise operation.

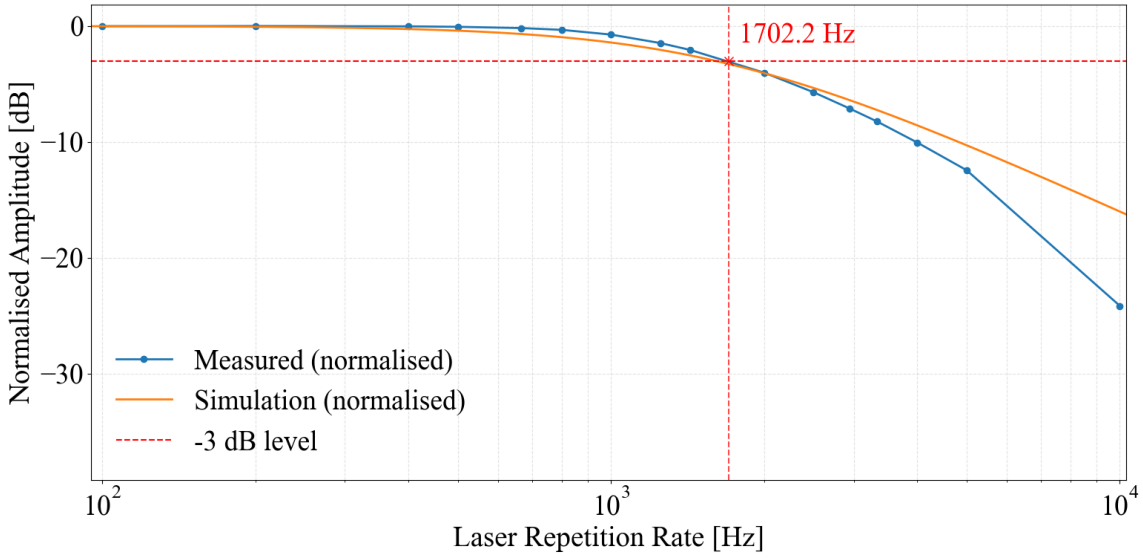

Figure 3.33 - Custom balanced detector AC bandwidth. The blue curve shows the measured response, while the orange trace shows the TINA-TI simulation data. The time-domain voltage was recorded using the MFLI instrument. Time-domain data were processed and normalised to 0 dB so the -3dB bandwidth was identified. Error bars are included but too small to be visible.

With 1 A TEC current, each photodiode can be cooled below $-40\,\text{C}°$, substantially reducing the dark noise contribution compared to room temperature conditions. To systematically evaluate the effect of biasing, the reverse bias potential was varied between 2 V and 5 V in 1 V increments. For each bias setting, the total TEC current was swept from 0 A to 2 A in 0.5 A steps.

The corresponding voltage-noise density spectra were recorded using a *Zurich Instruments* MFLI lock-in amplifier. The time-domain signal was sampled at 7.32 kSa/s, and the FFT was computed automatically by the device's native software.

The intrinsic input voltage noise of the MFLI device was found to be negligible relative to the measured spectra. Figure 3.34 presents the results of the measurement when the reverse bias was set at 2V.

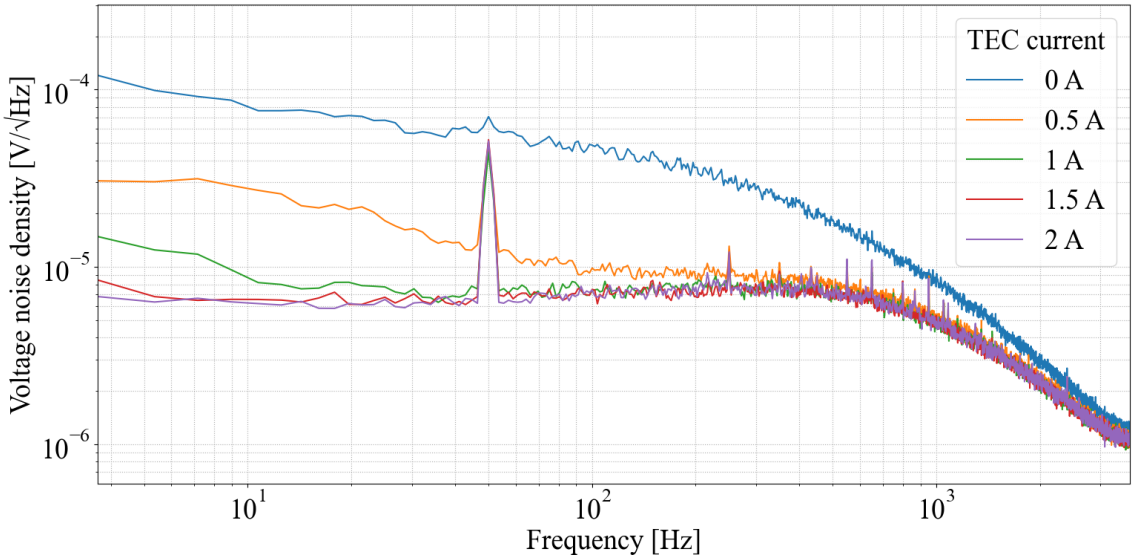

Figure 3.34 - Voltage noise density spectra of the packaged photodiodes at a reverse bias of 2 V, for TEC drive currents swept from 0 A to 2 A in 0.5 A steps. Higher TEC currents progressively reduce the low-frequency noise floor, indicating that cooling suppresses thermal generation-recombination noise in the photodiodes.

The voltage-noise spectra were recorded for all reverse-bias settings, and the mean voltage noise density was computed between 400 – 700 Hz, where the transimpedance gain is approximately flat. The results are summarised in Figure 3.35.From this figure, it can be deduced that in the absence of cooling (TEC current = 0 A), the noise level increases with reverse bias. This is a consequence of the dark current being the dominant contributor in noise. As the depletion region widens, thermal generation within it grows. Increasing the TEC current cools the devices and thermal generation is substantially reduced and so is the dark current. For currents above 1 A, the influence of reverse bias voltage on the total noise contribution is very small, indicating that the "EnC noise" contribution is insignificant.

A reverse bias of 5 V and a TEC drive current of 2 A were chosen. Although this bias level does not reduce the "EnC noise", a higher reverse bias also improves the linearity, speed and the dynamic range of the device by increasing the carrier collection speed.

In this configuration, the resultant noise floor of the amplifier was about 7 $\mu V/\sqrt{Hz}$. Thus, the input referred current noise of the detector is at $7fA/\sqrt{Hz}$ which puts it in a very high-performance bracket.

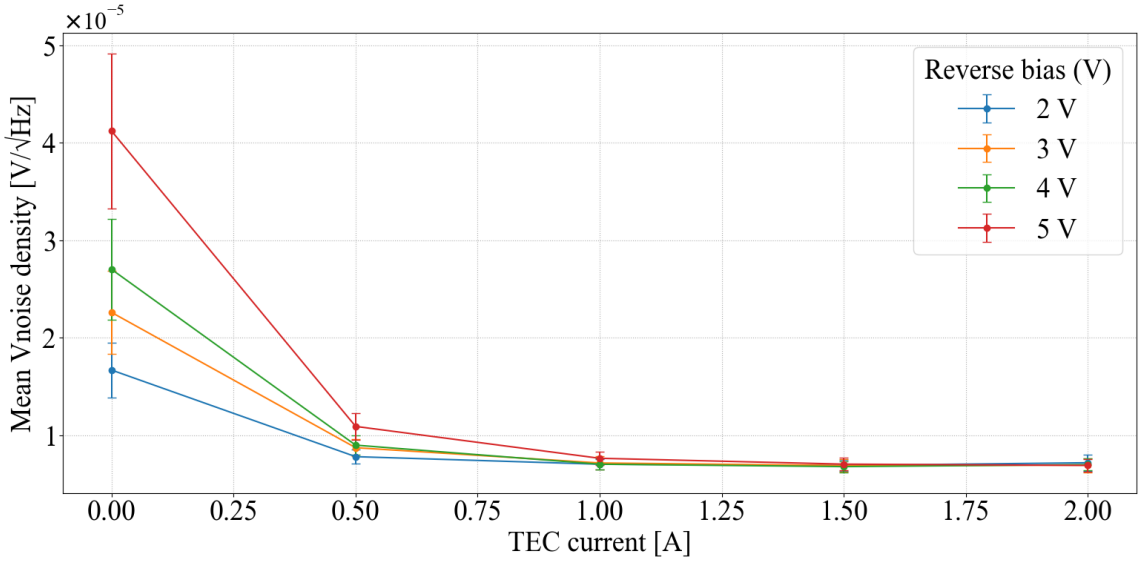

Figure 3.35 - Mean voltage-noise density in the 400–700 Hz band as a function of TEC current. The measurement was repeated for four different reverse bias voltages.

For comparison, one of the market reference tools for low-light measurement, the *Femto's Femtowatt Photoreceiver FWPR*, exhibits similar noise floor and has a useful bandwidth restricted to 20 Hz. In contrast, the custom detector developed here sustains this low-noise density up to 1.7 kHz.

Besides the noise-floor, the metric which is of equal importance is the quantum efficiency of the photodiodes. To quantify this, a setup was constructed where the input power to the photodiodes was varied, and the optical power prior to the neutral density (ND) filter was measured with a power meter before each reading. A schematic of the setup employed to measure the responsivity of the photodiodes is illustrated in Figure 3.36.

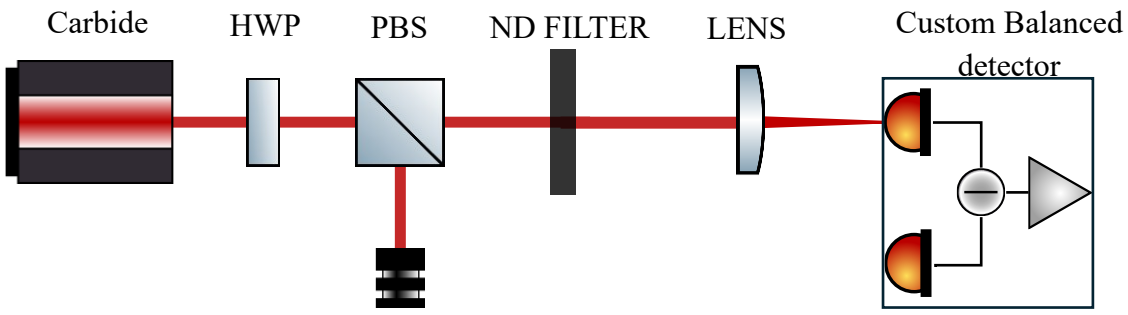

Figure 3.36 - Photodiode responsivity measurement setup. The half-wave plate (HWP) and polarising beam splitter (PBS) provide precise energy control, while a neutral-density (ND) filter enables further attenuation. A 100 mm AR-coated lens focuses the light onto the photodiode while minimising optical losses.

A half-wave plate (HWP) combined with a polarising beam splitter (PBS) enabled precise control of the optical power. The ND filter (NE10) was individually characterised, allowing the calculation of the incident optical power on the photodiodes. A 100 mm AR coated (1000-1060 nm, R<0.1%) lens was used to minimise optical losses. This measurement allowed the characterisation of each photodiode, where the detector output voltage was plotted as a function of optical power, as shown in Figure 3.37. The responsivity of the photodiodes can be extracted from the plots by dividing the gradient by the transimpedance gain of the detector.

To determine the quantum efficiency, the 1 GΩ feedback resistor was replaced with a 1 MΩ one. This was implemented because using a very large resistor would require more ND filters, necessary to achieve the required optical attenuation. Consequently, measurement uncertainty would increase, as that the ND filters would have to be individually characterised. In some cases, this characterisation pushed the power meter to its detection limits, further adding to the overall uncertainty. By operating at a lower transimpedance gain, with a resistor of a low, known tolerance, the characterisation can be performed with more precision, before replacing the feedback resistor to the original value.

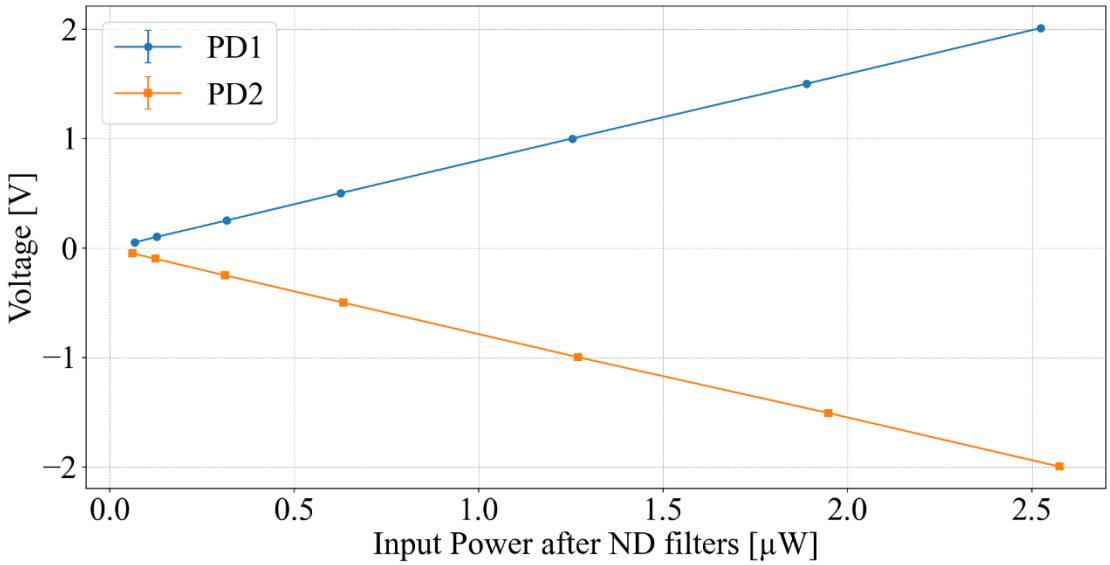

Figure 3.37 - Responsivity of PD1 and PD2. The gradient of these curves provide the product of the responsivity of the photodiode and the transimpedance gain. Dividing by the transimpedance gain allows us to extract the individual photodiode responsivity.

Consequently, this can be used to calculate the quantum efficiency of each photodiode by using Eq. 3.16

$$\eta = R\frac{hc_0}{q\lambda}, \tag{3.16}$$

where η is the quantum efficiency, R is responsivity, h is Planck's constant, c is the speed of light, q is the elementary charge and λ is the optical field wavelength. The quantum efficiency of PD1 and PD2 was found to be 96.3 ± 1.3 % and 94.1 ± 1.3 % respectively where the ± values represent the combined propagated uncertainty at the 1σ level.

The final parameter that will be reported here is the common-mode rejection ratio (CMRR). A key metric in balanced detection as it quantifies how well the two photocurrents are subtracted.

To evaluate it, the laser repetition rate was set to 1 kHz, and the same amount of optical power was illuminated on both photodiodes. The output spectrum was then recorded. Following this, one of the photodiodes was covered and a second spectrum was recorded. The results, shown in Figure 3.38, allow the CMRR to be determined from the dB difference between the two recorded peaks. A CMRR of 40 dB was established.

A higher CMRR could be achieved by choosing photodiodes with tightly matched quantum efficiencies, junction capacitances and dark current. Introducing adjustable bias networks as well as independent temperature control and stabilisation would allow these parameters to be equalised in real time. These steps would further improve balancing and mitigate the possibility of CMRR being a limiting factor in squeezing measurements. Nonetheless, values around 40 dB are already considered competitive compared to devices currently available.

Overall, the detector development and characterisation confirm that the detector is a high-performance device that meets the requirements of quantum optical measurements. The demonstrated sensitivity, low-noise performance and bandwidth provide confidence that it is a suitable device for resolving quantum noise at nanowatt optical powers. In the following chapter, the detector serves as a pivotal tool, integrated into quantum optical experiments to perform ultrafast measurements beyond the shot-noise limit.

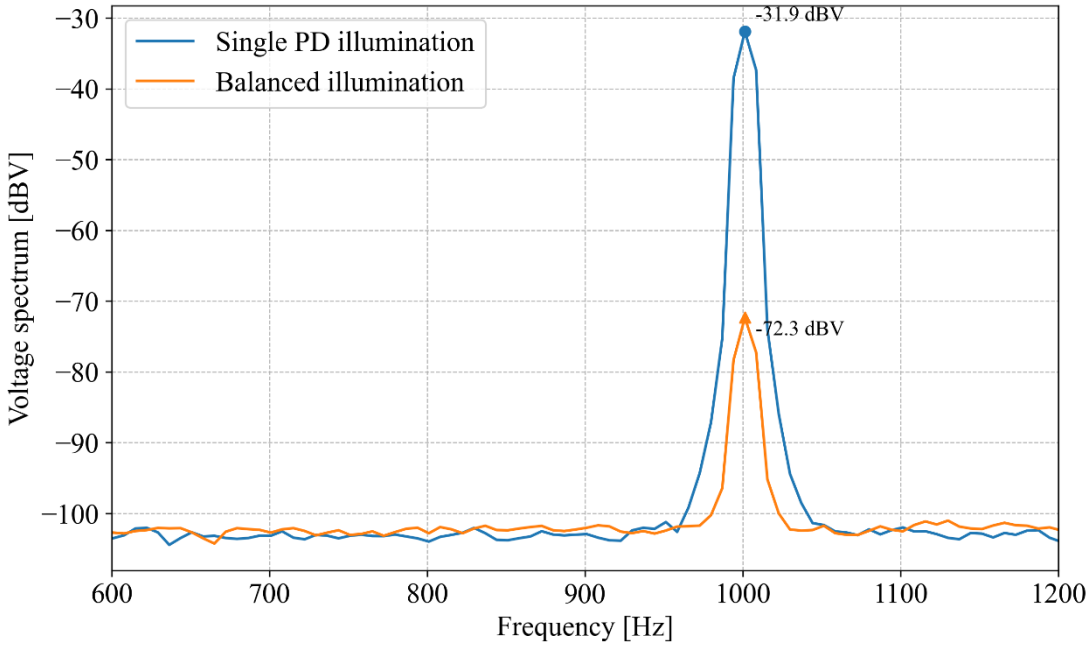

Figure 3.38 - Common-mode-rejection-ratio measurement. The blue peak corresponds to single photodiode illumination, while the orange trace represents the spectrum in the balanced configuration. In the balanced regime, more than 40dB of suppression was observed.

3.2.4 Commercial Balanced Detector

A direct outcome of this project was the expertise I gained in low-noise transimpedance amplifier design and characterisation. Through a collaboration with Bay Photonics, RedWave Labs and CPI, funded by Innovate UK, a high quantum efficiency detector was developed, termed HiQuED, tailored for quantum and photonics research. In this collaboration, I advised the partners on aspects of low-noise design and practical laboratory usability. My role focused on providing technical input so the collaborating teams can translate the performance of the research prototype into a commercial product.

The HiQuED device retained the core features of the laboratory detector, including high-quantum-efficiency photodiodes with three-stage thermoelectric and passive cooling. Its electronics were further developed, enabling software control of the TEC drive currents and individual channel monitoring.

Figure 3.39 - High-quality images of the finalised HiQuED commercial balanced receiver.

HiQuEd serves as a clear example of knowledge transfer from academia to industry where the design methodologies developed in this work contributed to the development of a commercial detector with potential for broader development. Images of the final product is shown in Figure 3.39.

4 Ultrafast Twin-Beams

In shot noise limited detection, there is a square root relationship between the SNR, and the number of photons detected N such that $SNR \propto \sqrt{N}$. Consequently, increasing the optical power enables an improvement of the SNR. In some cases, however, the optical power cannot be increased indefinitely. For instance, in biological samples, higher illumination levels can cause photobleaching, thermal damage or even cell death. In microscopy, where the spatial resolution depends on the tightly focused light, this effect is more prevalent.

In the context of THz-TDS applications, upper limits are dictated by nonlinear noise and back-action. Guedes *et al*. [22] theoretically determined this threshold to be on the order of tens of nJ per pulse, beyond which cascaded nonlinear contributions begin to dominate and contaminate the measurement signal.

In such scenarios, when classical noise-reduction techniques are no longer effective, further enhancement in sensitivity can be achieved using non-classical states of light, such as twin-beams, which possess correlations in their photon-number. By harnessing these photon-number correlations, balanced detection can be performed below the shot-noise limit.

The following sections outline the developments undertaken toward achieving sub-shot-noise measurements in the femtosecond regime. In Section 4.1 a reference is established by achieving shot-noise limited balanced detection at low-light levels, thereby validating the performance of the detector developed in Chapter 3. Section 4.2 focuses on the development of a twin-beam source via spontaneous parametric down-conversion. Finally, Section 4.3 builds on the findings of Section 4.2, where the parametric process is seeded with a coherent field to enhance the intensity and performance.

4.1 Shot-noise Limited Detection

To achieve shot-noise limited detection, the setup in Figure 4.1 was used. The light source was the previously mentioned Carbide laser. The system provides four presets, offering pulse energies of 400 µJ at 100 kHz, 200 µJ at 200 kHz, 80 µJ at 500 kHz, and 40 µJ at 1 MHz, respectively. In this experiment, the laser was operated at 1MHz.

The green dashed boxes outline the energy control stages. They were implemented using variable attenuators, designed for 1030 nm, femtosecond applications. The first stage controls the energy sent to the detector, while the second stage balances the optical power incident on the photodiodes.

This experiment employs the balanced detector described in Chapter 3. The total optical power was varied, and the voltage noise density spectra were recorded at each optical power level. Spectra were recorded using the Zurich MFLI frequency FFT function. The sampling rate was set to 7.32 kS/s, and 4096 samples were recorded for each spectrum.

The mean and standard deviation were computed between 100-800Hz (where the transimpedance gain is flat). Subtracting the electronic (dark) noise spectrum results in a plot of input power versus amplified shot noise, as shown in Figure 4.2.

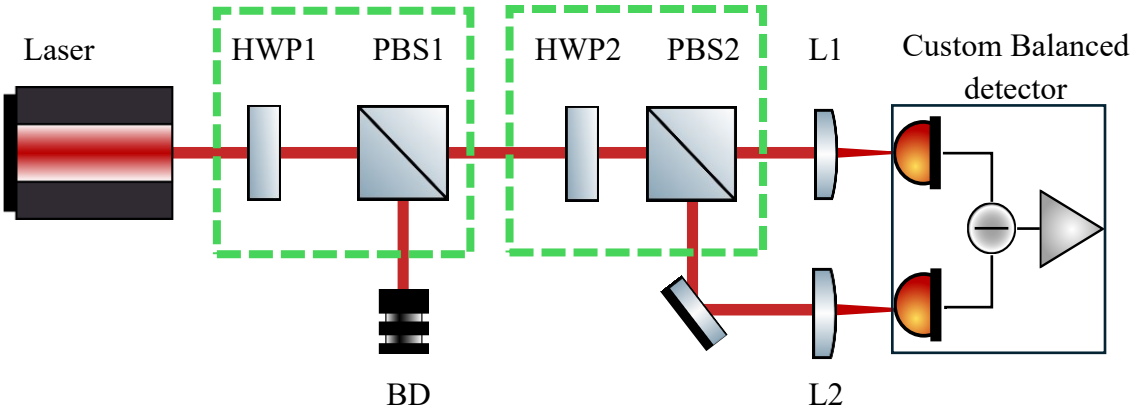

Figure 4.1 - Shot-noise limited detection setup. HWP1 and PBS1 are used to attenuate the total optical power sent to the detector. HWP2 and PBS2 are used to balance the light on both photodiodes.

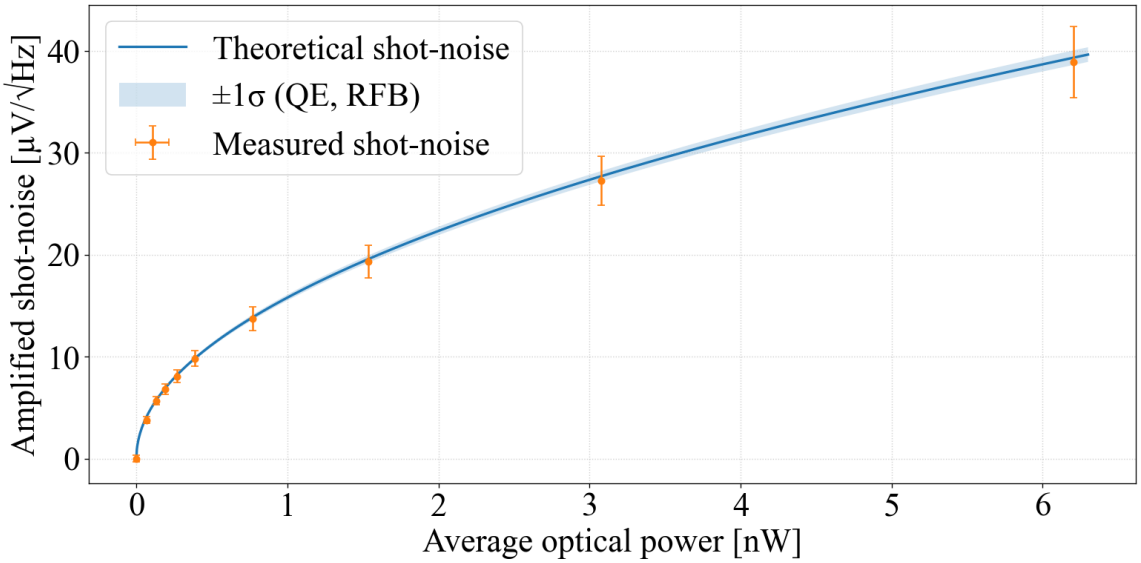

Figure 4.2 - Shot-noise limited detection: measured versus theoretical. The light blue shaded area represents the propagated uncertainty in the theoretical calculation, attributed to quantum efficiency and resistor tolerances. The orange error bars correspond to the standard deviation of the measured amplified shot-noise within the measurement range.

Results from a theoretical model have been included for comparison. The model firstly transforms optical input power into photocurrents. The photodiodes' real quantum efficiencies have been considered, as extracted in Section 3.2.3. As noted in Eq. 3.4, shot noise scales with the square root of the current. In balanced detection, this is the total photocurrent produced by the photodiodes. Thus, the difference signal carries shot noise set by the total photocurrent. Subsequently, the circuit amplifies it to a voltage noise density via the transimpedance gain.

For this comparison, the transimpedance gain has been assumed to be flat since we are operating in the 100-800 Hz range. By sweeping the input power range, the theoretical shot-noise curve was produced.

The light blue area in Figure 4.2, indicates the uncertainty of the prediction which has been obtained by propagating the stated errors. (Photodiodes' QE errors and R_f tolerance). These results confirm that the detector can measure shot noise at sub-nanowatt optical powers, validating its sensitivity and low-noise performance.

4.2 Twin-beam Squeezing via Spontaneous Parametric Down Conversion

Having confirmed shot-noise limited detection, the next aim is to surpass this limit by exploiting quantum correlations in twin-beams. These were generated by spontaneous parametric down conversion (SPDC) in a BBO crystal pumped at 515 nm. This type of crystal offers high-damage threshold, strong nonlinear coefficient and broad phase-matching bandwidth, making it well suited for femtosecond applications [70].

A type-I interaction was chosen because the nonlinear coefficient is higher for this type of interaction compared to type-II, resulting in a higher down-conversion efficiency. Moreover, the down-converted photons have broader spectral bandwidth at the degenerate wavelength of 1030 nm, which is advantageous under femtosecond pumping.

Generating quantum fields at the near infrared (NIR) is advantageous, as high quantum efficiency detectors are readily available. In addition, a broad selection of optical components with high-reflectivity and anti-reflection coatings are commercially available for this spectral region, enabling cost-effective integration of optoelectronic components that minimise photon losses.

Loss in either arm of a twin-beam measurement reduces the measurable photon-number correlations. This is a consequence of the fact that fewer signal-idler pairs are detected. As signal-idler pairs are broken, the contribution of uncorrelated shot-noise becomes more dominant. This behaviour has been studied both theoretically and experimentally by Allevi *et al.* [71] demonstrating that sufficiently high losses will eventually be driven toward the shot-noise limit, thereby losing any quantum-noise suppression.

The main drawback of this configuration is that both down-converted photons share the same polarisation, making spatially separating correlated photons more challenging. An illustration of the simplified experimental setup is shown in Figure 4.3.

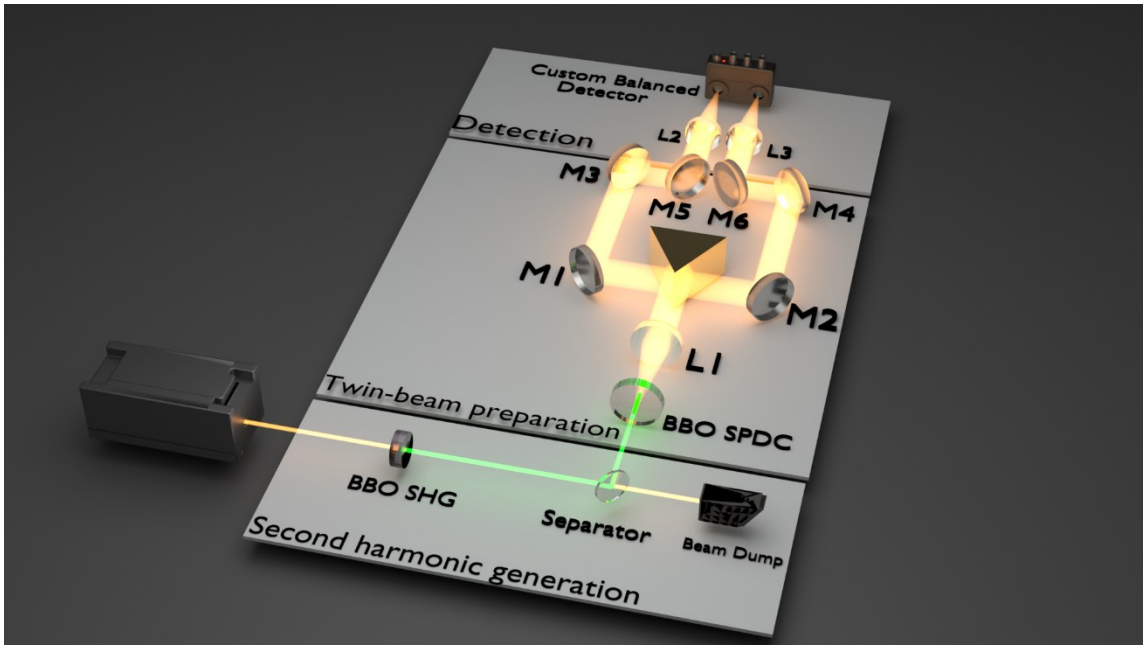

Figure 4.3 - Optical layout of the experimental setup used to generate twin-beams via SPDC. BBO SHG: AR/AR @ 515 & 1030 nm. L=1 mm | BBO SPDC: AR/AR @ 515 & 1030 nm. L=2 mm | L1: AR 75 mm @ 1030 nm plano-convex lens | P1: gold knife-edge prism | M1-M6: HR @ 1030 nm mirrors | L2 & L3: AR 75 mm plano-convex lens |SHG stage, where the 1030 nm fundamental is frequency doubled to 515 nm in a BBO crystal. Twin-beam preparation: The 515nm pulses pump the SPDC crystal, with intensity-correlated photons being split into two beams via P1 | Detection: differential measurement of the intensity-correlated beams.

The Carbide laser output (1030 nm) is frequency-doubled, in a 1 mm BBO crystal via SHG. To characterise and optimise the SHG efficiency, the input (1030 nm) and output (515 nm) powers were measured for different beam sizes. Owing to the high laser intensity and limited literature on damage thresholds in the femtosecond regime, tight focusing caused gradual crystal heating, and eventually surface damage. The optimal focusing condition was found by reducing the fundamental beam waist from 2mm to 1.3 mm (FWHM) using a Galilean telescope.

The 1 mm BBO crystal was then mounted on a translation stage and its position along the fundamental beam propagation direction was adjusted, to maximise the 515 nm output. Moreover, the crystal was mounted on a kinematic stage, allowing precise optimisation of the phase-matching angle. The input and output optical powers were measured with a *Gentec-EO* thermal power meter for increasing input powers. This process was performed

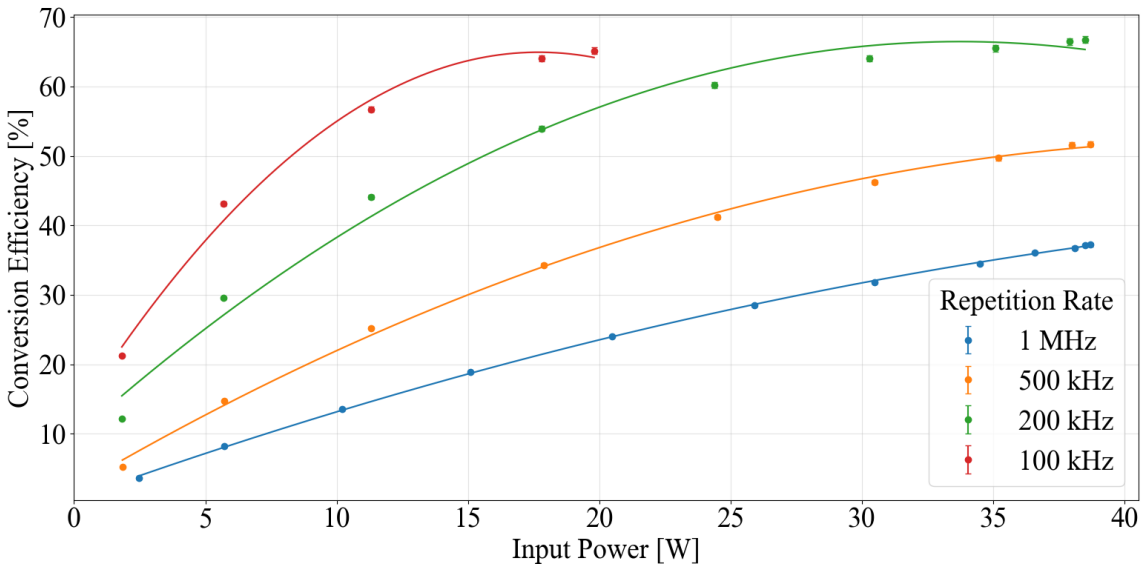

Figure 4.4 - Second-harmonic generation characterisation. Conversion efficiency as a function of input pump power for four different laser presets. 1 MHz: able to deliver up to 40 µJ per pulse | 500MHz: able to deliver up to 80 µJ per pulse | 200kHz: able to deliver up to 200 µJ per pulse | 100kHz: able to deliver up to 400 µJ per pulse.

for the four laser presets, offering different energies per-pulse and the results are shown in Figure 4.4. As expected, higher conversion efficiencies are observed at lower repetition rate presets, where the energy-per-pulse and thus intensity on the SHG crystal is higher.

To spectrally mode-clean the 515 nm output, the beam was routed via a combination of 45° and 0° separators, attenuating any residual fundamental signal by ≈ –136 dB. Such high attenuation is important, as any residual fundamental light present in the 515 nm path could seed the succeeding PDC process in an unwanted manner. Determining the right crystal length for SPDC generation first required understanding the duration of the 515nm pump pulse. This was addressed by performing a single-pass OPA cross correlation measurement.

To this end, the 1030 nm fundamental, was spatially overlapped with the 515 nm pump on a BBO crystal, of 0.5 mm thickness. Subsequently, a retroflector was placed on a delay stage and the 1030 nm beam was scanned through temporal overlap on the crystal. Since the 515 nm pulse drives the OPA process, the 1030 nm experiences maximum optical amplification at exact temporal overlap. Consequently, by scanning the delay, and

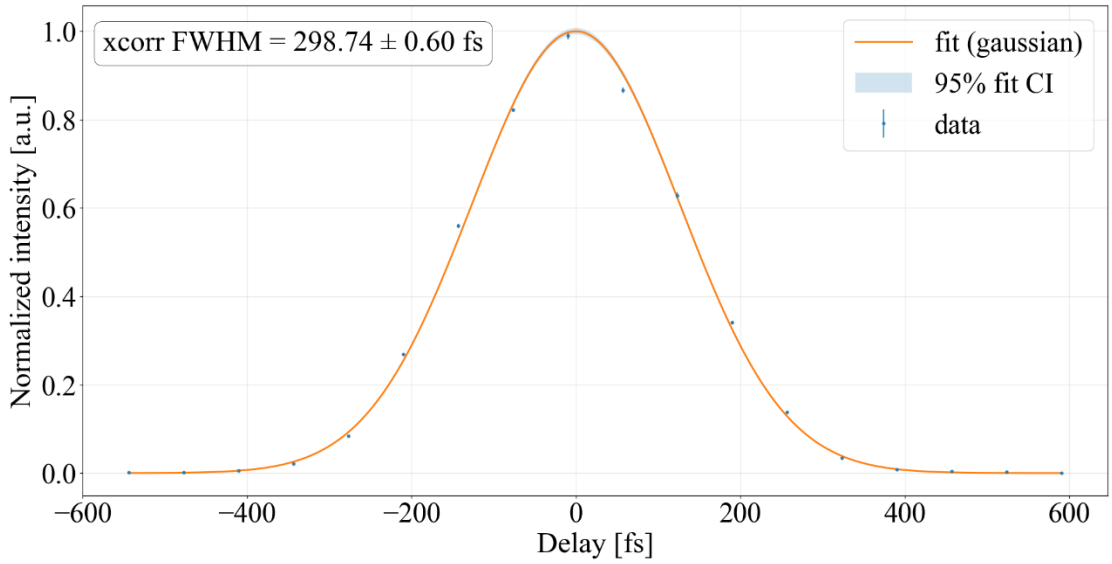

Figure 4.5 - Gaussian cross-correlation obtained via optical parametric amplification between the 1030 nm fundamental and the frequency-doubled 515nm. The Gaussian fit yields a FWHM of ≈299 fs.

calibrating the axis for a retroreflector scan, a cross-correlation profile between the two pulses, was produced.

From Figure 4.5, and by using the known 1030 nm duration of 245 fs, whilst also assuming Gaussian intensity profiles, the 515 nm pulse duration can be inferred from

$$\tau_{515\text{nm}} = \sqrt{\tau_{\text{xcorr}}^2 - \tau_{1030\text{nm}}^2}. \qquad \textbf{4.1}$$

This yields a pulse duration of 171 ∓ 1.1 fs, which closely agrees with the expected value for the SHG of a 245 fs Gaussian pulse in a thin nonlinear crystal

$$\tau_{\text{SHG}} = \frac{\tau_{\text{fundamental}}}{\sqrt{2}} = \frac{245\text{ fs}}{\sqrt{2}} = 173\text{ fs}. \qquad \textbf{4.2}$$

Based on simulations with *Software for Nonlinear Optics (SNLO)* by Dr. Arlee V. Smith [72] , assuming a type-I BBO crystal, the group-velocity mismatch (GVM) between 1030 nm and 515 nm was -95 fs/mm.

This quantifies the temporal walk-off between the interacting waves and corresponds to the difference of their inverse group velocities

$$GVM = \frac{1}{v_{\mathrm{g(515\ nm)}}} - \frac{1}{v_{\mathrm{g(1030\ nm)}}}, \qquad \textbf{4.3}$$

where $v_{\mathrm{g}} = c_0/n_{\mathrm{g}}$ are the group velocities that are obtained via the SNLO software using the Sellmeier dispersion relations of BBO.

From the GVM, the splitting length can be calculated, defined as the propagation distance within the crystal that the interacting pulses separate by one pulse duration

$$L_{overlap} \approx \frac{\tau_{515\,nm}}{|GVM|}. \qquad \textbf{4.4}$$

Using the obtained parameters for $\tau_{515\ \mathrm{nm}}$ and |GVM|, a splitting length of 1.8 mm was calculated. For this reason, both 1 mm and 2 mm crystals were investigated. When the 1 mm crystal is employed, the pump and the down-converted fields remain overlapped, increasing phase-matching bandwidth and thus generating temporally short down-converted fields. An accumulation of slip that reduces temporal overlap is expected with the 2 mm crystal, leading to narrower spectral bandwidth and therefore longer PDC pulses. However, the longer interaction length enhances the overall nonlinear gain and photon-pair generation.

The pump beam was directed to the PDC BBO crystal with the aid of a 45° dichroic separator, further removing any residual fundamental light. Immediately after the exit of the SPDC crystal, an antireflection coated lens (L1, f=75 mm) was placed at a distance equal to its focal length. Thus, a Fourier plane was formed at one focal length on the other side of the lens, where the spatial distribution of the down-converted photons directly corresponds to the angular spectrum of the SPDC emission.

In practice, this means that each spatial position maps to a specific propagation direction from the crystal, with diametrically opposite points representing momentum correlated photon pairs, as mentioned in Section 2.4.2. Therefore, a knife-edge prism was placed in the Fourier plane where the SPDC emission was split into two parts. By mounting the prism on a Y-Z translation stage enabled precise control of the splitting ratio and the splitting depth (alignment of the prism edge relative to the Fourier plane). It is important to note that the effectiveness of spatial selection, or in this case spatial division, is directly dependent on the spatial mode structure of the SPDC emission.

Correlations in the far field can be pictured as twin speckles on either side of the emission cone. Bright spots, otherwise known as coherence areas, are caused by the finite pump waist and crystal length. Since the crystal length has been determined, it is important to engineer the pump so that the probability of correlations being efficiently split and directed onto the photodiodes is enhanced.

A larger pump waist corresponds to a smaller coherence area in the far field, meaning that the far-field correlation spots are small and thus many speckles (or spatial modes) are present. In this regime, the chance of the prism dividing an individual mode is small and thus the chance of correlations being preserved post-splitting is higher. Conversely, a tighter pump focus increases the coherence area. Here, the number of spatial modes is reduced with more photons occupying a single spatial mode. In this case, it is more likely for the knife-edge prism to cut directly through a coherence area and thereby break correlations [73].

At sufficiently high pump intensities (high gain) the spatial distribution of the SPDC emission no longer reflects the entire pump spatial profile. Instead, the nonlinear interaction is dominated by the central, high-intensity portion of the Gaussian beam, with the side wings contributing marginally. Therefore, the effective pump waist is narrower than the physical beam waist, affecting the spatial mode structure as noted in the previous paragraph [74].

Accordingly, the pump beam was loosely focused with a 1m focal length plano convex lens so that the beam diameter was ≈ 650 μm ($1/e^2$) at the position of the crystal. This was the largest practical value that ensured the focused twin-beams remained sufficiently

smaller than the 750 μm photodiode active areas. The phase matching of the BBO crystal was tuned slightly away from collinearity so that the cone emission angle was approximately 2°. Increasing the angular separation enabled easier 50:50 splitting of the down-converted light. Figure 4.6 shows the SPDC emission at the far field recorded with an *Andor Zyla 5.5s CMOS* camera. The cone emission angle was obtained by converting the pixel displacement to angular coordinates using the imaging geometry of the setup (f = 75 mm, pixel size = 6.5 μm).

As shown in Figure 4.3 upon splitting, each arm was directed onto the focusing lens (L2=L3, F=75 mm) via three high-reflectivity, broadband ultrafast mirrors. The focusing lenses were also antireflection coated (R<0.3%) with a broadband coating, minimising losses.

To ensure a direct comparison, the measurements were carried out under identical conditions to those used for establishing shot-noise-limited detection, with the only difference being the substitution of the coherent light source with the twin-beam SPDC output. The first set of measurements was performed using an AR-coated 2 mm BBO crystal.

The Carbide laser was operated at 1MHz to minimise the energy of the 515 nm pulses whilst keeping the average SPDC power high. This condition maximises the number of

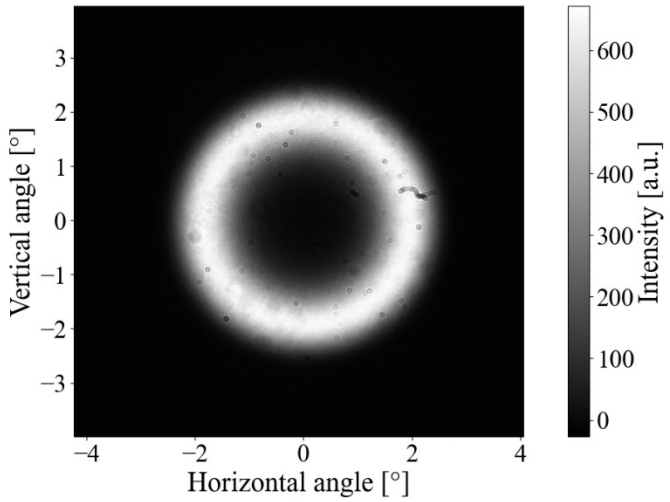

Figure 4.6 - Transverse profile of spontaneous parametric down-conversion (SPDC) cone, captured at the Fourier plane of L1.

spatial modes, as lower pulse energy corresponds to a reduced peak intensity in the nonlinear crystal and therefore smaller parametric gain. Consequently, gain narrowing of the PDC near-field profile is mitigated whilst preserving the total PDC power, due to the higher repetition rate. Under these conditions, we are placed in the best possible position to perform measurements below the shot-noise-limit.

Twin-beam squeezing is quantified by the noise reduction factor (NRF) [75]

$$NRF = \frac{\Delta^2(N_s - N_i)}{N_s + N_i}. \qquad \textbf{4.5}$$

Where $\Delta^2(N_s - N_i)$ is the variance of the photon-number difference between the signal and the idler pulses and $N_s + N_i$ is the shot-noise reference. A NRF below 0 dB indicates that the photon-number difference variance falls below the shot-noise limit, which is the signature of twin-beam squeezing. Consequently, a more negative NRF corresponds to stronger squeezing. Experimentally, we do not evaluate the number of photons on each individual beam. However, the NRF can be computed as the logarithmic power ratio of the difference-photocurrent noise powers measured for the twin-beams and the coherent benchmark.

Figure 4.7 presents the measured voltage noise powers for both the coherent and SPDC data. The data points correspond the photocurrent noise powers at different optical power levels, scaled by the transimpedance amplifier gain. The NRF at different power levels was quantified by taking the logarithmic ratio of the coherent and SPDC noise powers, the results are presented in Figure 4.8.

More than 5 dB of twin-beam squeezing has been observed up to optical levels of 6 nW. A highly promising result.

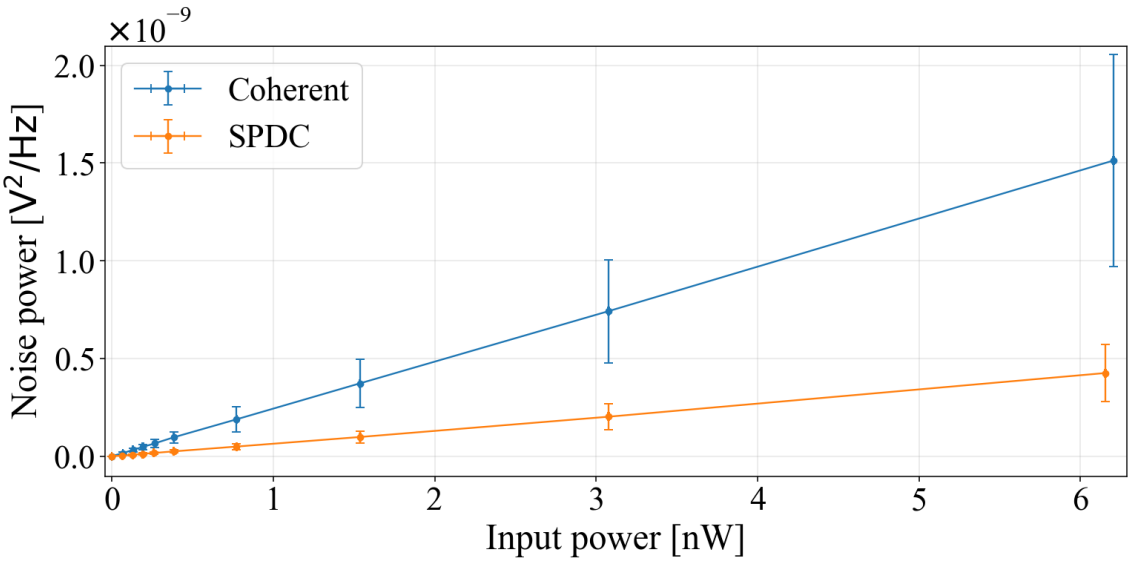

Figure 4.7 - Power spectral density (PSD) of the differential signal as a function of optical power for coherent (blue) and twin-beams (orange). The mean PSD values are computed over a 200 Hz analysis bandwidth, where the electronic noise has been subtracted. The error bars represent one standard deviation. The SPDC noise is consistently lower than the shot-noise limit, demonstrating sub-shot noise behaviour.

It can although be seen in Figure 4.8 that the NRF is slowly diminishing. This can be attributed to the increase in pump power, and therefore intensity, which was required to generate a higher flux of down-converted photons.

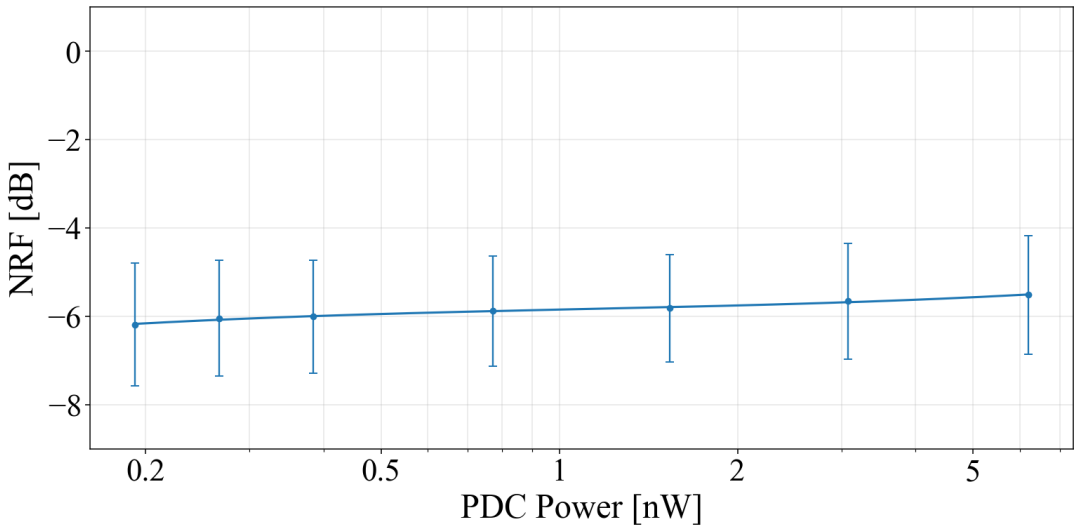

Figure 4.8 - Noise reduction factor (NRF) of twin-beams generated by pumping (515 nm) a 2 mm BBO crystal at a repetition rate of 1MHz. The solid line is drawn to guide the eye, and the error bars represent the propagated 1σ uncertainty.

As described earlier, higher intensities are expected to reduce the number of spatial modes, increase coherence areas and thus reduce the robustness of the correlations. To further examine this effect, the laser's tunability was exploited. By switching between the 1 MHz, 500 kHz, 200 kHz and 100 kHz presets, the pump-intensity and hence the number of down-converted photons per pulse was varied while keeping the average photon flux below the electronic saturation threshold. From these measurements, the NRF as a function of down-converted photons per pulse was determined, Figure 4.9

The NRF worsens by more than 4 dB over the measurement range. This result confirms the pump-dependent degradation already seen in Figure 4.8. More than 6 dB of squeezing is observed at the lowest point, where a pump energy of 170 nJ per pulse is required.

On the other hand, at the highest photon-flux point, 23 µJ per pulse of pump power was needed. This is more than two orders of magnitude increase in pump energy, and directly explains the loss of squeezing, in line with earlier studies of bright squeezed vacuum, where NRF increases with parametric gain [76].

Subsequently, the BBO crystal was replaced by the 1 mm crystal, and the full experimental and analysis procedure was repeated. The results are presented in Figure

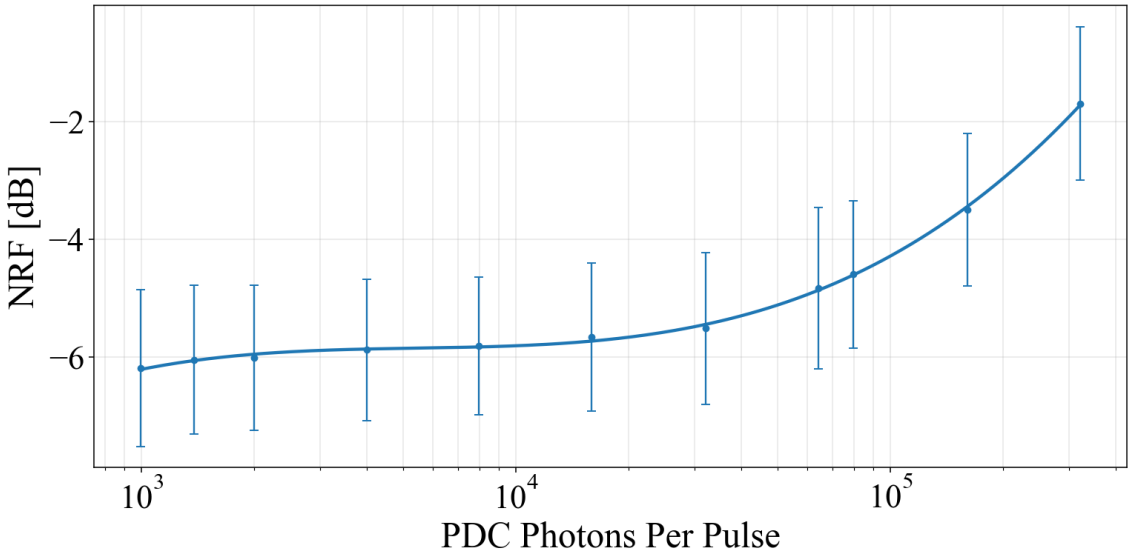

Figure 4.9 - NRF of twin-beams generated with a 2 mm BBO crystal at different repetition rates. Here the NRF is plotted against the number of photons per pulse, showing how the NRF degrades with pump intensity. The solid line serves as a visual guide

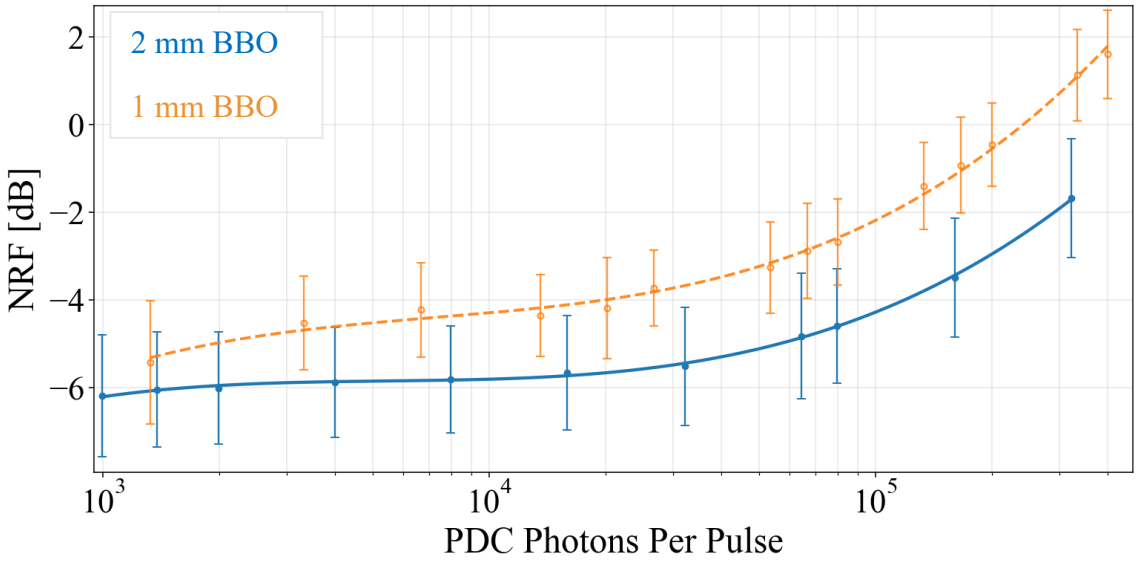

Figure 4.10 – Comparison of the NRF of twin-beams as a function of the down-converted photons per pulse for 1 mm (orange) and 2 mm (blue) BBO crystals. Solid and dotted lines are guides to the eye

4.10, where the NRF values obtained for both crystals are shown. It is important to note that the measurements were performed on different days, so alignment may differ.

The NRF, was observed to be higher when using the 1mm crystal compared to the 2 mm crystal (closer to the shot-noise limit), even at low down-converted photons numbers per pulse. This arises from the trade-off between the interaction length and the pump intensity. To generate the same down-converted photon number, the shorter crystal needs to be pumped with considerably higher energy and therefore the crystal could be driven at higher parametric gain.

The expected number of down-converted photons per pulse can be approximated using [76]

$$N_{\mathrm{SPDC}} = M \sinh^2\left(k\sqrt{N_{\mathrm{pump}}}\right), \qquad \textbf{4.6}$$

where k is a constant encapsulating the crystal nonlinearity, pump focusing and the interaction length. M is the number of spatiotemporal mode pairs, which is dependent on the pump intensity and phase-matching conditions [77]. Determining this number requires numerical integration of the analytic expressions which describe the PDC gain function

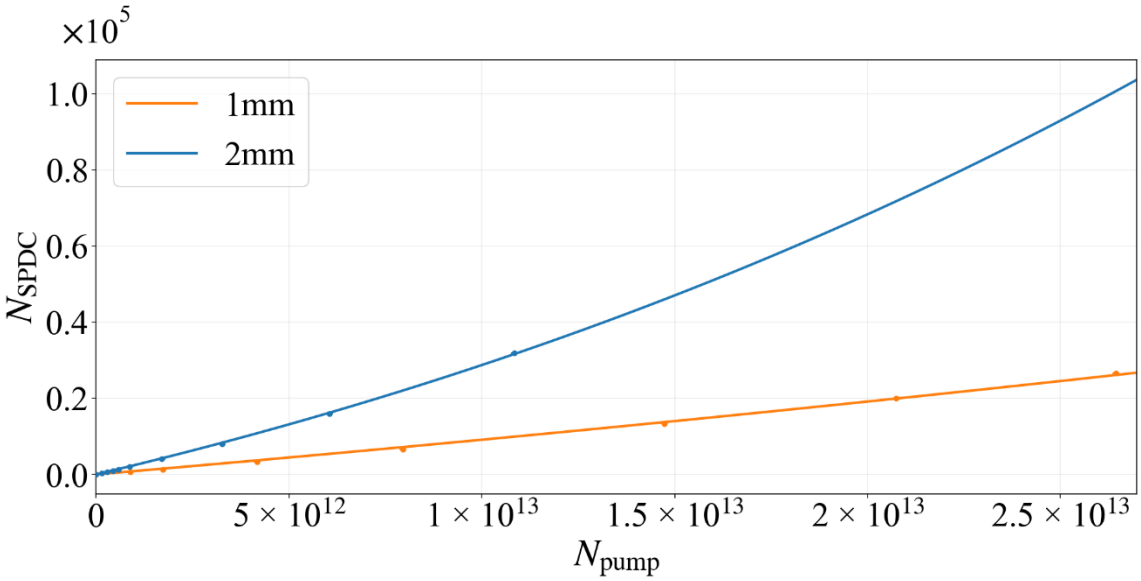

Figure 4.11 - Down-converted photons per pulse as a function of pump photons per pulse for 1 mm (orange) and 2 mm (blue) BBO crystals.

and is therefore, beyond the scope of this work. As illustrated in Figure 4.11, generating the same number of down-converted photons with the 1mm crystal, requires significantly more pump intensity possibly enlarging the coherence areas and losing correlations.

It is well established that the robustness of photon-number correlations, quantified by the NRF depend on both the number of modes and the overall detection efficiency [71]. This has also been observed in this work where the NRF approached or even surpassed the shot-noise limit at higher parametric gains.

Precise determination of the overall detection efficiency is non-trivial due to its broad spectral bandwidth which likely contributes to correlation loss. Figure 4.12 displays the measured spectrum of the SPDC radiation generated in a 1 mm BBO.

The spectrum was acquired by re-imaging the near field of the SPDC emission onto the entrance slit of a Czerny-Turner spectrograph with a spectral resolution of 0.13 nm. An ATLAS SWIR camera, sensitive in the 900-1700 nm range, was mounted on a translation stage scanned along the dispersion direction. This was implemented because the camera sensor was not large enough to capture the entire dispersed medium in one shot. Consequently, a total of five images had to be taken at different stage positions to

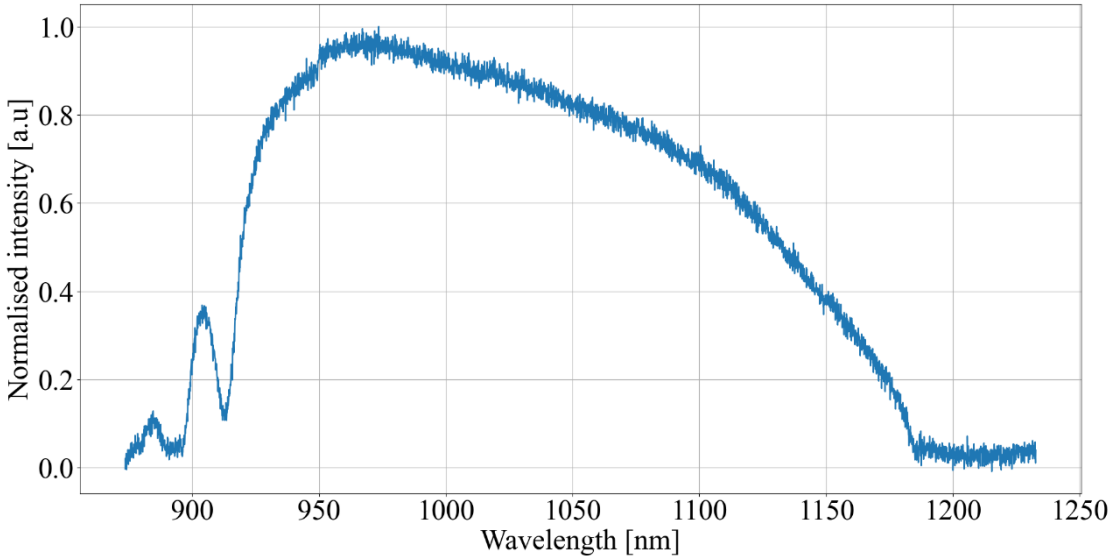

Figure 4.12 - Measured SPDC spectrum from a 1 mm BBO crystal pumped with 515 nm, 171 fs pulses.

reconstruct the full spectrum. To calibrate these images narrowband spectral filters with known central wavelengths were employed.

The observed asymmetry in Figure 4.12 arises because the spectrometer dispersion scale is linear in wavelength (λ) but not in energy (or frequency). This can be explained by considering the energy per photon

$$E = h\nu = \frac{hc_0}{\lambda}, \tag{4.7}$$

where h is Planck's constant, ν is frequency and c_0 is the speed of light. Differentiating Eq. 4.7 with respect to λ we obtain

$$\mathrm{d}\nu = -\frac{c_0}{\lambda^2}\mathrm{d}\lambda, \tag{4.8}$$

where it can be deduced that for shorter wavelengths, a given wavelength interval, $d\lambda$, corresponds to a greater frequency change, since it depends on the square of the wavelength.

Hence, plotting SPDC intensity as a function of wavelength, results in an asymmetric spectrum, even if physically the photons per unit frequency is symmetric and around the degenerate frequency, satisfying the phase-matching condition.

To correct this, the Jacobian factor [78] is applied

$$|\mathrm{d}\lambda/\mathrm{d}\omega| = \frac{2\pi c_0}{\omega^2}, \qquad \textbf{4.9}$$

converting the spectrum from wavelength to frequency space and thereby restoring symmetry and affirming energy conservation across the spectral range, as shown in Figure 4.13.

Despite the use of broadband antireflection and high-reflectivity coatings used in this experiment, the entire spectrum of the SPDC radiation may not be covered, resulting in spectral-dependent losses. Additionally, the photodetector performance is even a bigger concern. InGaAs photodiodes can be expected to behave poorly in the 900-950 nm range. Therefore, it is plausible that a high portion of photons in this spectral region are not detected therefore leading to broken correlations and reduced NRFs.

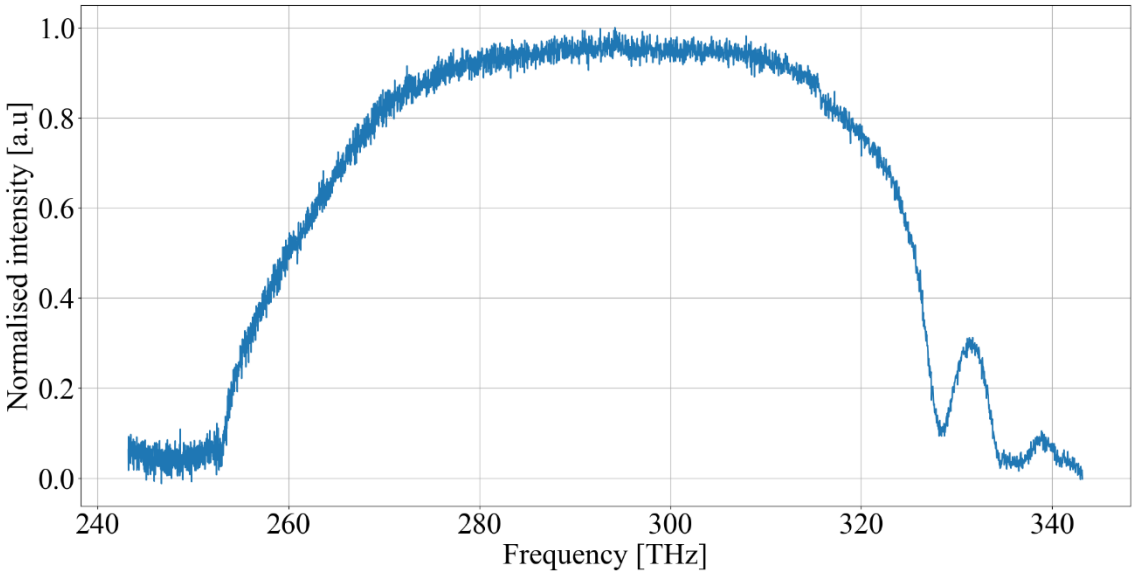

Figure 4.13 – Spectrum acquired **Figure 4.12**, now converted to frequency space after applying Jacobian factor. The correction has restored the spectral symmetry about the degenerate frequency.

4.3 Twin-beam Squeezing via Stimulated Parametric Down Conversion

Although spontaneous parametric down-conversion allowed us to develop a twin-beam source and observe squeezing, the NRF was found to deteriorate with increasing pump energy. In contrast, studies employing twin-beams seeded by faint coherent fields have shown that the quantum-noise reduction improves with increasing OPA gain [62], where the injected coherent field defines a single spatiotemporal mode.

The main objective of the work reported in this thesis was to integrate the twin-beam source in a THz-TDS setup to exploit the NRF and perform quantum-enhanced THz-TDS. The THZ-TDS setup requires the Carbide Laser to operate at 100 kHz to achieve adequate THz radiation amplitudes, which constrained the SPDC pumping to high energies. Therefore, utilising the strong correlations reported in the previous section in the context of THz-TDS is not a viable option. Furthermore, the size (~5 mm) of the non-Gaussian spatial mode of the SPDC radiation and the extremely low photon-flux posed additional challenges for efficient integration into the THz-TDS setup. Furthermore, the low probe power limits the impact of the study, since one of the key objectives is to enhance the sensitivity of THz-TDS at probe-power levels comparable to standard approaches.

Collectively, these limitations motivated the investigation of an alternative approach to assess whether improved NRF could be achieved under the operating constraints of THz-TDS. Specifically, stimulated parametric down conversion. In this configuration, the optical parametric amplifier is seeded with a weak coherent field.

The experimental geometry for seeded twin-beam generation is shown in Figure 4.14. A 2 mm β-Barium-borate crystal is orientated for type-1 phase matching. The green 515 nm pump is directed onto the crystal with a waist diameter of ~ 1 mm at $1/e^2$ intensity level. Simultaneously, the 1030 nm fundamental coherent field is injected in the same region in space, focused more tightly to a waist of $\sim 250\ \mu m$ $(1/e^2)$.

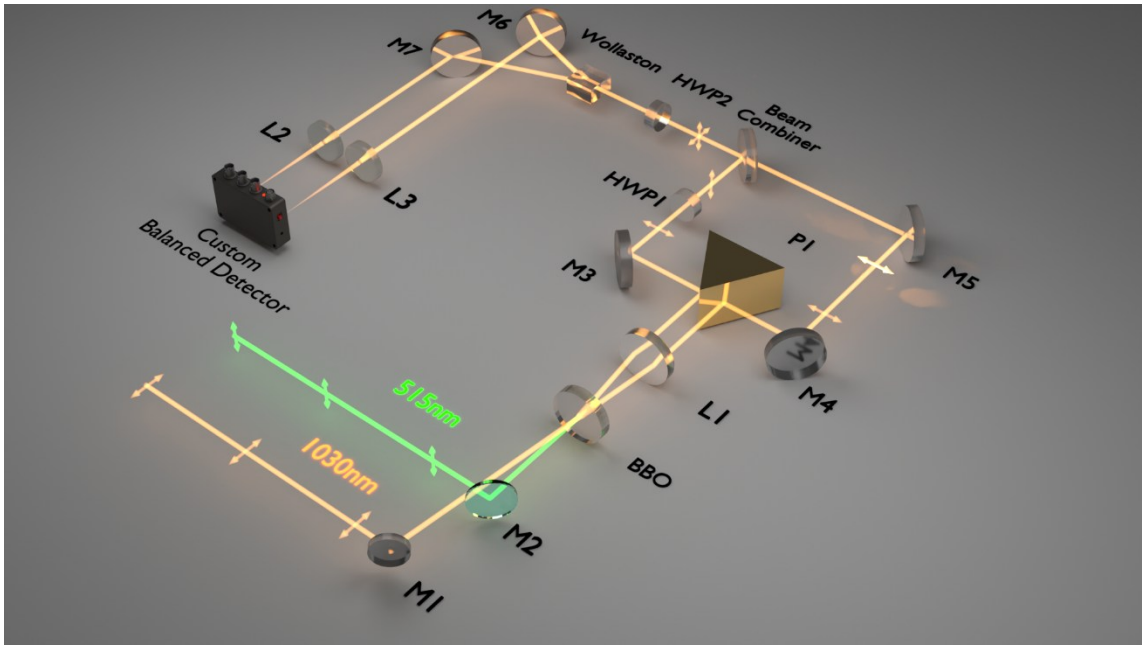

Figure 4.14 - Optical layout of the experimental setup used to generate twin-beams via seeded parametric down-conversion. M1, M3-M7: HR @ 1030 nm mirrors | M2: HR @ 515 nm mirror | BBO: AR/AR @ 515 & 1030 nm. L = 2 mm | L1: AR 75 mm @ 1030 nm plano-convex lens | P1: gold knife-edge prism | beam combiner: AR (p-pol) and HR (s-pol) | HWP: AR halfwave plates | Wollaston: AR @ 1030 nm | L1 & L2: AR 75 mm plano-convex lens. A horizontally polarised 1030 nm seed is injected at an angle 2° relative to the vertically polarised 515nm pump. The signal and idler beams are amplified within the nonlinear crystal and subsequently separated by P1. The first HWP rotates the polarisation of one of the beams allowing the spatial combination of both beams via the beam combiner. A second HWP rotates the orthogonal signal and idler, so they are not aligned with the principal axes of the Wollaston, enabling mixing of the state. Finally, the twin-beams are then separated by the Wollaston prism and directed to the balanced detector.

Temporal overlap between the pump and the seed fields was established by inserting a retroreflective delay line into the 1030 nm path. The BBO crystal was then tuned to satisfy the phase-matching condition for SFG between 1030 nm and 515 nm, producing 343 nm light as shown in Figure 4.15.

Once spatiotemporal overlap was achieved, attention was directed back to the experimental setup. The 515 nm pump polarisation was parallel with the crystal's optical axis, oriented normal to the optical table.

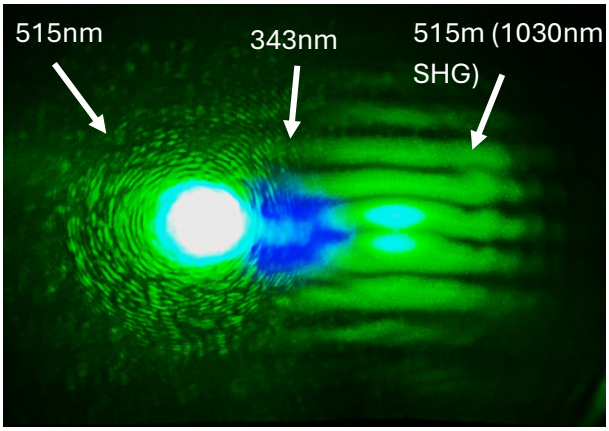

Figure 4.15 - Sum frequency generation between 1030 nm and 515 nm, confirming spatiotemporal overlap between the two pulse trains. A white card placed approximately 40 cm from the BBO crystal allowed the beams to diverge and was photographed with a camera. Three spots are visible: the 515 nm pump (left), the 343 nm SFG output confirming phase-matching (centre), and a residual 515 nm second harmonic of the 1030 nm seed (right).

With the seed beam injected cross-polarised to the pump, twin-beams were generated of horizontal polarisation. One of the beams passes through a half-wave plate which rotates its polarisation to vertical. This enables the spatial combination of the twin-beams into a single spatial mode, while maintaining orthogonal polarisation states.

A second half-wave plate was positioned before the Wollaston prism at the detection stage. By adjusting this, the alignment of the beams to the polarisation axes of the Wolllaston can be maintained, so that they are separated, or their polarisations can be deliberately rotated so that the NRF can be examined in the “separated” or “mixed” configuration.

The OPA was seeded by directing the fundamental field into the BBO crystal at an incidence angle of ~2°, matching the emission cone of SPDC reported in Section 4.2 and ensuring efficient amplification of the seed (signal) and generation of the idler. Figure 4.16A shows the seeded type-I OPA output at the far-field, where the SPDC ring is observed with the twin beams appearing as two diametrically opposed bright spots. The seed without the pump is shown on the right. It is important to note that the left image was obtained under conditions of strong pumping and weak seeding, enabling the observation of both the SPDC ring and the twin-beams without saturating the detector. Under the actual measurement conditions (discussed later in this section), the twin beams are significantly brighter relative to the SPDC ring. Like in the previous section, all

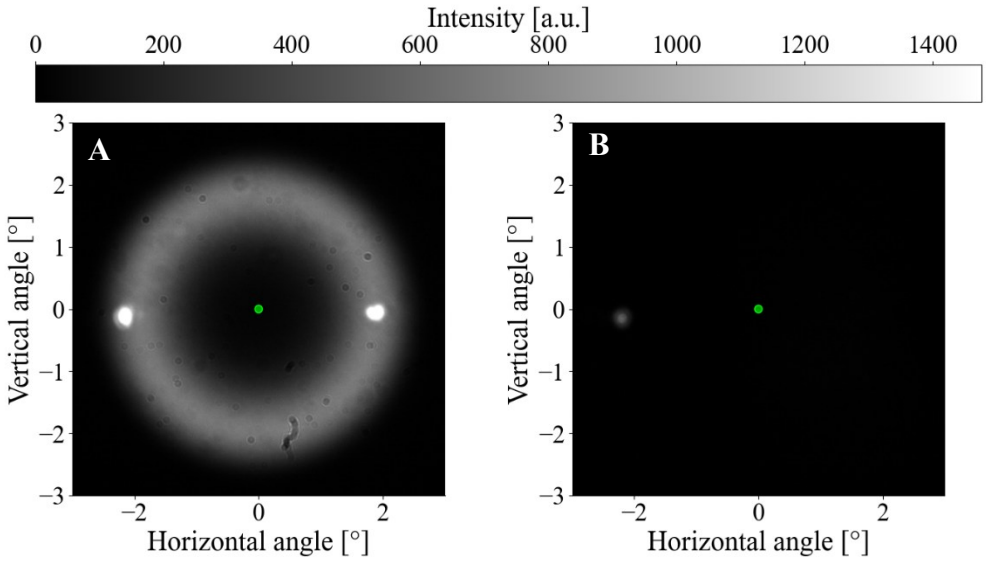

Figure 4.16 - Observation of twin beams in a seeded type-I OPA at the far field. **A**: Emission showing SPDC cone and diametrically opposed amplified signal and idler beams | **B**: Faint coherent seed recorded without pumping. The green circle indicates the position of where the pump would appear if it was not dumped (diameter not to scale).

transmissive and reflective optics were coated with appropriate high-reflectivity and anti-reflection coatings, respectively, to preserve the integrity of the quantum correlations. The measured spectra of the signal and idler beams are shown in Figure 4.17, overlaid with their Gaussian fits. Their FWHM bandwidths were determined to be 12 nm for the signal and 14 nm for the idler.

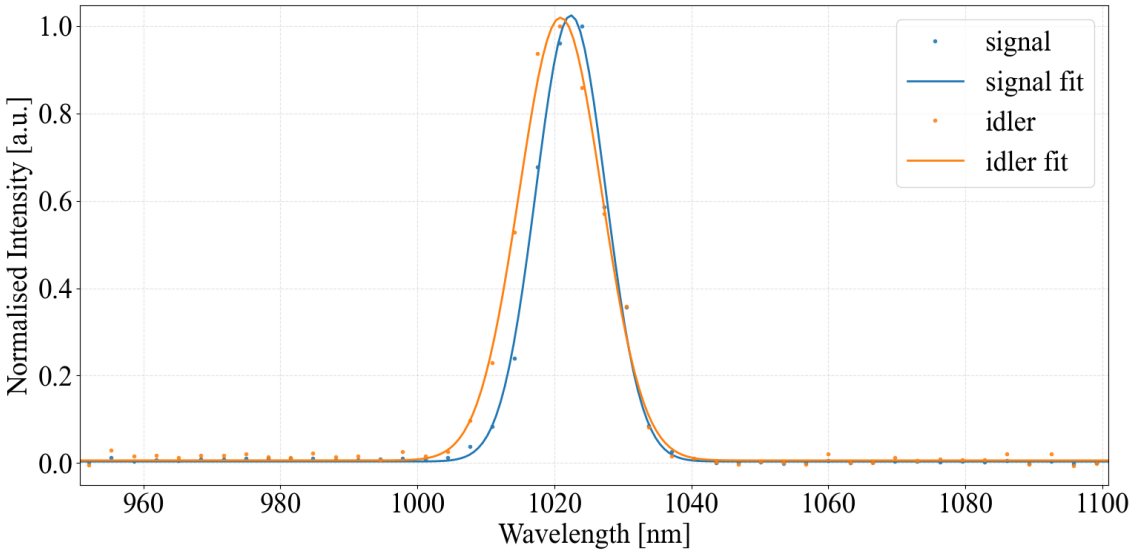

Figure 4.17 - Signal and idler spectra captured with an OceanOptics NIRQUEST spectrometer, with Gaussian fits overlaid.

Two advantages arise from the reduced bandwidths. Firstly, the spectral coverage in which the optics require specialised coatings is narrower, which reduces both the cost and the complexity in sourcing the components. Secondly, the issue that was highlighted in Section 4.2 where the broad SPDC spectra coupled with the limited spectral responsivity range of InGaAs photodiodes led to loss of spectral correlations is avoided.

In coherently seeded OPA, the difference between the signal and idler at the output depends on the parametric gain. For a phase-insensitive non-degenerate OPA, the mean output intensities are governed by [79]

$$\begin{aligned} I_{\text{signal}}^{\text{out}} &= G I_{\text{seed}} + (G-1) \\ I_{\text{idler}}^{\text{out}} &= (G-1)(I_{\text{seed}}+1), \end{aligned} \tag{4.10}$$

where $G \geq 1$ is the intensity gain and I_{seed} is the intensity of the seed field. The computed difference between signal and idler therefore becomes

$$I_{\text{signal}}^{\text{out}} - I_{\text{idler}}^{\text{out}} = I_{\text{seed}}, \tag{4.11}$$

and the sum

$$I_{\text{signal}}^{\text{out}} + I_{\text{idler}}^{\text{out}} \approx 2(G-1)(I_{\text{seed}}+1). \tag{4.12}$$

Finally, the relative imbalance can be formed

$$\frac{I_{\text{signal}}^{\text{out}} - I_{\text{idler}}^{\text{out}}}{I_{\text{signal}}^{\text{out}} + I_{\text{idler}}^{\text{out}}} \approx \frac{I_{\text{seed}}}{2(G-1)(I_{\text{seed}}+1)}. \tag{4.13}$$

Eqs. 4.10-4.13 describe how the signal and idler field intensities depend on the amplifier gain and the seed field intensity. When the initial seed intensity is large and the gain is low, the signal beam is dominated by the initial seed intensity while the idler remains weak. Therefore, there is a power mismatch between the two beams that limits the effectiveness of balanced detection (poor CMRR). As the gain increases, the idler contribution grows rapidly, and the signal-idler power difference is reduced. In the high-gain regime, the relative difference approaches zero. Although, the theoretical model predicts that the signal and idler power levels converge as the gain is increase, and noise reduction increases, previous experiments have observed an increase in noise at high amplification levels. This has been attributed to possible pump beam distortion when the OPA is operated in the high-gain regime [80].

When the seeded PDC configuration was first tested, it was immediately understood that the coherent seed field intensity would have to be weak and the OPA gain sufficiently high to minimise the signal-idler intensity imbalance. To reach this regime required the OPA to be pumped at intensities where spontaneous signal alone was already saturating (electronically) the detector.

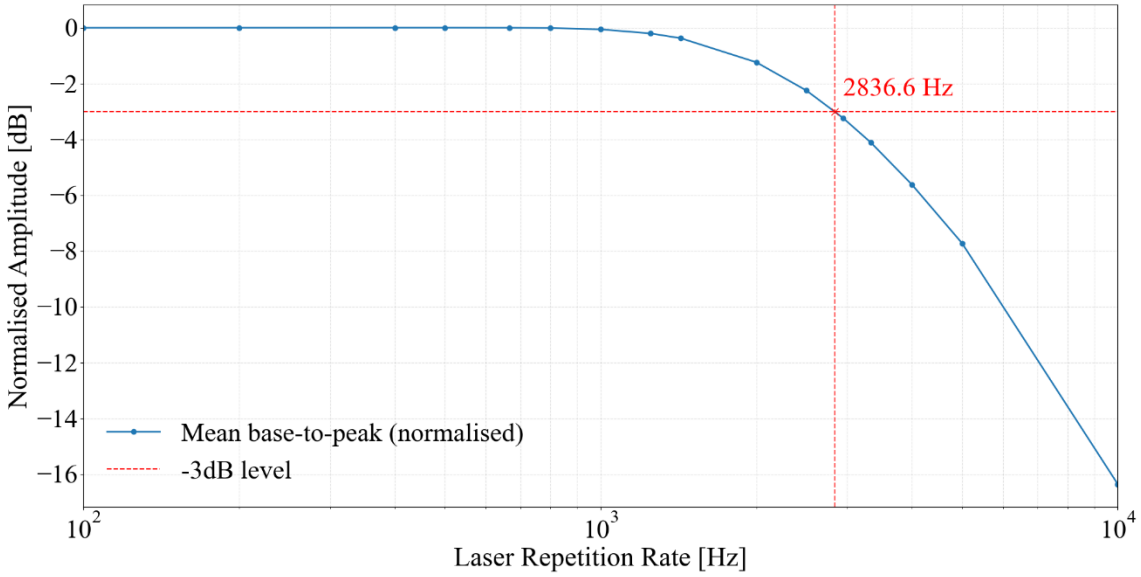

Figure 4.18 - Custom balanced detector AC bandwidth for a TIA gain of 10 MΩ. Peak-to-peak time-domain responses were recorded for different repetition rates, processed, and normalised to 0 dB so the -3 dB bandwidth was identified. Error bars are included but too small to be visible.

Consequently, the transimpedance gain of the custom balanced detector developed had to be reduced. After iteratively tuning the seeding level and pump field intensity, the feedback resistor was set to 10 MΩ, yielding a gain of 10 MV/A. By appropriately selecting R11 and C15, as described in Figure 3.26, the 3 dB bandwidth was set to approximately 3 kHz, as confirmed in Figure 4.18.

The 2 mm BBO crystal was pumped at a repetition rate of 100 kHz with an average power of 1.5 W. By sweeping the coherent seed power between 2 and 30 nW and following the same methodology described in Section 4.2, where the noise statistics of the twin-beam source were compared to those of a coherent source of the same average power, the NRF was evaluated. The results are presented in Figure 4.19**.** Where the electronic noise is subtracted, highlighting the intrinsic difference between the noise statistics of the quantum and the classical case. However, inclusion of the electronic noise contribution yields a more realistic interpretation of the quantum advantage, as presented in Figure 4.20.

It can be seen from Figure 4.20 that at low input powers, the NRF approaches 0 dB. This is attributed to the electronic noise. As can be seen from the orange curve, at low powers the ratio of the total noise (optical and electronic) and the electronic noise tend towards one. Here, the electronic noise dominates, making it difficult to determine any quantum

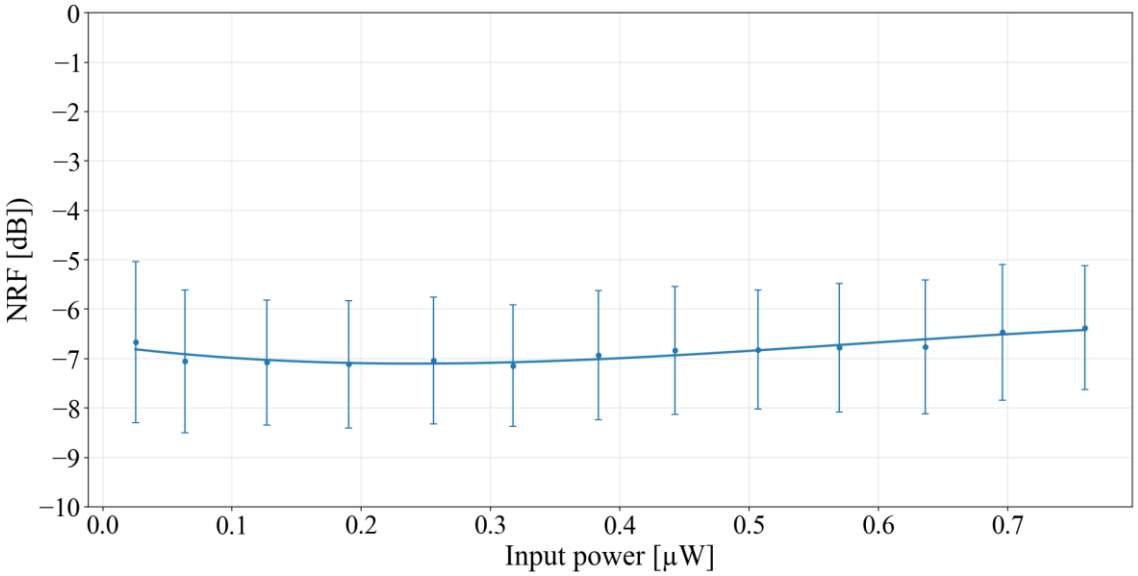

Figure 4.19 - Noise reduction factor (NRF) of twin-beams generated in by pumping (515 nm) a 2 mm BBO crystal at 100 kHz and seeding (1030 nm) with a faint coherent field. Electronic noise is subtracted. The solid line serves as a visual guide to the eye.

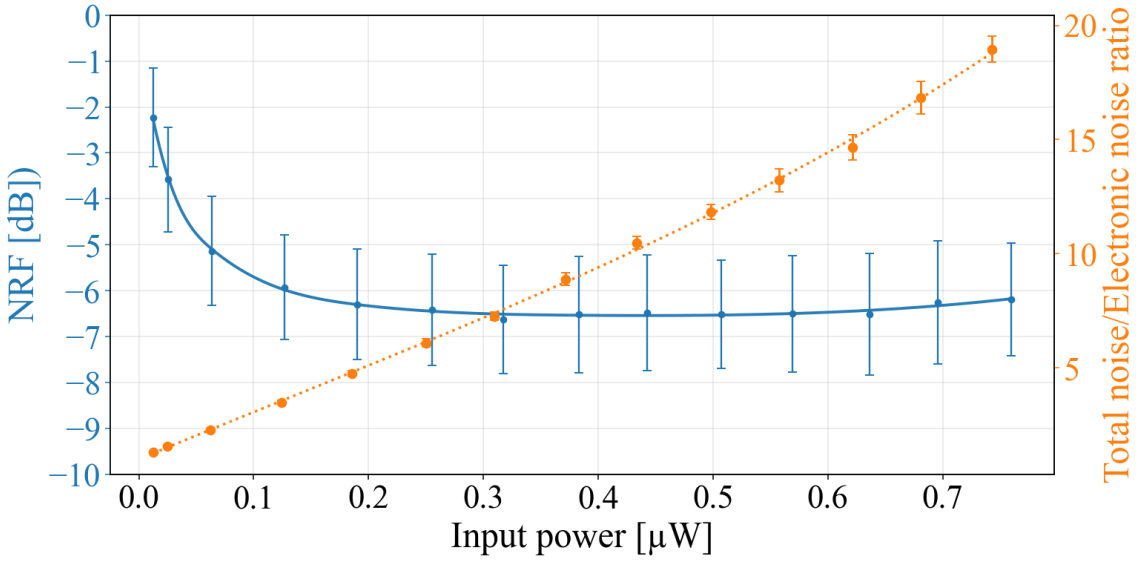

Figure 4.20 - Noise reduction factor (NRF) of twin-beams generated in by pumping (515 nm) a 2mm BBO crystal at 100kHz and seeding (1030 nm) with a faint coherent field. Electronic noise is included. The second right-hand axis shows the ratio between the total noise and the electronic noise, accounting for the NRF degradation, where the electronic noise contribution is larger. Solid and dotted lines are guides to the eye.

advantage when twin-beams are employed. To verify the effect of twin-beam squeezing, the cross-polarised twin-beams were rotated with a half-wave plate before the Wollaston prism, and the corresponding differential noise level was measured.

With this approach, the total optical power on the balanced detector remains fixed, whilst varying the splitting ratio of the twin-beams. At 0° the twin-beams are cross-polarised before the polarising beam splitter, as shown in Figure 4.14, resulting in the signal and idler being directed on separate photodiodes. In this configuration, the photon-number correlations in their photocurrent difference are maintained. As their polarisations are rotated by the HWP, the modes become increasingly mixed at the beam splitter, distributing photons from both beams on each photodiode. Consequently, this mixing progressively diminishes the correlations. The results are shown in Figure 4.21, where the noise of the twin-beams with varying polarisation rotation angles is compared to that of a shot-noise limited coherent source of identical optical power.

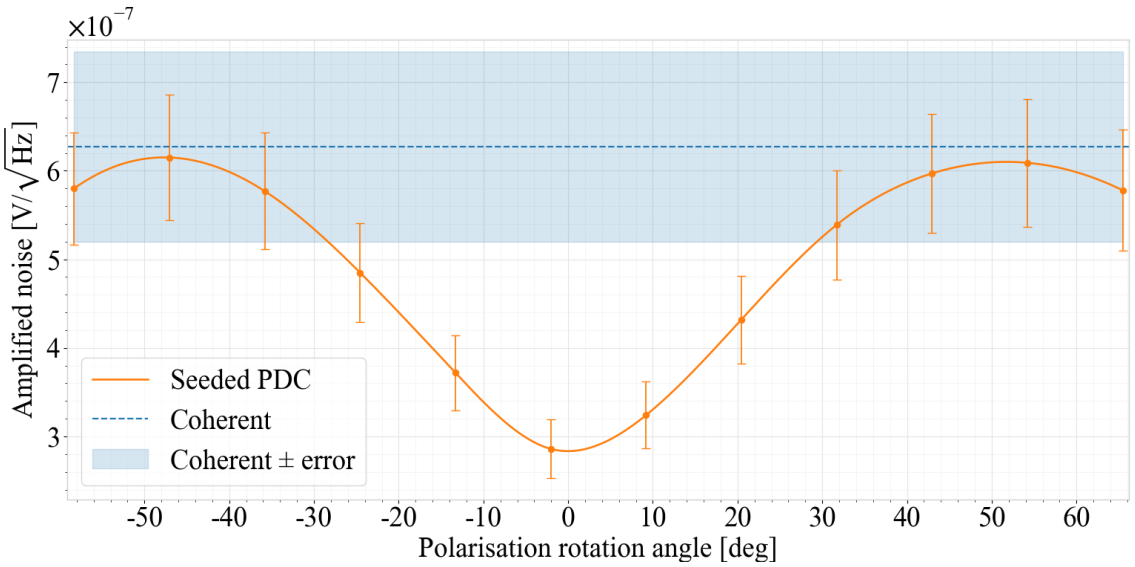

Figure 4.21 - Measured differential-noise of the twin-beams as a function of polarisation rotation angle, showing rise of noise to the shot-noise level (coherent reference) when the twin-beams are cross-polarised, as expected. The measured shot-noise level (coherent) is shown, obtained with classical balanced detection at identical optical powers. The shaded coherent ± error band illustrates the associated 1σ measurement uncertainty. Solid orange line indicates the trend.

In theory, the noise maxima should be at -45° and 45° polarisation rotation angles, assuming that signal and idler are cross-polarised having pure vertical and horizontal polarisations. In the above figure some asymmetry exists. This is because in practice the measured quantum noise versus angle is not set by optical mixing alone, it is also shaped by the effective balance of the two detector channels. Any DC power asymmetry (here the signal is 8% stronger than idler) or photodiode-responsivity mismatch, alters the CMRR of the balanced amplifier and thus affects the photocurrent difference channel.

In other words, it is not only the quantum-noise that is measured, but also a balance-dependent contribution from residual classical intensity noise. Thus, it is normal for these optoelectronic asymmetries to displace or reshape the extrema.

In this Section, twin-beams via coherently seeded SPDC have been developed and characterised. A quantum metrological tool has been developed in which photon-number correlations are confined to well-defined Gaussian spatial and temporal modes, enabling simple integration into existing balanced detection schemes. The issues identified in

Section 4.2, where the NRF degraded with optical power have been resolved, exceeding -6dB of noise reduction at optical powers near microwatt levels.

The ultrafast nature of this source makes it ideal in pump-probe measurements enabling the interrogation of fast phenomena, such as THz pulses, with sub-shot noise precision.

5 Quantum Enhanced THz-TDS

5.1 Generation of THz Radiation

5.1.1 Theory of Optical Rectification

While several methods exist for generating pulsed THz radiation, optical rectification (OR) remains one of the most effective. This is due to the capability to generate intense, and spectrally broad THz fields when compared to those generated by photoconductive antennas for example [81].

Optical rectification is a second-order nonlinear process which can be understood as a specific case of DFG, where the difference between the interacting fields approaches zero [82] (e.g. between the spectral components of a laser pulse). THz radiation is commonly generated via optical rectification by pumping electro-optic crystals with femtosecond pulses. The broad spectral bandwidth of a femtosecond pulse allows any pair of its components to interact within the nonlinear medium, contributing to the DFG. The combined result is the weighted sum of all contributions that satisfy the phase-matching condition. Consequently, a single femtosecond laser pulse is sufficient to drive optical rectification, simplifying the experimental implementation.

The total polarisation, as a power series in the electric field, has been introduced in Section 2 (Eq. 2.2). As in all second-order nonlinear effects, only the second-order term is relevant

$$\boldsymbol{P}^2(t) = \epsilon_0 \chi^{(2)} \boldsymbol{E}^2(t). \qquad \textbf{5.1}$$

Assuming that the incident light field is a plane-wave, its electric field can be expressed as

$$\boldsymbol{E}(t) = \int_{0}^{+\infty} E(\omega)\, e^{(-j\omega t)} \mathrm{d}\omega + c.c. \tag{5.2}$$

One can acquire the polarisation for optical rectification by substituting Eq. 5.2 into Eq. 5.1 so that

$$\begin{aligned} \boldsymbol{P}^2_{\mathrm{OR}}(t) &= 2\chi^{(2)} \vdots \int_0^{\infty} \int_0^{\infty} \boldsymbol{E}(\omega_1)\boldsymbol{E}^*(\omega_2)\, e^{-j(\omega_1-\omega_2)t} \mathrm{d}\omega_1 \mathrm{d}\omega_2 \\ &= 2\chi^{(2)} \vdots \int_0^{\infty} \int_0^{\infty} \boldsymbol{E}(\omega+\Omega)\, \boldsymbol{E}^*(\omega) e^{-j\Omega t} \mathrm{d}\Omega \mathrm{d}\omega, \end{aligned} \tag{5.3}$$

Where Ω is the difference of the two contributing optical frequency components. The radiated electric field, in the far field, is proportional to the second derivative of Eq. 5.3 with respect to time

$$\boldsymbol{E}(t) \propto \frac{\partial^2}{\partial^2 t} \boldsymbol{P}^2_{\mathrm{OR}}(t). \tag{5.4}$$

By considering the contributing fields $E(\omega_1) = A_1 e^{-jk_1 r}$ and $E(\omega_2) = A_1 e^{-jk_2 r}$ then as per Eq. 2.18 using the scalar approximation for simplicity

$$P_{\mathrm{NL}}(\Omega_{\mathrm{THz}}) = dE(\omega_1)E(\omega_2) = dA_1 A_2^* e^{-jk_3 r}, \tag{5.5}$$

where

$$\Omega_{\mathrm{THz}} = \omega_1 - \omega_2 \tag{5.6}$$

and

$$k_{\mathrm{THz}} = k_1 - k_2. \quad \textbf{5.7}$$

Here, Ω_{THz} and $\mathrm{k_{THz}}$ are the frequency and the wave vector of the generated THz field, with ω_1, ω_2 , k_1 and k_2 denoting the frequencies and wave vectors of the optical fields contributing to the generated field.

By appropriately selecting the thickness of the nonlinear medium, so that it is shorter than the coherence length as defined in Eq. 2.23**,** efficient THz generation can be achieved. Since the interacting optical fields are of much higher frequency than Ω_{THz} they are effectively degenerate ($\omega_1 \approx \omega_2 \approx \omega_0$). By taking the ratios of Eqs. 5.6 - 5.7,

$$\frac{\omega_1 - \omega_2}{k_1 - k_2} = \frac{\Omega_{\mathrm{THz}}}{k_{\mathrm{THz}}}, \quad \textbf{5.8}$$

the left-hand side of Eq. 5.8 approximates to $\frac{\Delta\omega}{\Delta k}$ since ($\Omega_{\mathrm{THz}} \ll \omega_0$) and hence

$$\frac{\Delta\omega}{\Delta k} = \frac{\Omega_{\mathrm{THz}}}{k_{\mathrm{THz}}}. \quad \textbf{5.9}$$

The left-hand side of the resulting equation is the group velocity of the input optical pulse, and the right-hand side is the phase velocity of the THz. Therefore, to achieve efficient THz generation the group velocity of the optical pulse must match the phase velocity of THz pulse throughout the interaction length. The geometry described by the above equations (collinear phase matching), results in high THz efficiency but also good THz beam quality, due to the long interaction length.

5.1.2 Experimental THz Generation via Optical Rectification

When choosing the nonlinear material for THz generation, three main figures of merit must be considered. Firstly, the material needs to possess a high nonlinear susceptibility which enhances the conversion efficiency of the interaction. Secondly, the absorption characteristics at the pump and THz wavelengths must be minimal so that both fields propagate along the material efficiently. Lastly, a long coherence length is advantageous as it maximises the interaction length of the fields within the material.

In the present work, Gallium Phosphide (GaP) was chosen as the nonlinear medium for THz generation, offering a favourable combination of properties for this purpose. Its large nonlinear coefficient ($d_{14} = 20\ \mathrm{pm/V}$) and broad transparency range ($0.55 - 1.6\ \mu\mathrm{m}$) provide the necessary conditions for efficient optical rectification.

As summarised in Table 5.1, GaP is the only crystal among common candidates that supports collinear phase matching at 1030 nm while exhibiting no two-photon absorption at this wavelength. This combination is particularly significant. Collinear phase matching enables high-efficiency, broadband THz generation without resorting to more complicated geometries or pulse front tilting. Furthermore, the absence of two-photon absorption ensures that pump energy is not dissipated through competing nonlinear processes that would otherwise degrade conversion efficiency. These properties make GaP directly compatible with Ytterbium-doped Potassium Gadolinium Tungstate (Yb:KGW) laser systems, such as the one employed here, establishing it as the natural choice for this setup. [83][84].

Table 5.1 Properties of common nonlinear crystals for 1030 nm pumped THz generation.

Crystal	Collinear phase matching at 1030nm	2PA at 1030nm
$ZnTe$	No	High
GaP	Yes	None
$GaAs$	No	High
$ZnGeP_2$	No	Present
$LiNbO_3$	No	None

Here, we generate THz by placing a 1mm long n-type GaP crystal (cut in the 110 plane) in a way so that the p-polarised pump beam is incident normal to the crystal surface and thus satisfying the phase-matching condition. To maximise THz generation, the crystal was positioned so that the [001] crystallographic axis is orientated at $\theta \simeq 55°$ with respect to the horizontally polarised pump.

The THz field polarisation orientation can be computed using

$$\Phi = \arctan(2\cot\theta), \qquad \textbf{5.10}$$

where Φ is defined as the angle between the THz field and the [001] crystallographic axis [85].

From Eq.5.10 it can be extracted that the polarisation of the THz field is roughly $54.5°$ to the [001] axis, suggesting that the THz field is almost p-polarised.

The selected crystal in this instance was lightly doped, as a heavily doped crystal would increase the likely hood of free-carrier absorption and thus reducing THz transmission. Using a crystal cut in the 110 plane provides access to the highest nonlinear tensor element of the Zincblende lattice, maximising the nonlinear interaction strength [86].

Although high pump intensities improve the conversion efficiency, they can also lead to saturation of the nonlinear process within the crystal. To investigate this, the experimental setup shown in Figure 5.1 was used to measure the optical rectification conversion efficiency, defined as the ratio of THz output power to incident pump power, for three different fixed beam diameters of 0.88 mm, 1.05 mm, and 3.50 mm. The THz output power was obtained using the Gentec THZ5I-BL-BNC pyroelectric detector, while the incident pump power was measured with the Gentec UP25N-100H-H9-D0 thermal detector. Increasing the pump beam size to 3.50 mm resulted in the highest conversion efficiency and THz output power. Saturation was observed at a conversion efficiency of $\sim 7 \times 10^{-7}$ when the OR crystal was pumped with 30 W of average power, as shown in Figure 5.2.

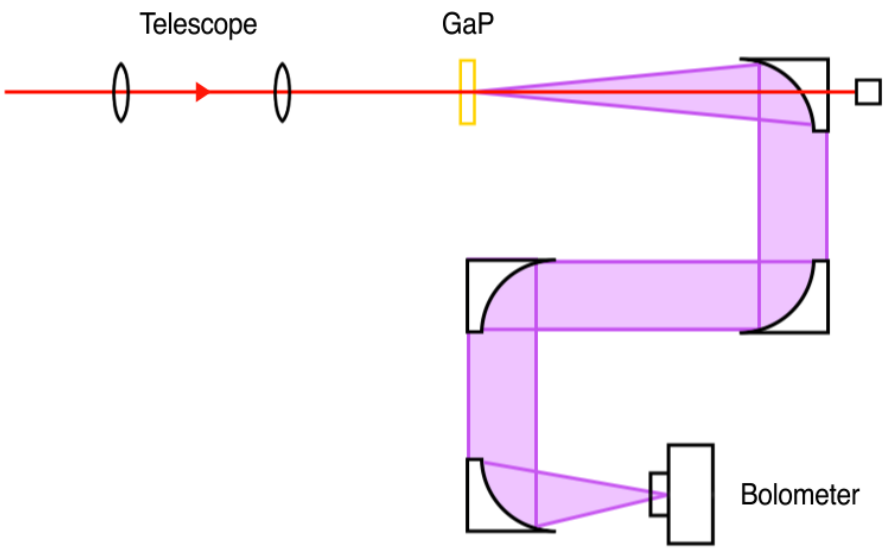

Figure 5.1 - Experimental setup for measuring THz conversion efficiency as a function of pump beam size. The red beam denotes the pump beam, while the purple represents the generated THz radiation. The pump waist was varied between 0.88 mm, 1.05 mm, and 3.50 mm, with THz output detected by a bolometer and incident pump power measured by a thermal power meter.

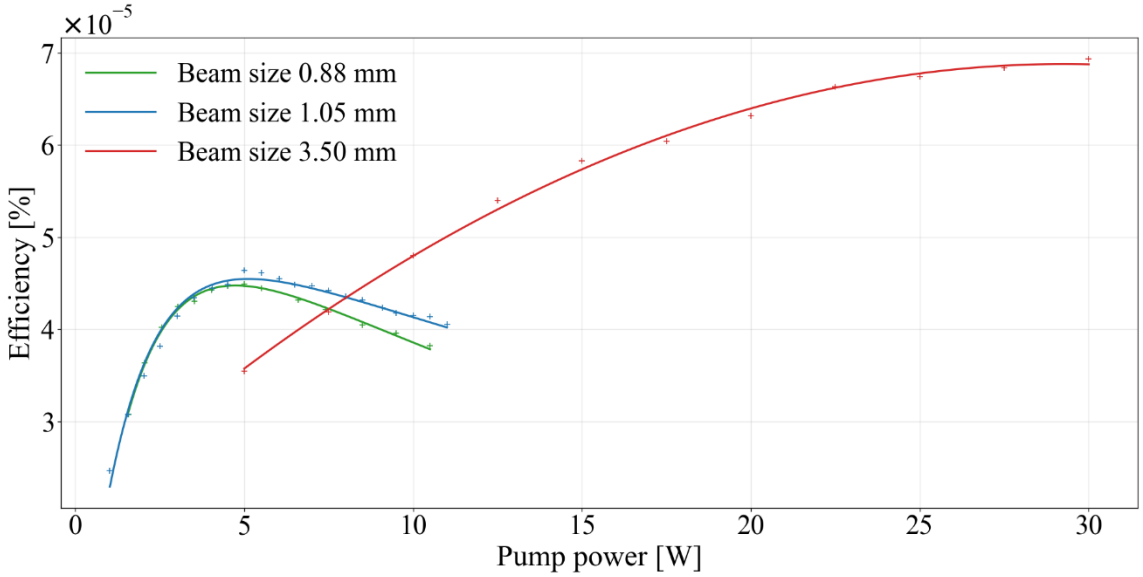

Figure 5.2 - THz conversion efficiency as a function of pump power for three different beam sizes. Optimal beam size was found to be 3.5 mm ($1/e^2$), providing the highest conversion efficiency before reaching saturation at 30 W.

5.2 Detection of THz Pulses

5.2.1 Theory of Electro-Optic Sampling

Electro-optic sampling can exploit the electro-optic (EO) effect to analyse time-varying electric fields. In this second-order nonlinear interaction, an applied electric field can modify the refractive index of the medium. GaP is an isotropic, non-centrosymmetric crystal and therefore exhibits no inherent birefringence. However, when an external electric field is applied, the induced EO effect can make the refractive index polarisation-dependent, introducing birefringence proportional to the field strength.

If we consider an electric field having an oscillating component at ω, and a steady component ($\omega = 0$), then

$$E(t) = E(0) + \mathrm{Re}\{E(\omega)e^{j\omega t}\}. \quad \textbf{5.11}$$

By substituting this electric field expression into Eq. 2.8 where the material's nonlinearities that are above second order are assumed to be negligible, the induced polarisation in the medium is given by

$$P_{\mathrm{NL}}(t) = P_{\mathrm{NL}}(0) + Re\{P_{\mathrm{NL}}(\omega)e^{j\omega t}\} + Re\{P_{\mathrm{NL}}(2\omega)e^{j2\omega t}\}, \quad \textbf{5.12}$$

where

$$P_{\mathrm{NL}}(0) = d[2E^2(0) + |E(\omega)|^2] \quad \textbf{5.13}$$

$$P_{\mathrm{NL}}(\omega) = 4dE(0)E(\omega) \quad \textbf{5.14}$$

$$P_{\mathrm{NL}}(2\omega) = dE(\omega)E(\omega). \quad \textbf{5.15}$$

Thus, the polarisation density consists of components at 0, ω and 2ω.

If we assume that the field oscillating at ω is considerably smaller in magnitude than the steady component $(|E(\omega)|^2 \ll |E(0)|^2)$, then the second-harmonic component (Eq. 5.15) can be ignored. Therefore, the linear relationship between the polarisation $P_{\mathrm{NL}}(\omega)$ and the optical field $E(\omega)$ can be extracted from Eq. 5.14. This equation can also be written in the form

$$P_{\mathrm{NL}}(\omega) = \epsilon_0 \Delta\chi E(\omega), \qquad \textbf{5.16}$$

where

$$\Delta\chi = \frac{4d}{\epsilon_0} E(0) \qquad \textbf{5.17}$$

represents the susceptibility change proportional to the DC electric field. One can obtain the equation giving the refractive index change by differentiating the relation $n^2 = 1 + \chi$ so that $2n\Delta n = \Delta\chi$ and substituting into Eq. 5.17 so that

$$\Delta n = \frac{2d}{n\epsilon_0} E(0). \qquad \textbf{5.18}$$

It is evident that the static field $E(0)$is coupled with the oscillating field $E(\omega)$ via the nonlinear medium, corresponding to the Pockels effect. In the context of THz detection, the static field is represented by the THz field so that Eq. 5.19 becomes

$$\Delta n = \frac{2d}{n\epsilon_0} E_{\mathrm{THz.}} \qquad \textbf{5.19}$$

The material is effectively linear with a refractive index that is controlled by the instantaneous THz field.

To directly measure the temporal profile of a THz electric field, electro-optic sampling (EOS) is employed. A linearly polarised probe beam co-propagates with the THz field and is spatially overlapped inside an EO crystal. The slow-varying THz field alters the refractive index ellipsoid of the EO crystal, via the Pockels effect, inducing a birefringence proportional to the instantaneous THz field.

When the probe field temporally overlaps the THz field inside the crystal, it experiences the altered refractive index and thus its polarisation is modified. A Wollaston prism is used to analyse the polarisation change by separating the probe into two orthogonally polarised beams. Balanced detection allows the measurement of the THz-induced polarisation rotation as a differential photocurrent signal.

In the presence of an electric field, the ellipsoid of the refractive index of a zincblende crystal is symmetric and can be expressed as

$$\frac{x^2 + y^2 + z^2}{n_0^2} + 2\gamma_{41}E_x yz + 2\gamma_{41}E_y xz + 2\gamma_{41}E_z xy = 1, \qquad \textbf{5.20}$$

where n_0 is the refractive index of the crystal in the absence of an external electric field, E_x, E_y and E_z are the components of the applied field, and γ_{41} is the linear electro-optic coefficient of the crystal.

Expanding Eq. 5.20 for small perturbations and considering an electric field polarised along the z-axis of the crystal ($E = E_z$), it can be observed that the field introduces a differential change in refractive index along the affected axes.

$$n_x = n_0 - \frac{1}{2}n_0^3\gamma_{41}E_z \quad , \quad n_y = n_0 + \frac{1}{2}n_0^3\gamma_{41}E_z. \qquad \textbf{5.21}$$

Thus, the birefringence is induced in the x-y plane is

$$\Delta n = n_y - n_x = n_0^3 \gamma_{41} E_z. \quad \textbf{5.22}$$

Therefore, each affected axis experiences a change in refractive index proportional to the applied field

$$\Delta n = -\frac{1}{2} n_0^3 \gamma_{41} E. \quad \textbf{5.23}$$

Light propagating through a medium of refractive index n over a distance d, accumulates an optical phase

$$\Phi = \frac{\omega n d}{c_0}, \quad \textbf{5.24}$$

where ω is the angular frequency and c_0 the speed of light in a vacuum. Accordingly, the phase change in the x-y plane is

$$\Delta\Phi = \frac{\omega d}{c_0}\left(n_y - n_x\right) = \frac{\omega d n_0^3 \gamma_{41} E_z}{c_0}. \quad \textbf{5.25}$$

The basis of EOS is built on the induced phase retardation described by Eq. 5.25, where the instantaneous THz field is encoded on the polarisation state of the spatiotemporally overlapped probe.

5.2.2 Experimental Electro-Optic Sampling

In this work, a 300 μm-long (110) cut GaP crystal was used as the detection crystal. The probe beam is first linearly polarised through a polariser, and its polarisation was set with a half-wave plate (HWP) to the optimal orientation relative to the THz field.

In GaP, the probe and THz field should be oriented so that their polarisations are orthogonal or parallel. In this setup, the probe was set to be polarised perpendicularly to the THz field. The detection crystal was subsequently rotated until the THz signal was maximised. This maximum corresponds to the configuration where the reference axis of the crystal is perpendicular to the THz field [87].

After passing the EO crystal, the probe beam passes through a quarter-wave plate (QWP) and a Wollaston prism, which separates its horizontal and vertical components, before they are directed onto a balanced detector. The QWP is placed so that the polarisation of the probe is biased so that the intensity of s and p components are equal in the absence of THz. Consequently, the generated photocurrents on the balanced receiver subtract perfectly, and we get a balanced output. In the presence of THz, a phase retardation is introduced, and the polarisation becomes elliptical.

The implemented EOS scheme is illustrated in Figure 5.3, where the polarisation state of the probe beam is annotated for both with and without THz. As it can be seen from the figure, when THz is present it causes an imbalance of light on the photodiodes and consequently a differential output voltage. By temporally scanning one pulse relative to the other, the full THz waveform can be constructed. This was implemented by adding retroreflective delay-line stage on the pump-beam path.

Typically, the phase retardation and hence imbalance caused by THz is very small and buried in noise, therefore advanced detection techniques, like lock-in amplification, need to be implemented to quantify them.

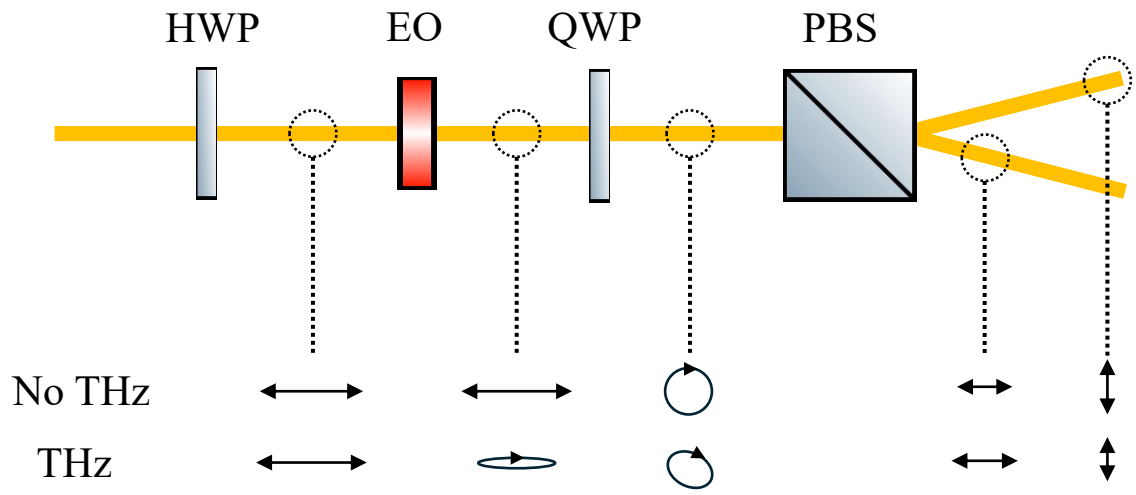

Figure 5.3 -Implemented EOS scheme. The HWP allows tuning the orientation of the linearly polarised probe to the optimal position. The probe polarisation is converted to circular/elliptical by the QWP such that the scheme is perfectly balanced in the absence of THz. When the THz field is applied, a differential imbalance is induced proportional to the THz field. Examples of the probe polarisation evolution with and without THz are shown.

5.2.3 Theory of Lock-in Amplification

In the case where two equal optical fields are incident on an ideal balanced detector, the differential output is 0 V. For the custom detector developed in this work, operating at a transimpedance gain of 10 MV/A and a 3 dB bandwidth of 2.9 kHz, the time-domain RMS noise is determined by integrating the measured dark voltage noise spectrum over the effective bandwidth following

$$V_{\mathrm{rms}} = \sqrt{\int_{f_1}^{f_2} e_n^2(f)\mathrm{d}f} \qquad \textbf{5.26}$$

The integration of Eq. 5.26 yields an RMS voltage noise of 65 μV.

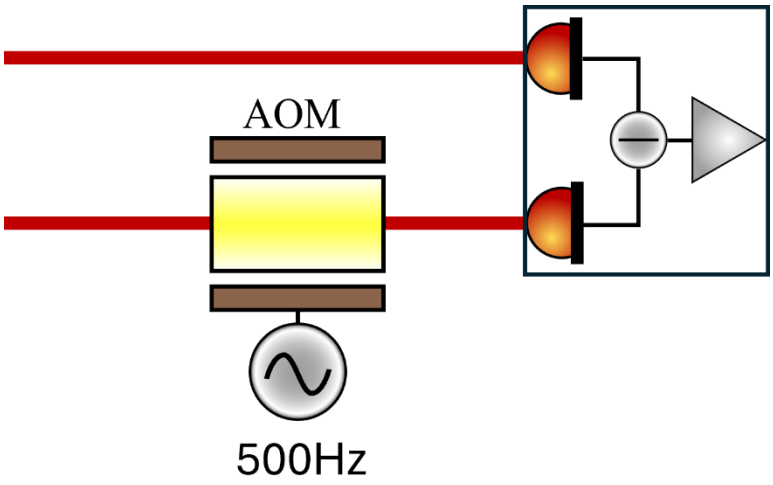

Figure 5.4 - Conceptual illustration of the principle used of introducing a controlled photocurrent imbalance via AOM modulation. This schematic represents the basis of the following simulations, where a sinusoidal differential is photocurrent is generated.

To simulate the detector's response under controlled imbalance, an acousto-optic modulator (AOM) is conceptually introduced in one of the beam paths. The optical intensity on the corresponding photodiode can be modulated sinusoidally (f = 500Hz), as seen Figure 5.4 **.** Consequently, a controlled photocurrent imbalance, is introduced at the input of the amplifier. This is subsequently amplified, appearing as a sinusoidal voltage at the detector's output.

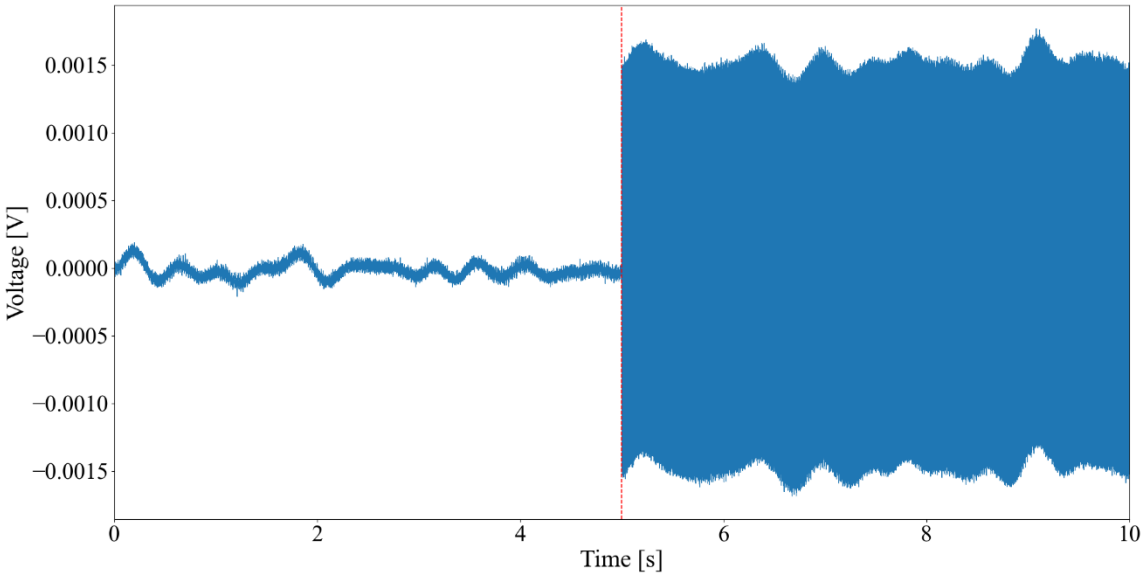

Figure 5.5 - Detectable output for a 150 pA modulation amplitude. Here, the differential signal induced is high enough so that it is easily digitised without advanced techniques

If the modulation amplitude is large enough, the differential output will be clearly observed and easily digitised. An example of this can be seen in Figure 5.5 where a modulation amplitude corresponding to a 150 pA differential photocurrent is introduced at $t = 5$ s. In this configuration, the signal is amplified to 1.5 mV, much larger than the RMS noise calculated using Eq. 5.26, therefore standard analogue-to-digital digitisation is adequate efficiently analysing the signal statistics.

When the periodic differential signal becomes small enough so that it is comparable or even smaller than the RMS noise, the situation becomes a lot more complex. To illustrate this, the modulation magnitude is decreased by two orders of magnitude. Post amplification the detector should output a sinusoidal signal of amplitude 15 μV.

As the broadband V_{RMS} noise is more than four times (65 μV) more than the signal of interest, it cannot be distinguished from the noise, as seen in Figure 5.6. Although the periodic component seems lost in noise, it still possesses a well-defined frequency and phase. By exploiting this property, lock-in amplification isolates and recovers the signal through phase-sensitive detection.

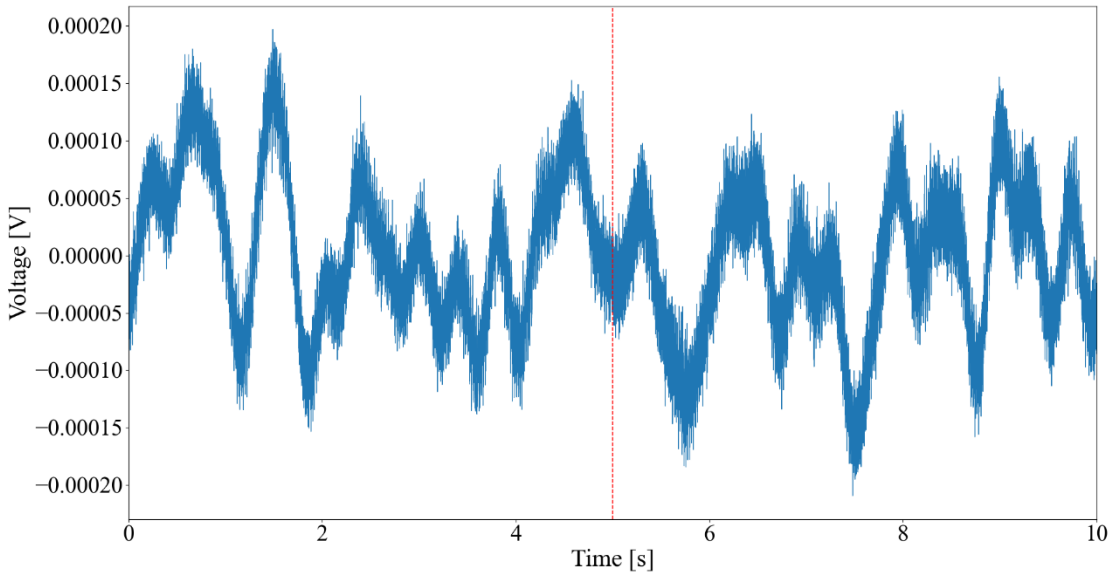

Figure 5.6 - Undetectable output for a 1.5 pA modulation amplitude. Here, even when the modulation starts at t=5 s, no observable signal is visible, as it is drowned in noise.

This is achieved by multiplying the noisy detector output (Figure 5.6) by a reference waveform at the same modulation frequency (in this case 500 Hz). The detector output signal may be written as

$$V_{\text{out}}^{\text{bal}}(t) = V_{\text{sig}}\sin\left(\omega_{\text{sig}}t + \theta_{\text{sig}}\right) + V_{\text{RMS}}. \quad \textbf{5.27}$$

Where V_{sig}, ω_{sig} and θ_{sig} represent the amplitude, frequency and the phase offset of the wave, respectively and V_{RMS} represents broadband noise. The reference, often generated from an externally provided signal is a pure sinusoid

$$V_{\text{ref}}(t) = \sin(\omega_{\text{ref}}t + \theta_{\text{ref}}). \quad \textbf{5.28}$$

Multiplying both signals generates signal components at both the sum and difference frequencies,

$$V_{\text{mix}}(t) = \frac{1}{2}V_{\text{sig}}\left[\cos\left(\left(\omega_{\text{sig}} - \omega_{\text{ref}}\right)t + \Delta\theta\right) - \cos\left(\left(\omega_{\text{sig}} + \omega_{\text{ref}}\right)t + \Sigma\theta\right)\right], \quad 5.29$$

Where $\Delta\theta = \theta_{\text{sig}} - \theta_{\text{ref}}$ and $\Sigma\theta = \theta_{\text{sig}} + \theta_{\text{ref}}$.

A low-pass filter rejects the high-frequency components, removing the sum term. In turn, if $\omega_{\text{sig}} = \omega_{\text{ref}}$, the lock-in output becomes

$$V_{\text{out}}^{\text{lock}}(t) = \frac{1}{2}V_{\text{sig}}\cos(\theta_{\text{sig}} - \theta_{\text{ref}}). \quad \textbf{5.30}$$

The lock-in output signal is directly proportional to the amplitude of the original signal, depending on its phase relative to the applied reference. In essence, a very narrowband measurement is performed, where all the broadband noise and unrelated components are rejected. A low-pass filter which succeeds the demodulation stage, defines the balance between noise suppression and response time. Narrow filtering results in a cleaner signal at the expense of a slower response.

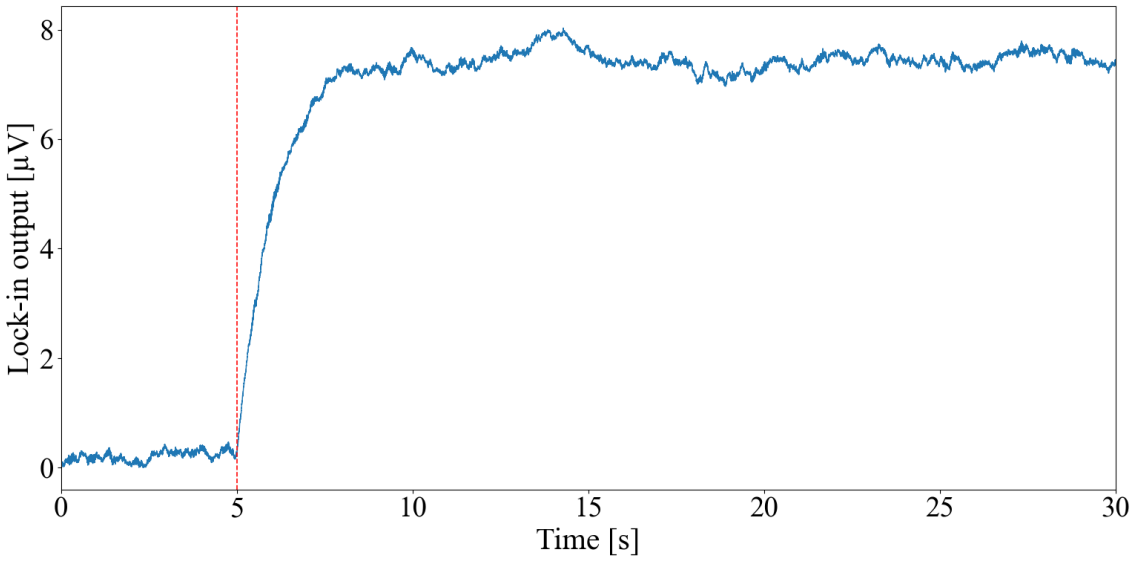

Figure 5.7 - Lock-in output for a 1.5 pA modulation amplitude. Example of how powerful the lock-in technique can be in extracting a periodic signal previously buried in noise.

By using a simple numerical model, where a first-order low-pass filter has been assumed, the lock-in output was simulated under the same conditions as in Figure 5.6, where the signal was indistinguishable from noise. As illustrated in Figure 5.7 as soon as the signal is introduced at $t = 5$ s, the lock-in response rises and settles to a steady DC value equal to $\frac{1}{2}V_{\text{sig}} = 7.5\ \mu\text{V}$, demonstrating the effectiveness of phase-sensitive detection. The fluctuations superimposed on the steady DC voltage correspond to noise components within the 0.16 Hz detection bandwidth.

5.3 Initial THz-TDS System

This part of the work was undertaken in close collaboration with another PhD student, Lennart Hirsch, who focused on optimising Yb: KGW-based THz-TDS generation and detection. The THz-TDS setup that was initially developed is illustrated in Figure 5.8.

The core of the system comprised the THz generation and detection components, described in Sections 5.1 and 5.2 respectively. The THz beamline (yellow) guides the radiation from the generation crystal, through the sample under test and subsequently on

the detection crystal. The pump beam is rejected by passing through a hole in the first off-axis parabolic mirror.

To generate the probe beam (blue), a small portion of the pump beam (red) is separated using a beam splitter. Generally, not a lot of light is required for the probe, and it is dependent on the sensitivity of the detector. Since the laser used in our setup can deliver up to 400 μJ of energy per pulse, at a repetition rate of 100 kHz, only a small fraction is required for electro-optic sampling.

To this end, a variable attenuator comprising of a thin film Brewster-type polariser and quartz half-wave plate was placed so that energy can be routed between the pump and the probe arms. To enable further control of the probe beam power, a half-wave plate followed by a Glan Taylor prism are placed in the probe path. Following the prism, an additional half-wave plate, allows optimisation of the EOS interaction, as mentioned in Section 5.2.1, by controlling the orientation of the probe polarisation.

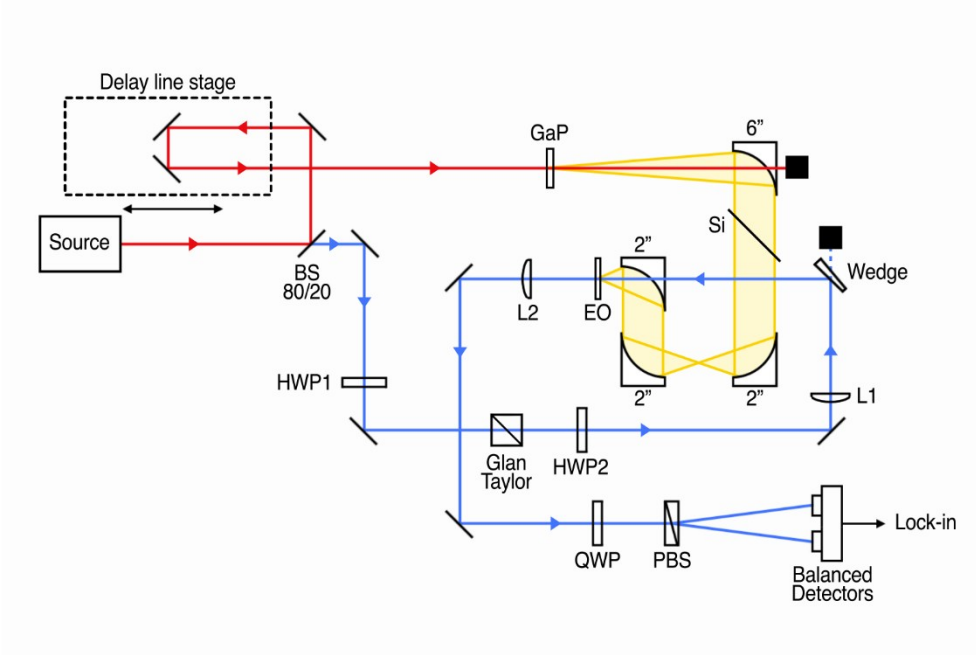

Figure 5.8 - A schematic view of the initial THz TDS system [94]. BS: beam splitter | HWP: Half-wave plate | QWP: quarter-wave plate | PBS: polarising beam splitter (Wollaston Prism) | GaP: gallium phosphide crystal | EO: electro-optic crystal (also GaP) | L3 focused the probe beam onto the EO detection crystal plane, L4 recollimated it after detection. The wedge helps direct a fraction of the light transmitted from the 80/20 BS onto the EO crystal.

The probe beam is then focused onto the EO detection crystal (L1) and recollimated (L2) before being directed onto the Wollaston prism. This is essential, as non-collimated light inside birefringent elements, may introduce a phase retardation between different spatial parts of the beams, lowering the extinction ratio and thus sensitivity.

For efficient THz detection, spatiotemporal overlap between the THz field and the probe pulse must occur at the EO crystal detection plane. To achieve spatial overlap, the probe beam is aligned onto the same focal spot as the THz beam. A small fraction of the pump-beam, slightly clipped by the first off-axis parabolic mirror, was used to visualise the THz beam. Because the residual light followed the same optical path, it was used as a reference when spatially overlapping the THz with the probe.

To achieve temporal overlap, the residual pump and the probe pulses were referenced to the TTL synchronisation signal, provided by the laser. By adjusting the pump retroreflective delay line and comparing the relative arrival times of the pump and probe pulses using a fast photodiode, placed at the EO detection plane, a coarse estimate of their temporal alignment was obtained.

Subsequently, the fast photodiode was replaced with a BBO crystal, and sum-frequency generation between the probe and the residual pump, as described in Section 4.3, was achieved. Observation of the SFG signal, at 343 nm, confirmed spatiotemporal overlap at the detection plane, and thus the BBO crystal was replaced by the GaP detection crystal.

Optimising key acquisition parameters is pivotal in improving the stability and noise performance of THz-TDS. These include the lock-in amplifier settings, sampling frequency, delay-line step size and settling time between measurements.

The lock-in amplifier's time constant, determines the effective measurement bandwidth. A shorter time constant (wider low-pass filter) enables faster settling times of the output at the expense of more RMS noise. A third-order low-pass filter with a 100 ms time-constant was selected, corresponding to 0.8 Hz 3 dB bandwidth, as it provided the best balance between acquisition speed and signal-to-noise ratio. A 1.3 s waiting time was introduced after each step, allowing both the mechanical motion and the low-pass filter to settle before the next measurement point.

A sampling rate of 6.7 kS/s was used, collecting data for 1 s at each delay position. As a result, 6700 samples were acquired per point, from which the signal statistics were computed.

The temporal resolution of the THz-TDS setup is governed by the step-size of the delay-stage, which was set at 2 μm. Hence, each increment corresponds to 13 fs of optical delay. The total scan range was between 0.5 mm-3 mm, depending on if system optimisation took place or a full-THz waveform was acquired.

Initial measurements were performed using the THz-TDS system described. These provided an early indication of the system's signal quality, highlighting several limitations inherent to the initial setup. Notable oscillations following the main THz peak were observed, indicating strong water absorption. Such effects deplete energy from the main THz peak and thus reduce the overall signal-to-noise ratio.

Additionally, as mentioned in section 5.1.2, the large pump beam diameter, although advantageous for efficient THz generation without saturation, introduced geometrical challenges. Firstly, the 3 mm aperture of the first off-axis parabolic (OAP) mirror proved to be too small, resulting in inefficient pump beam rejection. Furthermore, the produced THz radiation propagated with a small divergence angle, such that the THz beam was a lot smaller than the OAP mirror diameter. Therefore, the THz lost through the 3 mm rejection aperture, was significant.

These results and observations motivated the optimisation of the system. To mitigate water absorption losses, the THz beamline was purged with nitrogen reducing the humidity from 45 % down to 5 %. A pivotal re-design of the THz beam path was implemented, reducing overall clipping and enhancing THz collection efficiency.

The optimisation steps, along with several other system improvements beyond the scope of this work, were carried out by Lennart Hirsch, as part of his doctoral research. These developments are summarised in Hirsch *et al.* [88] to which I contributed as a co-author.

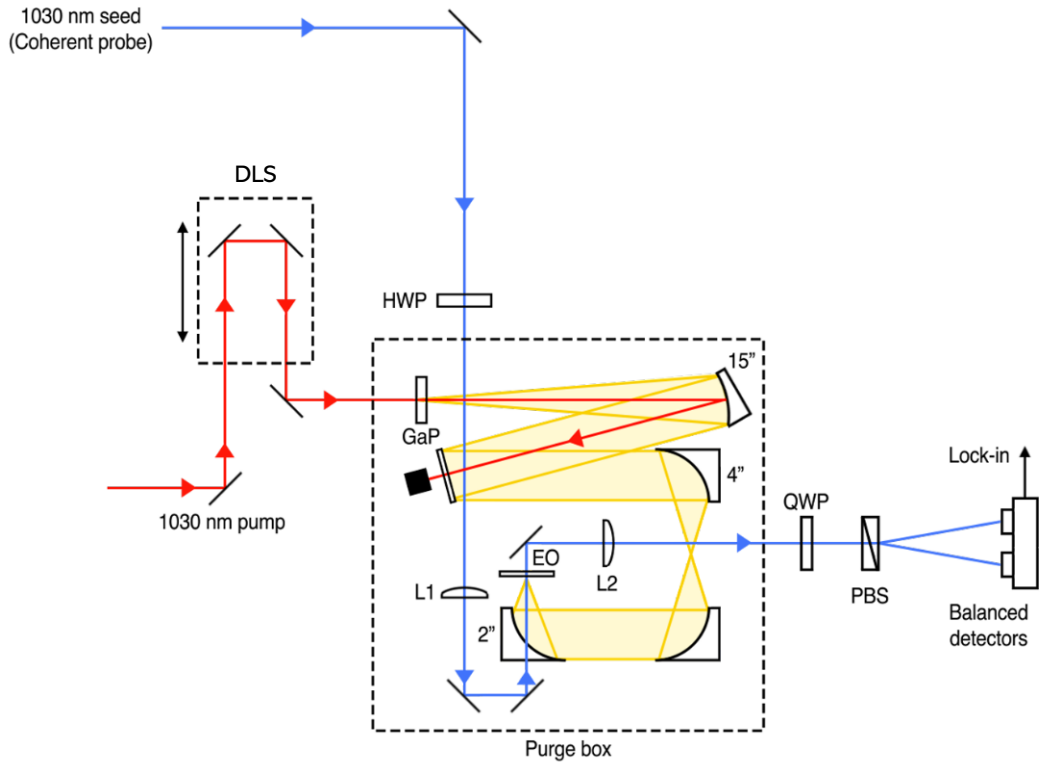

Figure 5.9 - Schematic of the optimised THz-TDS system showing the implementation of the improved THz beamline and purge box. The optical layout is based on the initial setup shown in **Figure 5.8**, with the updated mirror geometry within the THz beamline designed to minimise losses. The sealed purge box provides a controlled, low-humidity environment, thereby reducing atmospheric absorption.

The overall layout of the optimised system is summarised in Figure 5.9. The acquired THz-TDS trace and the corresponding power spectrum, when pumped with 17 W is shown in Figure 5.10, achieving an SNR of 71.8 dB.

This represents considerable improvement from the traces taken before the optimisations, yielding an SNR of 46 dB, highlighting the effectiveness of the implemented improvements to the system. The probe power used in these measurements was ~ 100 µW in both cases whilst the custom detector was not deployed in either case.

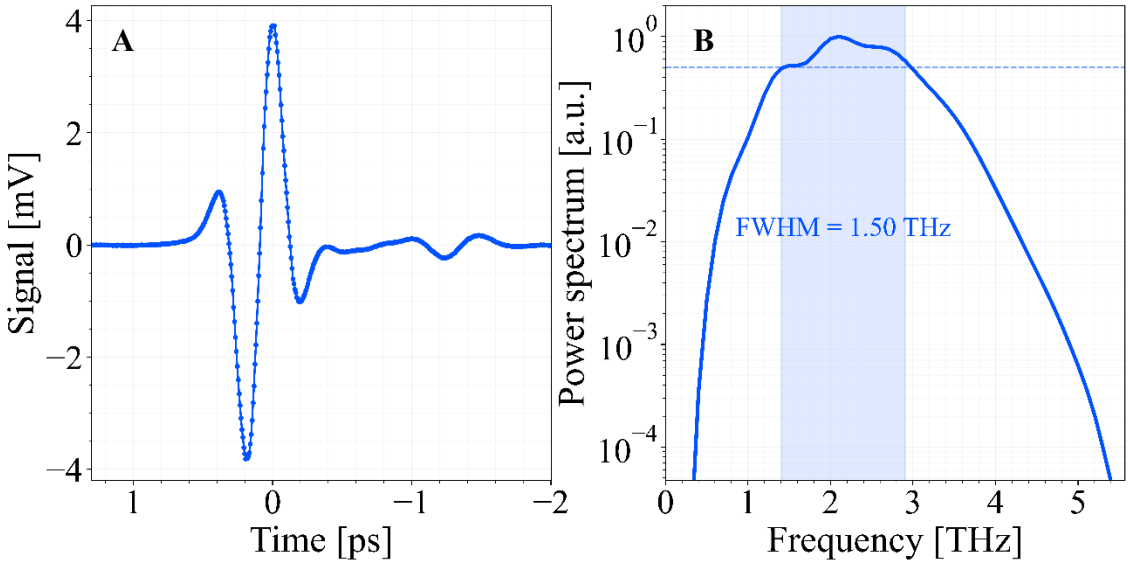

Figure 5.10 – **A**: Acquired THz-TDS trace when pumping the OR crystal with 17 W of pump power (SNR ≈ 71.8 dB) | **B**: Corresponding power spectrum, derived from the one-sided FFT of the THz-TDS trace.

5.4 Integrating the Twin-Beams in the THz-TDS System

In this section, the integration of the twin-beams developed in Section 4.3 into the THz-TDS setup is described in detail. The copropagating, orthogonally polarised signal and idler are routed through the back of the final off-axis parabolic mirror and onto the EO crystal. A half-wave plate (HWP2) was inserted before the EO crystal so that the polarisation of the probes can be adjusted to the optimal orientation relative to the THz field.

Subsequently, as in conventional THz-TDS the probe pulses are directed towards the balanced detector. An important deviation here, is that the before the Wollaston prism, the quarter-wave plate is replaced by a half-wave plate (HWP3) on the detection side. This change is essential, as using a QWP would mix the signal and idler photons, and thereby destroy the correlations and quantum advantage.

This configuration, a form of relative ellipsometry, is not as sensitive as the conventional QWP-based schemes, but it allows a demonstration of the achievable enhancement

through quantum metrological techniques, such as the developed twin-beam state. Figure 5.11 illustrates the overall configuration of the system.

Temporal overlap between the probe and the THz pulses was established as described in the previous section. Here, the signal was the probe beam, interacting wave with the THz so that its polarisation is altered. The idler co-propagated with the signal, sharing identical

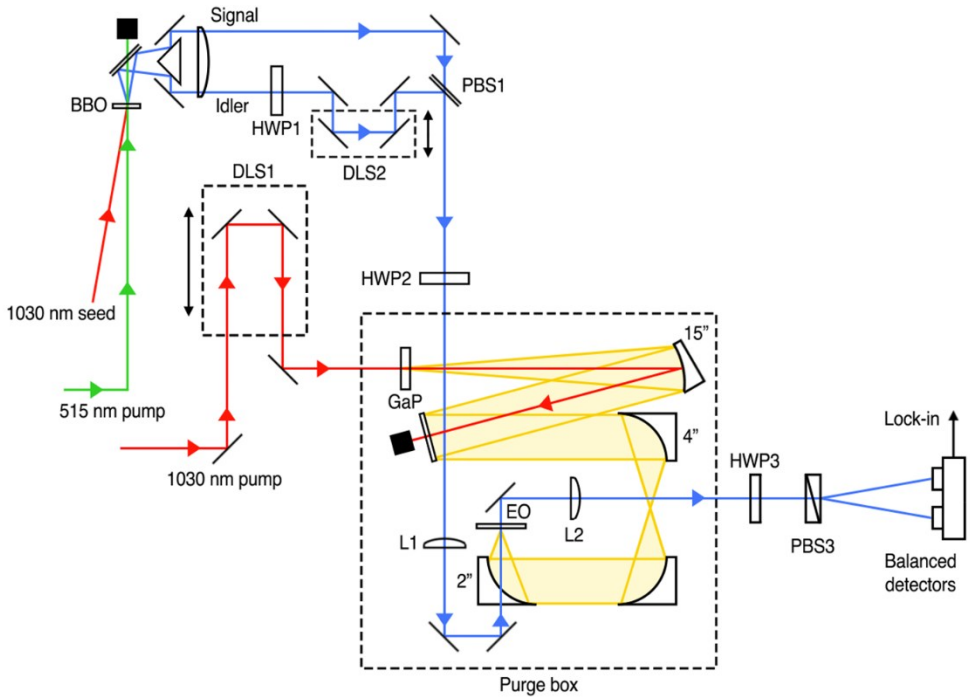

Figure 5.11 - Quantum-enhanced THz-TDS schematic, reconstructed from [94]. TWB: twin-beams | DLS: delay-line stage. The generation of the twin beams is shown in the upper-left section. PBS1 combines the twin beams into a single spatial mode, while DLS1 compensates for the relative path length difference between the signal and idler pulses. DLS2 controls the temporal delay of the THz waveform relative to the probe. HWP1 adjusts the probe polarisation to maximise the THz lock-in signal and HWP2 rotates the signal and idler beams, aligning them with the vertical and horizontal axes of PBS3 (Wollaston prism).

paths, and thus losses, but was temporally delayed via DLS2, so that it purely acted as a reference. The signal polarisation was perpendicular to the generated THz so that the polarisation rotation induced by the THz was maximised.

To ensure phase sensitivity, a small polarisation bias was introduced using HWP3, before the Wollaston prism, on the signal and idler path. This adjustment was required because if the signal polarisation was perfectly aligned with the Wollaston polarisation axis, any THz induced polarisation rotation, either right-handed or left-handed, would result in the same outcome: photons from the signal arm would be redirected to the idler arm. Consequently, the detection system would be insensitive to the sign of the electric field. By ever so slightly rotating the orthogonal signal and idler polarisations the system becomes sensitive to the polarity of the THz field, and thus to its phase, as opposite rotations now produce opposing changes in signal and idler intensities.

An interesting phenomenon was observed when the signal and idler were perfectly overlapped temporally: the differential noise increased significantly, representing interference. This is attributed to the fact that the two fields are cross-polarised and therefore are rotated in opposite directions by the THz-induced birefringence, as described by Planken *et al.* [87]. At the detector, where we are trying to measure the THz-induced imbalance, the opposite rotations are "fighting each other", resulting in partial interference and therefore increase in noise.

To minimise optical losses and preserve the quantum correlations, all surfaces and windows, including those on the purge box which the probe beams are transmitted through, were coated with high quality anti-reflection coatings. Balanced detection was performed using the high quantum efficiency, ultra-low noise transimpedance amplifier developed in Chapter 3. The Zurich MFLI 500MHz lock-in amplifier was used to acquire the THz-TDS traces.

5.5 Quantum-Enhanced THz-TDS Results

In the absence of THz, the differential photocurrent is almost balanced. When the THz interacts with the signal, its polarisation is altered, producing a photocurrent proportional to the THz field amplitude. The pump-beam was modulated at 2.1 kHz and the THz induced differential signal synchronously demodulated. One can either modulate the

probe, the pump or even the THz radiation at the SUT location, however modulating the pump also relaxes heating on the generation crystal as it is subjected to 50% less optical power.

Full waveform scans were acquired with the twin-beams, as described in Figure 5.11. The GaP generation crystal was pumped with pulses of 44.5 μJ energy and 245 fs duration. The laser repetition rate was set to 100 kHz, and total twin-beam power of 0.6 μW.

To make a direct comparison with a classical source, the BBO crystal was removed so that the 1030 nm seed line acted as the coherent probe with p-pol. By inserting a halfwave plate to rotate the polarisation to 45° and subsequently placing a thin-film polariser the twin-beam setup was geometrically simulated using coherent pulses with the same

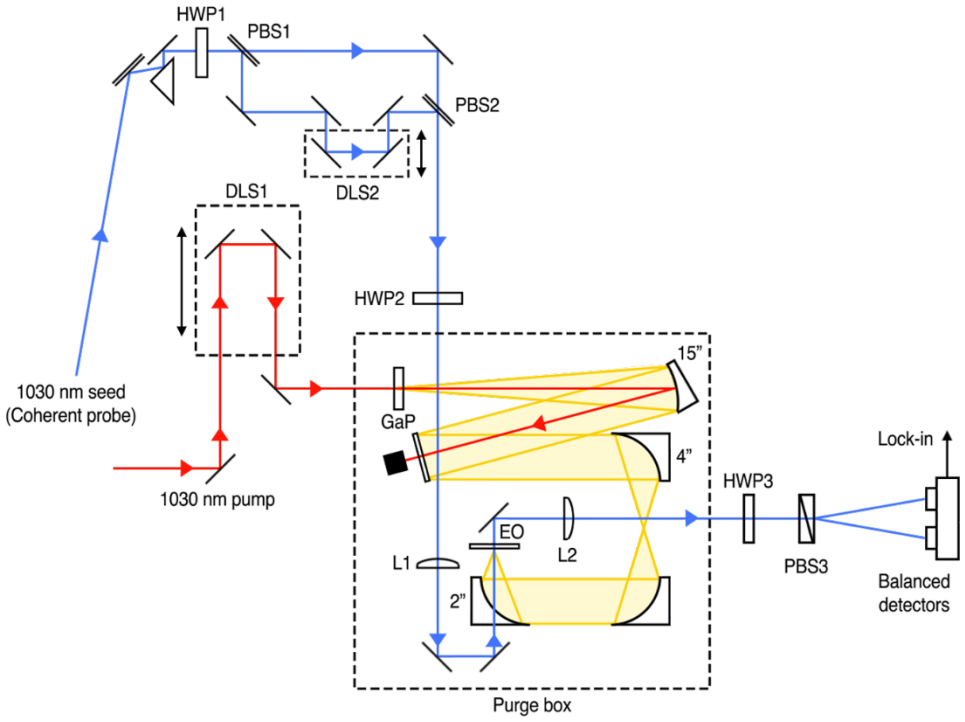

Figure 5.12 - Schematic of the coherent THz-TDS setup used to benchmark the quantum-enhanced configuration. The difference between this setup and that shown in **Figure 5.11** is that the BBO crystal is removed from its holder, the 515nm pump is blocked. The 1030nm seed thereby acts as the coherent probe. HWP1 rotates the linear polarisation to 45° so that p-pol and s-pol have the same optical power as the twin-beams. This coherent configuration, in terms of EOS, is identical to the twin-beam setup minus the quantum correlations and is used as the classical benchmark for evaluating the performance of the quantum-enhanced THz-TDS scheme.

amount of energy. A schematic of the coherent setup used to benchmark the performance of the twin-beam configuration is shown in Figure 5.12.

Here, the probe behaves as a classical coherent field whose sensitivity is limited by the shot-noise limit, as established in Section 4.1. When twin-beams are employed, the signal and idler exhibit strong photon-number correlations, supressing the differential noise below the shot-noise level. Henceforth, the two configurations are identical in every optical aspect (geometry, alignment, energy). This comparison therefore isolates and quantifies the influence of quantum correlations on the performance of the THz-TDS system.

The corresponding THz-TDS traces are shown in Figure 5.13A where the THz waveform acquired employing the twin-beams exhibits visibly lower noise. The orange waveform can be seen to be slightly temporally compressed. This is a consequence of the shorter ($\simeq$ 171fs) duration of the squeezed pulses compared to the coherent probe ($\simeq$ 245 fs). This arises from the temporal compression occurring in the SHG process that generates the 515 nm field employed as the pump in the twin-beam generation process.

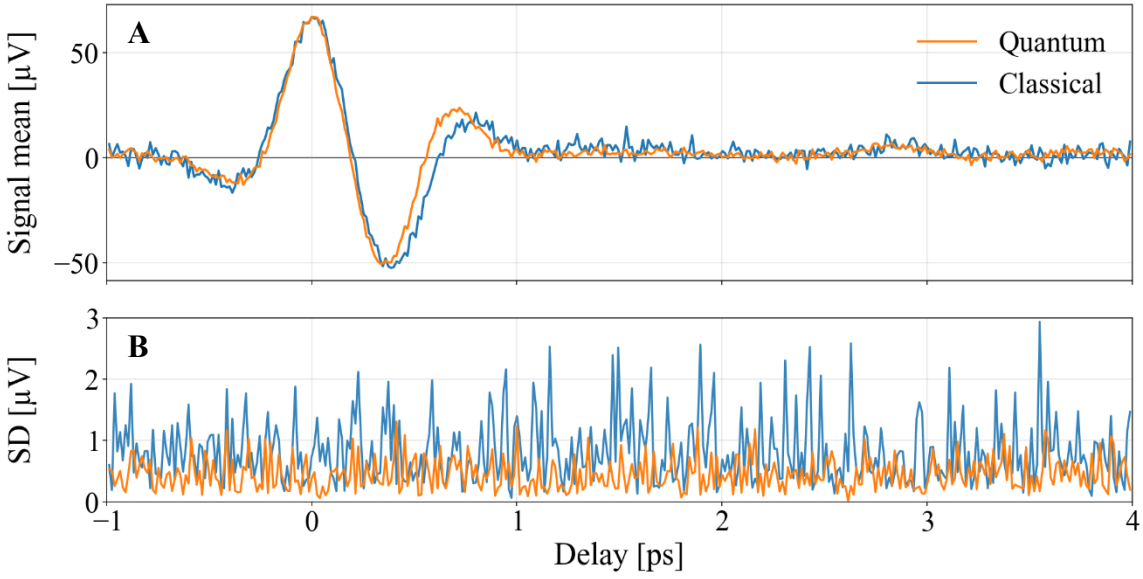

Figure 5.13 - Comparison of THz-TDS traces recorded with twin-beam (orange) and coherent (blue) probes. The top panel (**A**) shows the full THz waveform, where the mean signal amplitude has been plotted against temporal delay. Panel **B** presents the corresponding standard deviation of the measured data versus temporal delay, highlighting the independence of the standard deviation to delay position.

A statistical ensemble of measurements was acquired at each delay-line point to determine the standard deviation of the signal across the 5ps window.

The results, presented in Figure 5.13B confirm that the standard deviation remains uniform and independent of the temporal delay. This indicates with confidence that the probe is the dominant source of noise in these measurements. The standard deviation, averaged over the entire trace was $\bar{\sigma}_c = 0.82$ μV for the classical case and $\bar{\sigma}_q = 0.43$μV for the twin-beam case, indicating a two-fold reduction in noise. This is consistent with the measured NRF of the twin-beam source, as reported in Section 4.3.

To accurately assess the SNR of the detection, the THz peak data (at t = 0s on Figure 5.13A) were sampled for 60 s and the standard deviation was computed, where the peak signal was normalised for both probe configurations. The results, shown in Figure 5.14 indicate that the average normalised SD for the classical and the quantum case are $\bar{\sigma}_{r,c} \simeq 0.050$ and $\bar{\sigma}_{r,q} \simeq 0.025$ respectively. This demonstrates that two-mode squeezing improves the SNR of the time-resolved electric field by a factor of two, compared to what is possible with classical probes. In THz-TDS, SNR is defined as the ratio between the average value of the signal at the THz peak and its associated standard deviation [89].

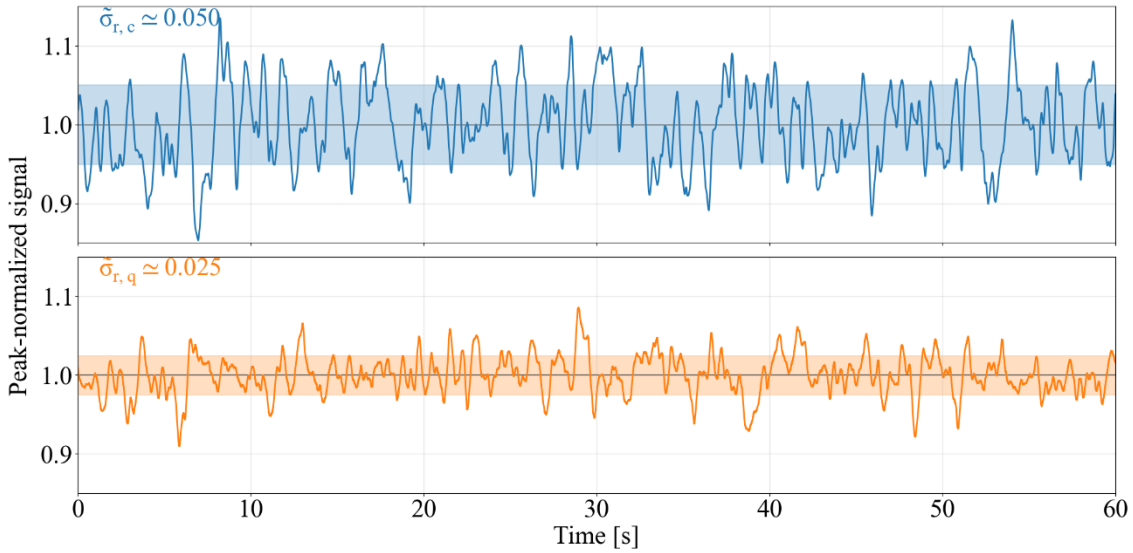

Figure 5.14 - Normalized electric field value acquired over 60 s for the classical (blue) and quantum (orange) measurements. Values within 1 SD are shown in both cases with a shaded area.

From the recorded THz traces, which contain the mean and standard deviation of the field at different probe delays, the expected noise reduction in the THz field spectral properties (amplitude and phase) can be inferred. To this end, a series of $\mathrm{N} = 1000$ temporal traces were generated numerically (for both quantum and classical configurations) with each temporal trace being assigned amplitude values at all delay points. For each delay point, the amplitude value assigned is randomly sampled from a normal distribution with a mean and standard deviation corresponding to average THz signal and the average measured standard deviation, respectively.

A Fourier-transform was then performed on each temporal trace so that the complex spectral field was obtained

$$\widetilde{\boldsymbol{E}}(\Omega) = \boldsymbol{F}_{\mathbf{t}}\{\boldsymbol{E}(\boldsymbol{t})\}. \qquad \textbf{5.31}$$

Subsequently, the average and the standard deviation at each frequency point of the $\tilde{E}(\Omega)$ trace ensemble was computed. The resultant average power spectral densities (PSD) $S(\Omega) = |\tilde{E}(\Omega)|^2$ are shown in Figure 5.15 as shaded regions for both the quantum (orange) and classical (blue) configurations. The slight discrepancy between the power spectra comes from the differing pulse durations of the probe pulses used to sample the THz fields. The error bars correspond to the uncertainty of the power spectra.

To establish and quantify the quantum enhancement in the spectral domain, a ratio between the relative errors of the classical and quantum measurement was computed at each frequency point.

$$\eta_{\mathrm{S}}(\Omega) = \frac{\sigma_{\mathrm{S},c}(\Omega)/\bar{S}_{\mathrm{c}}(\Omega)}{\sigma_{\mathrm{S},q}(\Omega)/\bar{S}_{\mathrm{q}}(\Omega)}. \qquad \textbf{5.32}$$

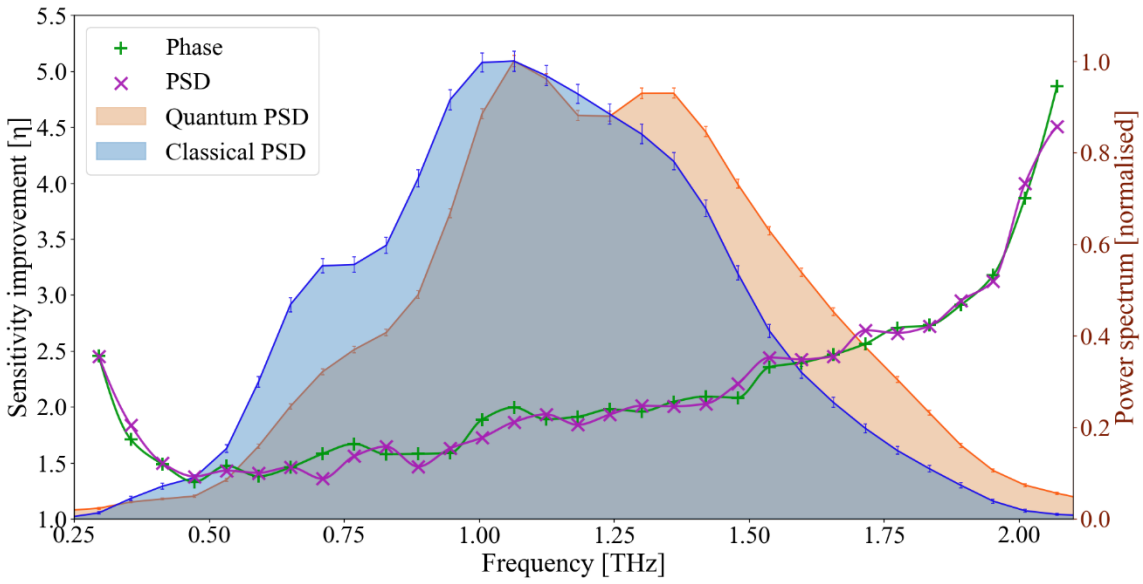

Figure 5.15 - Spectral Analysis. Normalised power spectral density (PSD, solid colours, right axis) for the classical (blue) and quantum (orange) measurements, computed as explained in the text. The green and purple crosses show the values of the sensitivity improvement in the estimation of the spectral phase and power spectral density, respectively (left axis, see the main text for details).

Where $\sigma_{S,c}$ and $\sigma_{S,q}$ denote the standard deviations of the power spectral data at frequency Ω for the classical and quantum measurement, respectively, and $\bar{S}_{\mathrm{c}}$ and $\bar{S}_{\mathrm{q}}$ represent the corresponding mean PSD values at the same frequency. This metric, illustrated by the purple crosses (values on the left-hand axis) in Figure 5.15, quantifies the relative enhancement in sensitivity of power spectral measurements. A value of $\eta_{\mathrm{S}} > 1$ is observed, spanning across the entire spectrum, indicating an improvement in sensitivity of the THz-TDS system when twin-beams are employed as a probe. Notably, $\eta_{\mathrm{S}} > 2$ for a substantial portion of the spectrum indicating a substantial noise reduction.

A similar metric was defined for the spectral phase $\Phi(\Omega) = \mathrm{Arg}[\tilde{E}(\Omega)]$, as

$$\boldsymbol{\eta_{\Phi}(\Omega) = \frac{\sigma_{\Phi,\mathrm{c}}(\Omega)/\bar{\Phi}_{\mathrm{c}}(\Omega)}{\sigma_{\Phi,\mathrm{q}}(\Omega)/\bar{\Phi}_{\mathrm{q}}(\Omega)}.} \qquad \textbf{5.33}$$

The same definitions used for Eq. 5.32 apply here, with $\sigma_{\Phi,c}$ and $\sigma_{\Phi,q}$ representing the standard deviations of the spectral phase at Ω for the classical and quantum probe measurements. Additionally, $\bar{\Phi}_c$ and $\bar{\Phi}_q$ correspond to the mean values of the same dataset at the same frequency. The values of η_Φ reflect the improvement in phase-retrieval precision leveraged when employing two-mode squeezed light.

The results presented in this Section have been published in *Science Advances [90]*

6 Conclusion and Outlook

In this work, the development of ultrafast quantum optical technologies has been presented, aimed at improving the sensitivity of terahertz time-domain spectroscopy. Multiple technologies have been bridged, spanning from low-noise optoelectronics to nonlinear and quantum optics, culminating in the realisation of the first THz-TDS system operating beyond the classical limit.

Based on the theoretical and experimental framework established for the generation and detection of quantum-correlated light, a custom balanced detector was designed and constructed optimised for electronic low-noise (< 7 fA$\sqrt{\text{Hz}}$) and high quantum efficiency (95%). Assessment of its common-mode rejection ratio, bandwidth, and stability validated its suitability for sub shot-noise measurements.

Building on this foundation, shot-noise limited performance was demonstrated using balanced-detection. Subsequently, a twin-beam source was realised through spontaneous parametric down-conversion in a barium-borate crystal, where the noise statistics of the twin-beams was compared to the shot-noise limit at the corresponding optical power level. The noise reduction factor for the spontaneous case was evaluated using crystals of 1 mm and 2 mm length, but it was found that for increasing down-converted photons per pulse the noise reduction degraded, limiting the PDC output power in the nanowatt range.

A key objective of this work is to enhance the sensitivity of THz-TDS using quantum probes of optical power levels to standard approaches. The SPDC twin-beam source was found to be too fragile for this purpose. Therefore, an alternative configuration was investigated and subsequently realised. By coherently seeding the parametric down-conversion process, a NRF exceeding 6 dB was achieved at optical powers close to 1 μW, marking an important step toward quantum-enhanced ultrafast time-domain measurements.

Finally, a complete THz-TDS platform was developed, operating at 100 kHz with 245 fs pulse duration. Terahertz pulses were generated and detected via optical-rectification and electro-optic sampling, respectively, using GaP crystals. The twin-beams were integrated into the system, and the noise performance was compared to that employing a classical probe, under identical conditions. Analysis of the results in both time and frequency domain concludes that the twin-beam THz-TDS system, showed enhanced sensitivity compared to when the classical probe was used.

This work represents the first demonstration of employing quantum probes to enhance the sensitivity of THz-TDS measurements, with the caveat that it does not represent a standard THz-TDS implementation. Due to the nature of the source, the THz-TDS system had to be slightly modified, effectively transforming the standard polarimetric measurement to a differential transient absorption measurement. As a result, the modified configuration inherently yields lower SNR than what is achievable with conventional polarimetric techniques.

The sensitivity improvements demonstrated here open pathways to measurements that remain inaccessible to classical THz-TDS systems. A particularly promising direction is the integration of phase-squeezed states within SU (1,1) nonlinear interferometers [91]. In such a configuration, the first OPA generates quantum-correlated signal and idler beams, which subsequently serve as the probe in electro-optic sampling. The THz-induced phase modulation is then coherently amplified by the second OPA prior to detection. This architecture would yield sub-shot-noise phase sensitivity within a standard polarimetric geometry. It would potentially enable a more direct integration of quantum probes into conventional THz-TDS systems, addressing the key limitation of the modified differential absorption configuration employed in this work.

Another potential avenue is to experimentally build the scheme proposed by Virally *et al.* [92], where one beam of a PDC twin-beam pair is used to condition the statistics of the other, producing a nonclassical probe state tailored for electro-optic sampling. Unlike a classical coherent probe, this conditioned state remains sensitive to higher-order statistical moments of the THz field, resulting in a predicted sixfold improvement in signal-to-noise ratio.

Moreover, alternative sensing modalities such as phase interferometry [93] are under investigation for THz applications and represent a natural candidate for integration with phase-squeezed states, potentially extending quantum-enhanced sensitivity beyond the intensity-correlation regime explored here.

Overall, the results achieved in this thesis outline the progress made from developing optoelectronic hardware enabling quantum-noise reduction measurements to harnessing the quantum advantage within a THz-TDS system. We have experimentally demonstrated a quantum advantage, using quantum sources at probe power levels comparable to those routinely used in field-resolved spectroscopy, thereby paving the way for further developments toward quantum-enhanced field-resolved spectroscopy. The sensitivity improvements demonstrated here open pathways toward measurements that remain inaccessible to classical THz-TDS systems, with potential applications spanning condensed matter physics, materials characterisation, and chemical sensing. A particularly compelling frontier is the field spectroscopy of biological samples, where THz radiation is uniquely sensitive to low-frequency collective vibrational modes, intermolecular hydrogen-bond dynamics, and hydration-layer structure, all of which are intimately linked to protein conformation and function. Early-stage disease processes, including misfolding, aggregation, and changes in cellular hydration, produce subtle spectroscopic signatures in the THz band that are obscured by noise in conventional systems. The quantum-enhanced sensitivity demonstrated in this work, at probe powers compatible with fragile biological specimens, represents a step toward resolving such signatures.

Bibliography

[1] J. Haas and B. Mizaikoff, “Advances in Mid-Infrared Spectroscopy for Chemical Analysis,” Jun. 12, 2016, *Annual Reviews Inc.* doi: 10.1146/annurev-anchem-071015-041507.

[2] C. Funk *et al.*, “The climate hazards infrared precipitation with stations—a new environmental record for monitoring extremes,” *Sci. Data*, vol. 2, no. 1, p. 150066, 2015, doi: 10.1038/sdata.2015.66.

[3] J.-X. Cheng and X. S. Xie, “Vibrational spectroscopic imaging of living systems: An emerging platform for biology and medicine,” *Science (1979).*, vol. 350, no. 6264, p. aaa8870, 2015.

[4] I. Newton, “A letter of Mr. Isaac Newton, Professor of the Mathematicks in the University of Cambridge; containing his new theory about light and colors: sent by the author to the publisher from Cambridge, Febr. 6. 1671/72; in order to be communicated to the R. Society,” *Philos. Trans. R. Soc. Lond.*, vol. 6, no. 80, pp. 3075–3087, Jan. 1997, doi: 10.1098/rstl.1671.0072.

[5] W. H. Wollaston, “XII. A method of examining refractive and dispersive powers, by prismatic reflection,” *Philos. Trans. R. Soc. Lond.*, no. 92, pp. 365–380, 1802.

[6] I. Howard-Duff, “Joseph Fraunhofer (1787-1826),” *Journal of the British Astronomical Association, vol. 97, no. 6, p. 339-347*, vol. 97, pp. 339–347, 1987.

[7] W. D. W. Abney and L. Festing, “XX, On the influence of the atomic grouping in the molecules of organic bodies on their absorption in the infra-red region of the spectrum,” *Philos. Trans. R. Soc. Lond.*, no. 172, pp. 887–918, 1881.

[8] D. T. Emerson, “The work of Jagadis Chandra Bose: 100 years of millimeter-wave research,” *IEEE Trans. Microw. Theory Tech.*, vol. 45, no. 12, pp. 2267–2273, 1997, doi: 10.1109/22.643830.

[9] J. M. Chamberlain, “Where optics meets electronics: recent progress in decreasing the terahertz gap,” *Philosophical Transactions of the Royal Society of London. Series A: Mathematical, Physical and Engineering Sciences*, vol. 362, no. 1815, pp. 199–213, 2004.

[10] A. G. Davies, A. D. Burnett, W. Fan, E. H. Linfield, and J. E. Cunningham, "Terahertz spectroscopy of explosives and drugs," *Materials today*, vol. 11, no. 3, pp. 18–26, 2008.

[11] H.-B. Liu, Y. Chen, G. J. Bastiaans, and X.-C. Zhang, "Detection and identification of explosive RDX by THz diffuse reflection spectroscopy," *Opt. Express*, vol. 14, no. 1, pp. 415–423, 2006.

[12] J. Ma, N. J. Karl, S. Bretin, G. Ducournau, and D. M. Mittleman, "Frequency-division multiplexer and demultiplexer for terahertz wireless links," *Nat. Commun.*, vol. 8, no. 1, p. 729, 2017.

[13] H. J. Joyce, J. L. Boland, C. L. Davies, S. A. Baig, and M. B. Johnston, "A review of the electrical properties of semiconductor nanowires: insights gained from terahertz conductivity spectroscopy," *Semicond. Sci. Technol.*, vol. 31, no. 10, p. 103003, 2016.

[14] H. Rubens, *Gittermessungen im langwelligen Spektrum*. 1921.

[15] P. R. Smith, D. H. Auston, and M. C. Nuss, "Subpicosecond photoconducting dipole antennas," *IEEE J. Quantum Electron.*, vol. 24, no. 2, pp. 255–260, 1988.

[16] D. Grischkowsky, S. Keiding, M. Van Exter, and C. Fattinger, "Far-infrared time-domain spectroscopy with terahertz beams of dielectrics and semiconductors," *Journal of the Optical Society of America B*, vol. 7, no. 10, pp. 2006–2015, 1990.

[17] M. Huber *et al.*, "Standardized electric-field-resolved molecular fingerprinting," *Anal. Chem.*, vol. 96, no. 32, pp. 13110–13119, 2024.

[18] I. Pupeza *et al.*, "Field-resolved infrared spectroscopy of biological systems," *Nature*, vol. 577, no. 7788, pp. 52–59, 2020.

[19] F. Krausz, "Nobel Lecture: Sub-atomic motions," *Rev. Mod. Phys.*, vol. 96, no. 3, p. 30502, Aug. 2024, doi: 10.1103/RevModPhys.96.030502.

[20] C. Hofer *et al.*, "Linear field-resolved spectroscopy approaching ultimate detection sensitivity," *Opt. Express*, vol. 33, no. 1, pp. 1–17, 2025, doi: 10.1364/OE.536543.

[21] C. Kübler, R. Huber, S. Tübel, and A. Leitenstorfer, "Ultrabroadband detection of multi-terahertz field transients with GaSe electro-optic sensors: Approaching the near infrared," *Appl. Phys. Lett.*, vol. 85, pp. 3360–3362, 2004, [Online]. Available: https://api.semanticscholar.org/CorpusID:122040833

[22] T. L. M. Guedes, I. Vakulchyk, D. V. Seletskiy, A. Leitenstorfer, A. S. Moskalenko, and G. Burkard, “Back action in quantum electro-optic sampling of electromagnetic vacuum fluctuations,” vol. 3, 2022.

[23] S. Virally, P. Cusson, and D. V. Seletskiy, “Enhanced Electro-optic Sampling with Quantum Probes,” *Phys. Rev. Lett.*, vol. 127, no. 27, pp. 1–6, 2021, doi: 10.1103/PhysRevLett.127.270504.

[24] B. E. A. Saleh and M. C. Teich, *Fundamentals of photonics*, vol. 332. Wiley New York, 2008.

[25] T. H. Maiman, “Stimulated optical radiation in ruby,” *Nature*, vol. 187, no. 4736, pp. 493–494, 1960.

[26] eg P. A. Franken, A. E. Hill, C. W. Peters, and G. Weinreich, “Generation of optical harmonics,” *Phys. Rev. Lett.*, vol. 7, no. 4, p. 118, 1961.

[27] M. Bass, P. A. Franken, A. E. Hill, C. W. Peters, and G. Weinreich, “Optical mixing,” *Phys. Rev. Lett.*, vol. 8, no. 1, p. 18, 1962.

[28] M. Bass, P. A. Franken, J. F. Ward, and G. Weinreich, “Optical rectification,” *Phys. Rev. Lett.*, vol. 9, no. 11, p. 446, 1962.

[29] J. A. Giordmaine, “Mixing of light beams in crystals,” *Phys. Rev. Lett.*, vol. 8, no. 1, p. 19, 1962.

[30] J. A. Giordmaine and R. C. Miller, “Tunable coherent parametric oscillation in LiNb O 3 at optical frequencies,” *Phys. Rev. Lett.*, vol. 14, no. 24, p. 973, 1965.

[31] R. Y. Chiao, C. H. Townes, and B. P. Stoicheff, “Stimulated Brillouin scattering and coherent generation of intense hypersonic waves,” *Phys. Rev. Lett.*, vol. 12, no. 21, p. 592, 1964.

[32] R. W. Terhune, P. D. Maker, and C. M. Savage, “Optical harmonic generation in calcite,” *Phys. Rev. Lett.*, vol. 8, no. 10, p. 404, 1962.

[33] R. Y. Chiao, E. Garmire, and C. H. Townes, “Self-trapping of optical beams,” *Phys. Rev. Lett.*, vol. 13, no. 15, p. 479, 1964.

[34] J. A. Armstrong, N. Bloembergen, J. Ducuing, and P. S. Pershan, “Interactions between Light Waves in a Nonlinear Dielectric,” *Physical Review*, vol. 127, no. 6, pp. 1918–1939, Sep. 1962, doi: 10.1103/PhysRev.127.1918.

[35] S. M. A. Mirzaee and J.-M. Nunzi, “Searching for evidence of optical rectification: optically induced nonlinear photovoltage in a capacitor configuration,” *Journal of the Optical Society of America B*, vol. 36, no. 1, pp. 53–60, 2018.

[36] R. W. Boyd, *Nonlinear Optics*, 4th ed. Academic Press (Elsevier), 2020.

[37] R. Luo, Y. He, H. Liang, M. Li, and Q. Lin, "Highly tunable efficient second-harmonic generation in a lithium niobate nanophotonic waveguide," *Optica*, vol. 5, no. 8, pp. 1006–1011, 2018.

[38] M. M. Fejer, G. A. Magel, D. H. Jundt, and R. L. Byer, "Quasi-phase-matched second harmonic generation: tuning and tolerances," *IEEE J. Quantum Electron.*, vol. 28, no. 11, pp. 2631–2654, 2002.

[39] C. Couteau, "Spontaneous parametric down-conversion," *Contemp. Phys.*, vol. 59, no. 3, pp. 291–304, 2018.

[40] G. Kulkarni, J. Rioux, B. Braverman, M. V Chekhova, and R. W. Boyd, "Classical model of spontaneous parametric down-conversion," *Phys. Rev. Res.*, vol. 4, no. 3, p. 33098, Aug. 2022, doi: 10.1103/PhysRevResearch.4.033098.

[41] D. F. Walls, "Squeezed states of light," *Nature*, vol. 306, no. 5939, pp. 141–146, 1983, doi: 10.1038/306141a0.

[42] R. Schnabel, "Squeezed states of light and their applications in laser interferometers," *Phys. Rep.*, vol. 684, pp. 1–51, 2017.

[43] E. S. Polzik, J. Carri, and H. J. Kimble, "Spectroscopy with squeezed light," *Phys. Rev. Lett.*, vol. 68, no. 20, pp. 3020–3023, May 1992, doi: 10.1103/PhysRevLett.68.3020.

[44] M. A. Taylor *et al.*, "Biological measurement beyond the quantum limit," *Nat. Photonics*, vol. 7, no. 3, pp. 229–233, 2013, doi: 10.1038/nphoton.2012.346.

[45] T. Gehring *et al.*, "Implementation of continuous-variable quantum key distribution with composable and one-sided-device-independent security against coherent attacks," *Nat. Commun.*, vol. 6, no. 1, p. 8795, 2015, doi: 10.1038/ncomms9795.

[46] C. M. Caves, "Quantum-mechanical noise in an interferometer," *Physical Review D*, vol. 23, no. 8, pp. 1693–1708, Apr. 1981, doi: 10.1103/PhysRevD.23.1693.

[47] J. Abadie *et al.*, "A gravitational wave observatory operating beyond the quantum shot-noise limit," *Nat. Phys.*, vol. 7, no. 12, pp. 962–965, 2011, doi: 10.1038/nphys2083.

[48] J. Aasi *et al.*, "Enhanced sensitivity of the LIGO gravitational wave detector by using squeezed states of light," *Nat. Photonics*, vol. 7, no. 8, pp. 613–619, 2013, doi: 10.1038/nphoton.2013.177.

[49] A. I. Lvovsky, “Squeezed light,” *Photonics: Scientific Foundations, Technology and Applications*, vol. 1, pp. 121–163, 2015.

[50] C. Zhang, Y. Huang, B. Liu, C. Li, and G. Guo, “Spontaneous parametric down-conversion sources for multiphoton experiments,” *Adv. Quantum Technol.*, vol. 4, no. 5, p. 2000132, 2021.

[51] T. Shields *et al.*, “Electro-Optical Sampling of Single-Cycle THz Fields with Single-Photon Detectors,” *Sensors*, vol. 22, no. 23, 2022, doi: 10.3390/s22239432.

[52] S. Hong *et al.*, “Quantum enhanced multiple-phase estimation with multi-mode N 00 N states,” *Nat. Commun.*, vol. 12, no. 1, p. 5211, 2021.

[53] T. Shields *et al.*, “Electro-optical sampling of single-cycle THz fields with single-photon detectors,” *Sensors*, vol. 22, no. 23, p. 9432, 2022.

[54] L.-A. Wu, H. J. Kimble, J. L. Hall, and H. Wu, “Generation of squeezed states by parametric down conversion,” *Phys. Rev. Lett.*, vol. 57, no. 20, p. 2520, 1986.

[55] R. E. Slusher, L. W. Hollberg, B. Yurke, J. C. Mertz, and J. F. Valley, “Observation of Squeezed States Generated by Four-Wave Mixing in an Optical Cavity,” *Phys. Rev. Lett.*, vol. 55, no. 22, pp. 2409–2412, Nov. 1985, doi: 10.1103/PhysRevLett.55.2409.

[56] H. Vahlbruch, M. Mehmet, K. Danzmann, and R. Schnabel, “Detection of 15 dB Squeezed States of Light and their Application for the Absolute Calibration of Photoelectric Quantum Efficiency,” *Phys. Rev. Lett.*, vol. 117, no. 11, p. 110801, Sep. 2016, doi: 10.1103/PhysRevLett.117.110801.

[57] T. Eberle *et al.*, “Quantum Enhancement of the Zero-Area Sagnac Interferometer Topology for Gravitational Wave Detection,” *Phys. Rev. Lett.*, vol. 104, no. 25, p. 251102, Jun. 2010, doi: 10.1103/PhysRevLett.104.251102.

[58] R. E. Slusher, P. Grangier, A. Laporta, B. Yurke, and M. J. Potasek, “Pulsed squeezed light,” *Phys. Rev. Lett.*, vol. 59, no. 22, pp. 2566–2569, 1987, doi: 10.1103/PhysRevLett.59.2566.

[59] J. Wenger, R. Tualle-Brouri, and P. Grangier, “Pulsed homodyne measurements of femtosecond squeezed pulses generated by single-pass parametric deamplification,” *Opt. Lett.*, vol. 29, no. 11, pp. 1267–1269, 2004.

[60] C. Kim and P. Kumar, “Quadrature-Squeezed Light Detection Using a Self-Generated Matched Local Oscillator,” *Phys. Rev. Lett.*, vol. 73, no. 12, pp. 1605–1608, Sep. 1994, doi: 10.1103/PhysRevLett.73.1605.

[61] J. Amari, J. Takai, and T. Hirano, “Highly efficient measurement of optical quadrature squeezing using a spatial light modulator controlled by machine learning,” *Optics Continuum*, vol. 2, no. 4, pp. 933–941, 2023.

[62] O. Aytür and P. Kumar, “Pulsed twin beams of light,” *Phys. Rev. Lett.*, vol. 65, no. 13, pp. 1551–1554, Sep. 1990, doi: 10.1103/PhysRevLett.65.1551.

[63] A. Pozzoli, M. Lamperti, M. Clerici, M. Bondani, and A. Allevi, “Optimal generation of mesoscopic twin-beam states by means of a natively femtosecond laser system,” *APL Photonics*, vol. 10, no. 3, 2025.

[64] M. A. Finger, T. S. Iskhakov, N. Y. Joly, M. V Chekhova, and P. S. J. Russell, “Raman-free, noble-gas-filled photonic-crystal fiber source for ultrafast, very bright twin-beam squeezed vacuum,” *Phys. Rev. Lett.*, vol. 115, no. 14, p. 143602, 2015.

[65] A. Allevi, S. Olivares, and M. Bondani, “Measuring high-order photon-number correlations in experiments with multimode pulsed quantum states,” *Phys. Rev. A*, vol. 85, no. 6, pp. 1–5, 2012, doi: 10.1103/PhysRevA.85.063835.

[66] P. Horowitz, W. Hill, and I. Robinson, *The art of electronics*, vol. 2. Cambridge university press Cambridge, 1989.

[67] K. K. Ng and S. M. Sze, *Physics of semiconductor devices*. Wiley-Interscience Hoboken, NJ, 2007.

[68] X. Ramus, “Transimpedance considerations for high-speed amplifiers,” *Application Report SBOA122. Texas Instruments*, p. 97, 2009.

[69] S. Franco and F. Sergio, *Design with operational amplifiers and analog integrated circuits*, vol. 1988. McGraw-Hill New York, 2002.

[70] D. N. Nikogosyan, *Nonlinear optical crystals: a complete survey*. Springer, 2005.

[71] A. Allevi and M. Bondani, “Multi-mode twin-beam states in the mesoscopic intensity domain,” *Physics Letters, Section A: General, Atomic and Solid State Physics*, vol. 423, p. 127828, 2022, doi: 10.1016/j.physleta.2021.127828.

[72] A. V Smith, *Crystal nonlinear optics: with SNLO examples*. AS-Photonics Albuquerque, NM, USA, 2018.

[73] E. Brambilla, A. Gatti, M. Bache, and L. A. Lugiato, “Simultaneous near-field and far-field spatial quantum correlations in the high-gain regime of parametric down-conversion,” *Phys. Rev. A*, vol. 69, no. 2, p. 19, 2004, doi: 10.1103/PhysRevA.69.023802.

[74] A. Gatti, M. Clerici, and L. Caspani, “Enhancing upconversion with space–time entanglement: from twin photons to twin-beams,” *Optica Quantum*, vol. 3, no. 3, pp. 269–279, 2025.

[75] a Heidmann, R. Horowicz, S. Reynaud, E. Giacobino, C. Fabre, and G. Camy, “Observation of quantum noise reduction on twin laser beams.,” *Phys. Rev. Lett.*, vol. 59, no. 22, pp. 2555–2557, Nov. 1987, [Online]. Available: http://www.ncbi.nlm.nih.gov/pubmed/10035582

[76] I. N. Agafonov, M. V Chekhova, and G. Leuchs, “Two-color bright squeezed vacuum,” *Phys. Rev. A (Coll. Park).*, vol. 82, no. 1, p. 11801, Jul. 2010, doi: 10.1103/PhysRevA.82.011801.

[77] T. Dickinson *et al.*, “Quantum-enhanced second harmonic generation beyond the photon pairs regime,” *Sci. Adv.*, vol. 11, no. 27, p. eadw4820, 2025.

[78] J. Mooney and P. Kambhampati, “Get the basics right: Jacobian conversion of wavelength and energy scales for quantitative analysis of emission spectra,” 2013, *ACS Publications*.

[79] D. F. Walls and G. J. Milburn, “Input–output formulation of optical cavities,” in *Quantum optics*, Springer, 2008, pp. 127–141.

[80] D. T. Smithey, M. Beck, M. Belsley, and M. G. Raymer, “Sub-shot-noise correlation of total photon number using macroscopic twin pulses of light,” *Phys. Rev. Lett.*, vol. 69, no. 18, p. 2650, 1992.

[81] X.-C. Zhang and J. Xu, *Introduction to THz wave photonics*, vol. 29. Springer, 2010.

[82] J.-P. Negel, R. Hegenbarth, A. Steinmann, B. Metzger, F. Hoos, and H. Giessen, “Compact and cost-effective scheme for THz generation via optical rectification in GaP and GaAs using novel fs laser oscillators,” *Applied Physics B*, vol. 103, no. 1, pp. 45–50, 2011.

[83] J. Huang *et al.*, “High efficient terahertz generation from cryogenic gallium phosphide based on collinear difference frequency,” in *Fifth International Symposium on Laser Interaction with Matter*, SPIE, 2019, pp. 726–732.

[84] D. J. Wilson *et al.*, “Integrated gallium phosphide nonlinear photonics,” *Nat. Photonics*, vol. 14, no. 1, pp. 57–62, 2020.

[85] Q. Chen, M. Tani, Z. Jiang, and X.-C. Zhang, “Electro-optic transceivers for terahertz-wave applications,” *Journal of the Optical Society of America B*, vol. 18, no. 6, pp. 823–831, 2001.

[86] M. Yang *et al.*, “Second harmonic generation in monolithic gallium phosphide metasurfaces,” *Nanophotonics*, vol. 13, no. 18, pp. 3311–3319, 2024.

[87] P. C. M. Planken, H.-K. Nienhuys, H. J. Bakker, and T. Wenckebach, “Measurement and calculation of the orientation dependence of terahertz pulse detection in ZnTe,” *Journal of the Optical Society of America B*, vol. 18, no. 3, pp. 313–317, 2001.

[88] L. Hirsch, D. Adamou, D. Faccio, M. Peccianti, and M. Clerici, “Design of an optimized terahertz time-domain spectroscopy system pumped by a 30 W Yb: KGW source at a 100 kHz repetition rate with 245 fs pulse duration,” *Applied Sciences*, vol. 14, no. 15, p. 6688, 2024.

[89] M. Naftaly and R. Dudley, “Methodologies for determining the dynamic ranges and signal-to-noise ratios of terahertz time-domain spectrometers,” *Opt. Lett.*, vol. 34, no. 8, pp. 1213–1215, 2009.

[90] D. Adamou *et al.*, “Quantum-enhanced time-domain spectroscopy,” *Sci. Adv.*, vol. 11, no. 4, p. eadt2187, 2025.

[91] Z. Y. Ou, “Enhancement of the phase-measurement sensitivity beyond the standard quantum limit by a nonlinear interferometer,” *Physical Review A—Atomic, Molecular, and Optical Physics*, vol. 85, no. 2, p. 023815, 2012.

[92] S. Virally, P. Cusson, and D. V Seletskiy, “Enhanced electro-optic sampling with quantum probes,” *Phys. Rev. Lett.*, vol. 127, no. 27, p. 270504, 2021.

[93] A. Velten, A. Schmitt-Sody, and J.-C. Diels, “Precise intracavity phase interferometry in an optical parametric oscillator with two pulses per cavity round trip,” *Opt. Lett.*, vol. 35, no. 8, pp. 1181–1183, 2010.

[94] Lenny Hirsch, “Design of a THz-TDS system optimised for high signal-to-noise ratio,” University of Glasgow, Glasgow, 2025. Accessed: Oct. 23, 2025. [Online]. Available: https://theses.gla.ac.uk/85214/